

MASTER THESIS

Structural Optimization of Uniform Strength Noise Barrier

C. Chen



 **TU**Delft


SUMMUM

Structural Optimization of Uniform Strength Noise Barrier

by

Chiayu Chen

to obtain the degree of Master of Science in Civil Engineering
at the Delft University of Technology,
to be defended publicly on August 23, 2023

Student number: 5486300

Project duration: January 01, 2023 - August 23, 2023

Thesis supervisor: Dr.ir. Diederik Veenendaal

Summum Engineering

Thesis committee: Prof. dr. ir. Max Hendriks

Delft University of Technology, Chair

Dr. ir. Pierre Hoogenboom

Delft University of Technology

Ir. Hoessein Alkisaie

Delft University of Technology



Preface

The culmination of my Master's degree at Delft University of Technology is represented by the Master's thesis presented here. This work serves as the final step of my Master's journey in Civil Engineering and Geosciences, conducted in collaboration with both Summum Engineering and Delft University of Technology.

I extend my appreciation to Diederik Veenendaal for not only introducing me to this captivating subject but also guiding me with his extensive expertise in computational modeling. My gratitude also goes to Jelle Feringa, whose technological contributions have translated the project into reality. Witnessing my theoretical input materialize into an actual structural piece on the ground has been a truly exceptional experience. Working alongside the entire team at the office has also been inspiring and motivating.

Furthermore, I am thankful to my thesis committee members, namely Max Hendriks, Pierre Hoogenboom, and Hoessein Alkisaie, for their invaluable feedback and guidance throughout my progress. The cooperative and positive atmosphere during our meetings spurred me on and provided a sense of motivation. Special thanks are owed to Max Hendriks for his role as committee chairman, providing practical advice on research methodologies, as well as enhancing the effectiveness of my thesis presentation. I am also immensely grateful to Pierre Hoogenboom for his guidance in resolving mathematical challenges and posing thought-provoking questions that encouraged a deeper exploration of my research.

Lastly, I wish to acknowledge the support of my friends and family, who have stood by me throughout my academic journey. I reserve special gratitude for my parents, whose unwavering beliefs have been a cornerstone of my success.

Thank you for taking the time to read and engage with my thesis.

*Chiayu Chen,
Delft, August 2023*

Contents

Preface	i
Summary	ix
1 Introduction	1
1.1 Problem statement and research objectives	2
1.2 Thesis structure and research methodology	3
2 Literature review	5
2.1 Analytical form finding	5
2.1.1 Constant stress examples	6
2.1.1.1 Homogeneous tapered cables	6
2.1.1.2 Space elevator	9
2.1.1.3 Arches	11
2.1.1.4 Beams	14
2.1.2 Summary of the examples	17
2.2 Numerical structural optimization	20
2.2.1 Structural optimization	20
2.2.1.1 Size optimization	21
2.2.1.2 Shape optimization	21
2.2.1.3 Topology optimization	24
2.2.2 Effect of self-weight on topology optimization	32
2.2.3 Optimization in Grasshopper	35
2.2.3.1 Opossum	36
2.2.3.2 Karamba3D: Topology optimization	38
3 Analytical Derivation and Numerical Integration	40
3.1 Form of constant stress: self-weight	40
3.1.1 Analytical derivation: self-weight	40
3.1.2 FEA check: self-weight	43

3.2	Form of constant stress: uniformly distributed load q	45
3.2.1	Analytical derivation: uniformly distributed lateral load q	45
3.2.2	FEA check: uniformly distributed load q	47
3.3	Form of constant stress- load combination	48
3.3.1	Analytical derivation: constant maximum tensile stress ($\sigma = 0$)	49
3.3.2	FEA check: constant maximum tensile stress ($\sigma = 0$)	51
3.3.3	Analytical derivation: constant maximum tensile stress	52
3.3.4	FEA check: constant maximum tensile stress	55
3.3.5	Analytical derivation: constant stress on both boundaries	56
3.3.6	FEA check: zero bending moment, eccentricity + uniformly distributed load q	61
3.3.7	Analytical derivation: center line profile	61
3.3.8	FEA check: center-line profile	65
3.4	Discussion	66
3.5	Case study	69
4	Numerical structural optimization-2D	72
4.1	Validation of Grasshopper's Topology Optimization Tool	73
4.2	Topology optimization	74
4.2.1	Topology optimization model setup	75
4.2.2	Comparative results from analytical and numerical methods	76
4.3	Shape optimization	77
4.3.1	Shape optimization model setup	77
4.3.2	Penalty function	78
4.3.3	Optimized results for varying target utilization	81
4.3.3.1	Asymmetric	82
4.3.3.2	Symmetric	83
4.4	Discussion	86
5	Numerical structural optimization-3D	90
5.1	Longitudinal direction-3 types of corrugations	90
5.1.1	Individual design variables for each type of corrugations	91
5.1.2	Combine and reduce the number of variables	92
5.1.3	Interpolation function	94
5.2	Cross-section assignment	96
5.2.1	Interpolation of two shapes	96
5.2.2	Linear interpolation between control points	98

5.3	Structural optimization	99
5.3.1	FEA	100
5.3.2	Optimization and results	101
5.3.2.1	Optimization results: UC=0	102
5.3.2.2	Optimization results: UC=0.2	105
5.4	Discussion	108
6	Conclusion	113
7	Recommendation	117

List of Figures

2.1	Types of taper of the axially suspended cable, adapted from [1]	6
2.2	Forces on a tapered cable segment Δy , adapted from [1]	7
2.3	The two dimensions constant stress cable derivation, reprinted from [1]. Left: Equilibrium of a cable element. Right: General form of the constant-stress catenary: In sec x function.	9
2.4	(a) Geometry (b) Internal forces acting on an infinitesimal element, reprinted from [2] . .	10
2.5	(a) Geometry and loads (b) Internal forces acting on the center line, adapted from [3] . .	12
2.6	(a) Stand-alone, constant stress 1:20 model (b) center-line profile. Input variables for a real-size structure: $\gamma = 25kN/m^3, l = 6m, h = 6m, A_0 = 0.3m^2$, reprinted from [3]	14
2.7	Cantilever beam with a point load at the end, adapted from [4]	15
2.8	General case of a beam subjected to uniformly distributed load q , adapted from [5]	16
2.9	Visualization of $h(x)$	17
2.10	Three different structural optimization techniques, reprinted from [6]	21
2.11	Independent node movement of a hole in a plate. Left: initial design, Right: final design, reprinted from [7]	22
2.12	A typical checkerboard pattern in the ESO method, reprinted from [8]	28
2.13	Nodes located within the circular sub-domain Ω_i are used in the filter scheme for the i th element, reprinted from [8]	29
2.14	(a) the soft-kill BESO method with $q=5$ (b) the hard-kill BESO method with $q=\infinite$, reprinted from [9]	34
2.15	(a) zero self-weight (b) $F=100\%$ self-weight (c) $F=50\%$ self-weight (d) $F=10\%$ self-weight (e) self-weight only, reprinted from [9]	35
2.16	optimal topology with self-weight, hard-kill method, reprinted from [9]	35
2.17	Opossum GUI, reprinted from	37
2.18	BESO for a rectangular plate under two corner loads, reprinted from	38
3.1	Infinitesimal segment of the member	41
3.2	Static form of uniform strength: self-weight	43
3.3	Geometry model setup in Grasshopper	44

3.4	Stress result of the constant stress shape considering self-weight: Uniform compressive stress in the entire structure	45
3.5	(a) Geometry and loading (b) Form of constant maximum bending stress: uniformly distributed load q	47
3.6	Stress result of the constant stress shape considering uniformly distributed lateral load q : Uniform maximum bending stress	48
3.7	Geometry and loading: load combination	49
3.8	Form of constant 0 tensile stress: load combination	51
3.9	Results of the constant stress shape (load combination): zero tensile stress on the tension boundary	52
3.10	Result of ODE113	55
3.11	Results of the constant maximum tensile stress shape (load combination)	55
3.12	Geometry, loading and stress	57
3.13	center of mass: x_c , Eccentricity: ec	58
3.14	Visualization of Eq 3.24	60
3.15	Results of the zero moment shape	61
3.16	A segment of the center line	62
3.17	Results of the zero bending moment and constant stress shape	66
3.18	Comparison of the constant stress geometries	67
3.19	The influence of self-weight inclusion under different scales of uniformly distributed load q	68
3.20	Comparison of constant stress geometry and zero bending moment geometry	69
3.21	Sustainable noise barrier built at the InnovA58 site	71
4.1	Comparison of BESO soft-kill result from [9] example 1 and Karamba3D result	74
4.2	Comparison of BESO soft-kill results from [9] example 2 and Karamba3D result	74
4.3	The effect of defining non-design space, design domain box: $1.6 * 5m$	75
4.4	Comparison of numerical and analytical results from Sec 3.3.6	76
4.5	Polynomial approximation: coefficients as design variables	78
4.6	Demonstration of penalty function	80
4.7	Infeasible result without thickness constraint, minimum thickness: 6.3 cm, weight: 3322.8 Kg	80
4.8	Grasshopper script for shape optimization	81
4.9	Comparison of analytical derivation (left) and shape optimization (right) results: Asymmetric	82
4.10	Comparison of analytical derivation (left) and shape optimization (right) results: Symmetric	84

4.11 Comparison of analytical derivation (left) and shape optimization (right) results: Sym- metric with constant stress	85
4.12 Topology optimization and analytical from of zero-bending moment	88
5.1 Relationships of variables: circular and trapezoidal shape	93
5.2 Relationships of variables: circular and sinusoidal shape	94
5.3 Interpolation function	95
5.4 Three types of corrugated shape with the same scale	95
5.5 Five control points on the longitudinal curve	97
5.6 First two graph taken from Fig4.2, referred to as Shape 1 and Shape 2	97
5.7 Interpolation of two base cross-sections	98
5.8 Example of the linear interpolation	99
5.9 Boundary conditions and load case of the structural model	101
5.10 Seven design variables in the 3D model	102
5.11 Illustration of optimized geometry with UC=0, top view and perspective view	104
5.12 First principal stress in the upper boundary layer, UC=0	105
5.13 Illustration of optimized geometry with UC=0.2, top view and perspective view	107
5.14 First principal stress in the upper boundary layer, UC=0.2	108
5.15 Front view of the straight wall with cross-section Shape 1: principal stress one in the upper boundary layer in tension	109
5.16 Comparison of bending moment between straight and corrugated longitudinal profiles . .	110
5.17 Material savings of the optimal results with desired utility 0 and 0.2	111

List of Tables

2.1	Constant stress examples: Type 1	17
2.2	Constant stress examples: Type 2	18
2.3	Constant stress examples: Type 3	19
3.1	Input values to the variables in Eq 3.4	42
3.2	Input components for Karamba3D: self-weight	44
3.3	Input values to the variables in Eq 3.7	46
3.4	Input components for Karamba3D: uniformly distributed load q	48
3.5	Input values to the variables in Eq 3.11	51
3.6	Input components for Karamba3D: load combination	52
3.7	Input y and output h	54
4.1	Numerical shape optimization: Asymmetric shape	83
4.2	Numerical shape optimization: Symmetric shape	86
5.1	Three corrugated shapes and variables	92
5.2	Optimized design variables for longitudinal profile, $UC=0$	103
5.3	Optimized design variables for cross-sections at control points A and B, $UC=0$	103
5.4	Optimized design variables for longitudinal profile, $UC=0.2$	106
5.5	Optimized design variables for cross-sections at control points A and B, $UC=0.2$	106

Summary

Traditional noise barriers often rely on outdated design techniques and resource-intensive materials like concrete and steel, however, with sustainability gaining importance, there is a need to align noise barrier design with green construction principles. One of the most promising ways to mitigate the environmental impact is through structural optimization aimed at reducing material usage for construction. Therefore, the main research question is: What is the optimal geometry of the noise barrier made of a low tensile strength material, in two dimensions and three dimensions under self-weight and uniformly distributed lateral load?

The overall methodology employed to address the research questions consists of several key steps. Firstly, the process begins with a two-dimensional analytical form-finding aimed at deriving optimal cross-sections for the noise barrier. Apply the concept of uniform strength theory, which is a design approach renowned for its capacity to yield structures with the utmost material efficiency, to attain constant (maximum) stress shapes. These mathematical solutions are validated by Finite Element Analysis (FEA) to ensure they meet the predefined stress criteria. Subsequently, numerical structural optimization is performed to obtain the minimum weight geometries while adhering to stress constraints through the utilization of a penalty function. A crucial aspect involves comparing the numerically optimized geometries with the analytical solutions. The significant resemblance between these outcomes serves to confirm the accuracy and reliability of the numerical optimization framework, also mutually proving the fact that they represent optimal geometries. Ultimately, this validated optimization model is extended into three dimensions, enabling the exploration of the minimum weight combination of the longitudinal profile and the assigned varying cross-section along the noise barrier.

Analytical solutions describing the 2D uniform strength cross-sections of a noise barrier differ under varying load conditions. The constant stress shape stemming from self-weight exhibited an exponential function. This exponential progression of thickness along the central axis, from top to bottom, ensures uniform compressive stress throughout the structure, implying a full utilization of the material when the specified constant stress is the maximum allowable compressive stress in the structure. On the other hand, while considering a uniformly distributed lateral load, the solution displayed a linear function.

Both the tension and compression boundaries along the height possess constant maximum bending stress. Lastly, the load combination of self-weight and uniformly distributed lateral load generates two distinctive symmetric geometries, dictated by the specified constant maximum tensile stress on the tension boundary: zero or non-zero. The square root function ensures constant zero tensile stress along the height of the tension boundary. The benefit of this solution is that it eliminates the necessity for additional structural elements like reinforcement or foundation, particularly when using materials with low tensile strength for constructing the noise barrier, thanks to the absence of tensile stress. On the contrary, when a non-zero constant maximum tensile stress is specified for the tension boundary, it results in a linear geometry similar to the case of considering only uniformly distributed loads. In this situation, the inclusion of self-weight compensates for tensile bending stress from the lateral load and slightly reduces material requirements, yet the impact is negligible. Another scenario considering load combination involves an asymmetrical shape with zero bending moment in the structure. This is achieved by leveraging the bending moment generated by the eccentricity of self-weight to counterbalance the bending moment from lateral loads. However, this asymmetry may not be practically viable in real-world scenarios where loads can originate from opposite directions.

The two-dimensional numerical structural optimization effectively integrated topology optimization and shape optimization. Starting with topology optimization, it created a preliminary design for the optimal material distribution within a rectangular box under self-weight and uniformly distributed lateral load from one side. The result closely resembles the asymmetric analytical solution. Following this, shape optimization was applied to further refine and control the geometries, building on the topology-optimized result. The iterative shape optimization process consists of three main components: 1) parametrically describing the geometry using three coefficients of a second-order polynomial, ensuring a smooth boundary shape; 2) conducting structural analysis using FEA tool Karamba3D, which employed a beam element with a moment fixed connection at the bottom end subjected to a load combination; 3) implementing an optimization algorithm with the goal of minimizing weight, and incorporating stress constraints using a penalty function that can efficiently eliminate candidates violating specified constraints. The numerical model successfully produced optimal cross-sections that closely matched analytical solutions considering load combinations. This indicates that both analytical form-finding based on uniform strength theory and numerical structural optimization aimed at minimizing weight can achieve optimal geometries, reinforcing each other's validity.

The validated two-dimensional numerical optimization framework was expanded into three dimensions with two main differences in the structural model. Firstly, the beam element was substituted by the 3-node shear-deformable isotropic flat shell element. Additionally, all the rotational degrees of freedom were released at the bottom support, allowing for the generation of a corrugated longitudinal profile, pos-

sessing sufficient inherent bending stiffness and obviating the need for the previously used moment-fixed connection at the bottom. The corrugated shape offered the advantage of reducing the required cross-sectional area along the longitudinal direction due to the substantial decrease in bending stress within the structure. The optimal cross-sections derived from the 2D optimization formed the foundational shapes assigned along the noise barrier, with the optimization algorithm further decreasing their dimensions to achieve minimum weight structure respecting stress constraint. In scenarios where the desired maximum tensile stress is zero, the resulting minimum weight configuration exhibited a "semi-circle" corrugated longitudinal geometry. This shape showcased optimal efficiency with the highest bending stiffness, translating into a material savings of 22.6%. Conversely, when the specified maximum tensile stress allows a non-zero value, a sinusoidal wave shape outperformed the semi-circle profile in weight reduction, achieving a remarkable 60.5% material savings. The effectiveness of the 3D structural optimization process was underscored by the substantial material savings achieved when compared to non-optimized reference models.

In conclusion, this research provides significant insights into the optimal geometries of free-standing structures, demonstrating the efficacy of both analytical and numerical approaches. Importantly, the numerical optimization framework has been shown to be highly efficient and accurate, requiring remarkably short computational times while delivering impressive results.

Chapter 1

Introduction

In recent years, sustainability has become an increasingly important topic, driving the need for more environmentally-friendly construction practices. Structural optimization, aimed at reducing material usage, has shown promise in mitigating the environmental impact of construction projects. The Netherlands, facing substantial infrastructure development, has a high demand for noise barriers to create livable urban spaces. However, traditional noise barrier designs relying on outdated techniques and resource-intensive materials like concrete and steel pose sustainability challenges, urging the need for greener solutions.

To address these challenges, innovative concepts such as robotic shot earth fabrication and structurally optimized geometry are being integrated into noise barrier design, aiming to preserve acoustic performance while reducing environmental impact. Inspired by these advancements, this thesis explores novel approaches to noise barrier design, seeking to minimize material usage by optimizing its shape to efficiently handle gravity load and uniformly distributed load.

Efficient and effective use of the material is essential in designing a structure that can deliver optimal load-carrying performance. Achieving an optimal shape can be realized through analytical and numerical methods. One widely-adopted analytical concept is uniform strength theory with the design criterion of constant stress. This design principle draws inspiration from natural structures like trees and bones, known for their highly optimized forms characterized by a minimum stress response to loading.

Numerical structural optimization, on the other hand, involves defining objectives, constraints, and design variables to achieve the desired design outcome. Objectives could include minimizing the structure's weight, maximizing its stiffness, or minimizing the stresses or strains under certain load cases. Constraints may include limits on the maximum allowable displacement or stress, or geometric constraints such as maximum and minimum thicknesses or curvature limits. Design variables could include parameters that

define the geometry or material properties of the structure.

On the other hand, numerical structural optimization involves defining design variables, objectives, and constraints to attain the desired outcome. Design variables encompass parameters defining geometry, load case, and material properties. Objectives may include weight minimization, stiffness maximization, or stress/strain minimization under specific loads. Constraints encompass maximum allowable displacement, stress, or geometric limitations like thickness and curvature bounds.

To find the optimal shape of a noise barrier, this paper will explore using these approaches to optimize the structure. Also, compare the results of analytical and numerical approaches, and address the optimization process and constraints involved in achieving an optimal design

This paper aims to explore these approaches in finding the optimal shape for a free-standing noise barrier under various load conditions, encompassing two and three dimensions. The study will compare results from analytical and numerical methods, highlighting the optimization processes and constraints involved in achieving an optimal design.

1.1 Problem statement and research objectives

The main research question of this research is:

What is the optimal geometry, encompassing cross-section and longitudinal profile, of a noise barrier (namely a free-standing wall) made of a low tensile strength material, when considering self-weight and exposure to uniformly distributed lateral load?

To address the main research question, the following three sub-questions are formulated:

1. Can analytical form-finding based on uniform strength theory be effectively utilized to determine optimal structural geometries under specific load conditions?
2. Can numerical structural optimization, starting from a basic shape without any foundational understanding, efficiently transform it into the optimal geometry that closely resembles analytical solutions, employing a distinct strategy focused on minimizing weight under specified stress constraints?
3. When extending to three dimensions, is it feasible to adjust the longitudinal profile of the noise barrier to enhance its bending stiffness against out-of-plane load?

The primary objective of this research is to determine the most efficient and sustainable design for a noise barrier, which minimizes material usage while ensuring sufficient load-carrying capacity and structural performance. The ultimate goal is to contribute to the development of environmentally friendly and highly optimized noise barriers, promoting sustainable urban environments. Additionally, a secondary objective of the research is to develop a practical numerical optimization framework capable of generating

an optimal design that aligns with the results obtained through analytical derivation, thereby validating the effectiveness and reliability of the proposed numerical methodology.

1.2 Thesis structure and research methodology

The following section provides a clear overview of the purposes and steps of each chapter.

Chapter 2 - Literature review

The purpose of this chapter is to provide background knowledge on analytical form-finding and numerical form-finding.

Analytical form-finding:

Introduce the concept of uniform strength theory and explores various examples, such as tapered cables and space elevators, constant stress arches, and constant maximum stress beams.

Numerical form-finding:

Investigate different approaches to the optimization problem to identify the most suitable framework for addressing the research problem. Additionally, it introduces the background knowledge of optimization Grasshopper plug-ins.

Chapter 3 - Analytical derivation and Numerical integration

This chapter presents the analytical derivation process for constant stress 2D cross-sections under various load cases.

Uniform strength theory derivation:

Develop the equilibrium equations governing the form of constant stress shapes. Two load cases consider self-weight and uniformly distributed load individually. One load combination considers self-weight and uniformly distributed load.

FEA validation:

FEA is conducted to verify the accuracy of the analytical solutions and ensure that the derived shapes meet the specified criteria.

Chapter 4 - Numerical structural optimization in two dimensions

Topology optimization serves as the initial step to gain insights into the optimal material distribution, while shape optimization follows to refine the topology-optimized outcome based on stress constraints.

The purpose of these numerical methods is to generate results that can be compared to the analytical solutions, thereby demonstrating the capability and reliability of the numerical framework.

Topology optimization:

Topology optimization aims to find the optimal material distribution. However, there are limitations in including self-weight in the iterations, making it essential to validate the chosen tool's capacity to incorporate self-weight.

Shape optimization:

The shape optimization design process consists of three main components: 1.) A parameterized geometry description of the design space, 2.) A numerical structural analysis (FEA), and 3.) The optimization algorithm with objective function and penalty function to incorporate constraints. The primary objective in this phase is to develop an efficient parametric model that encompasses all three aspects mentioned above.

Chapter 5 - Numerical structural optimization in three dimensions

The numerical structural optimization expands into three dimensions to determine the optimal geometry of the noise barrier, encompassing both the longitudinal profile and cross-sections.

Longitudinal direction:

Three different corrugated shapes are investigated to identify the most effective design in terms of bending capacity.

Cross-section assignment:

The cross-sections obtained from the 2D numerical optimization serve as the initial shapes. The optimization algorithm gradually reduces the cross-sectional area while simultaneously adjusting the longitudinal profile to achieve an optimal design.

Chapter 6-Conclusion

Present research findings on optimal noise barrier geometries through analytical derivation and numerical structural optimization. The study demonstrates the efficacy of these methodologies in achieving material savings and ensuring structural performance.

Chapter 7 - Recommendation

Provide recommendations for future research: explore higher-order polynomial representations, incorporate topology optimization in 3D framework and so on.

Chapter 2

Literature review

Chapter 2 addresses the relevant background knowledge of the research.

2.1 Analytical form finding

Analytical form finding is an approach used in structural engineering to predict the geometrical optimal shape and size of a structure based on its intended function and performance requirements. [10] This process typically involves deriving the shape from a mathematical model of the structure using various analytical techniques, such as equilibrium equations and energy methods.

The objective of analytical form finding can be minimizing the stress response of the structure under certain load cases while satisfying other design constraints such as cost and weight. This can be accomplished by adjusting the shape, size, material stiffness, or a combination of these factors, to achieve an optimal balance of performance and efficiency.

The concept of finding a structurally optimal shape through analytical approaches has been in use for a considerable length of time. Dates back to 1691, Bernoulli proposed the problem of hanging cable and solved it with calculus. The solution results in the famous form of 'catenary'. In 1947, Landweber [11] published his work on cable functions, which helps to determine the tensile stress in the cable when it's loaded with uniform current underwater. In 1953, Ramsey [12] also found the geometrical configurations of a chain and elastic string with analytical treatment. He derived the form of a parabola when the string is loaded with a point load along its length, in the meantime, he adopted the concept of uniform strength and discovered the cross-sectional area should be in proportion to the level of tension.

Develop upon the concept of analytical form finding, uniform strength theory is a structural design criterion that aims to ensure all parts of a structure are equally stressed (constant stress) under a

specific load case. [3] The specified constant stress in the entire member is generally the maximum allowable stress of the material. In this way, it guarantees full utilization of the structure. This approach is inspired by natural structures such as trees and bones which are known to be highly optimized and exhibit a minimal stress response to loading.

2.1.1 Constant stress examples

Various examples listed below adopt the concept of uniform strength theory for analytical form finding. All of them show that according to the criterion of constant stress along the cross-section under prevalent load, the derived shape has the most optimized structural performance and the most efficient use of the materials.

2.1.1.1 Homogeneous tapered cables

[1] explore the concept of tapered cable with constant stress criterion. Equilibrium equations, governing the static geometry which a tapered cable complies with, were developed for two common cases of cable application, namely the axially suspended (Fig 2.1 and Fig 2.2), and catenary cables (Fig 2.3). Fig 2.1 shows the different types of taper under the self-weight of the cable when it's supported at the top end, while Fig 2.3 depicts the constant stress catenary function when the cable is loaded by self-weight w and supported in two dimensions.

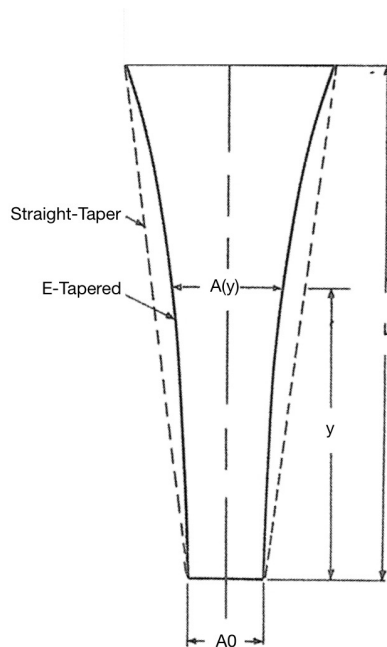


Figure 2.1: Types of taper of the axially suspended cable, adapted from [1]

The E-Tapered shown in Fig 2.1 was derived with the use of constant stress theory. It assumed a vertical

axially suspended cable geometry and the only external loading acting on the cable is its self-weight. From the basic equilibrium in Eq 2.1, which means the increase of axial force in the cable comes from the weight of an infinitesimal element dy , see Fig 2.2.

$$dT = \gamma A dy \quad (2.1)$$

At any point, the cross-sectional area A can be substituted by the relation of $A = \frac{T}{\sigma}$, where σ represents the constant stress. After the substitution, the static equilibrium Eq 2.1 can be further simplified and gives the following expression of area:

$$A(y) = A_0 e^{\frac{\gamma y}{\sigma}} \quad (2.2)$$

where : $\sigma =$ constant stress

$\gamma =$ specific weight

$A_0 =$ area at the bottom ($y=0$)

Eq 2.2 shows that when the cross-sectional area of the cable geometry increases exponentially from the bottom to the top, the axial stress results from self-weight remains constant σ .

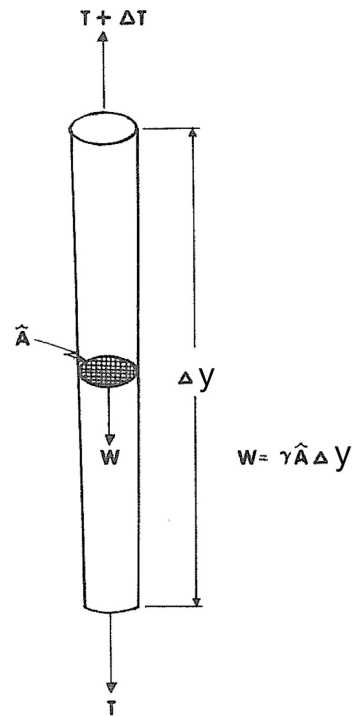


Figure 2.2: Forces on a tapered cable segment Δy , adapted from [1]

The second case in the paper considered the cable to be suspended in a two-dimensional manner. The cable is supported between two points with a horizontal distance and loaded with its self-weight only. From the left picture in Fig 2.3, static force equilibrium and moment equilibrium can be listed with a vectorial format, see Eq 2.3 and Eq 2.4.

$$\sum \vec{F} = 0$$

$$-\vec{T} + (\vec{T} + \Delta\vec{T}) + \vec{w}\Delta s = 0 \quad (2.3)$$

$$\sum \vec{M}_o = 0$$

$$\vec{r} * -\vec{T} + (\vec{r} + \Delta\vec{r}) * (\vec{T} + \Delta\vec{T}) + r_w * \vec{w}\Delta s = 0 \quad (2.4)$$

Different from the first part, the form of the cable that conforms to the criterion of constant stress should be derived first, that is the center line profile of the cable shown in Eq 2.5. After that, the varying area along the cable center axis can then be derived, see Eq 2.6. Both the equations are derived from the basic equilibrium Eq 2.3 and Eq 2.4.

$$y = \frac{\sigma}{\gamma} \ln \sec \frac{\gamma x}{\sigma} \quad (2.5)$$

$$A(s) = \frac{T_H}{\sigma} \cosh \frac{\gamma s}{\sigma} \quad (2.6)$$

where : T_H = axial horizontal force in the cable

s = corordinate along the cable in 2D

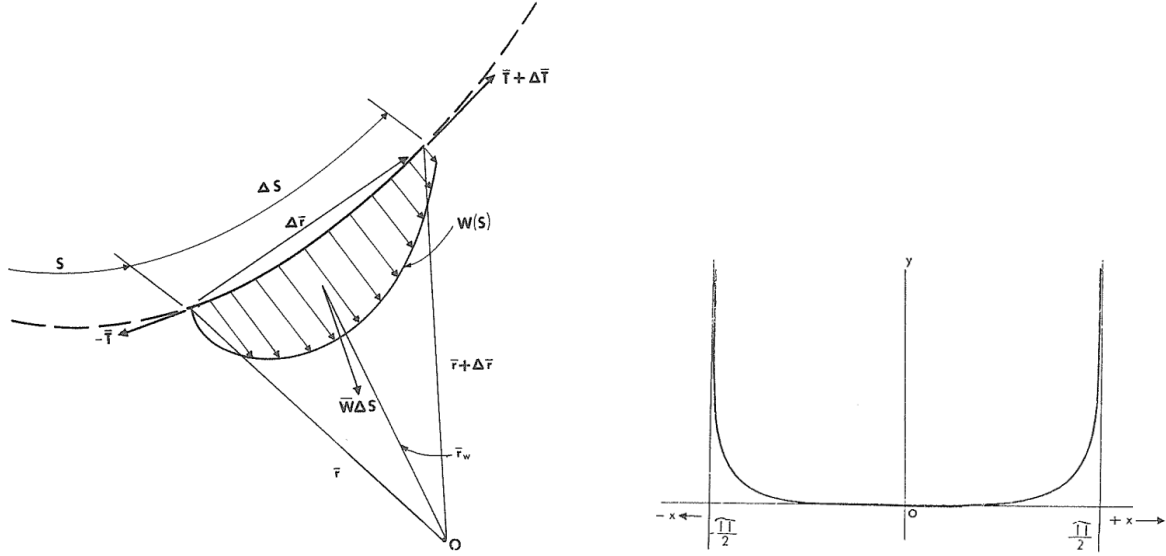


Figure 2.3: The two dimensions constant stress cable derivation, reprinted from [1]. Left: Equilibrium of a cable element. Right: General form of the constant-stress catenary: $\ln \sec x$ function.

These equations were subsequently utilized to compare the performance of the optimum, tapered cable against the conventional constant diameter cable. The advantages and disadvantages of tapered cables are summarized in the paper.

2.1.1.2 Space elevator

The objective of [2] is to find a different design for the space elevator that can avoid excessive stress occurring in the structure. The proposed solution employs the constant stress concept and gives a varied cross-section along the height of the elevator, which guarantees the tensile stress in the structure remains uniform.

The force acting on an infinitesimal element of the space elevator includes W (weight of the element), FC (outward centrifugal force), FU (upward force results from the portion of cable above the element), and FD (downward force results from the portion of cable below the element). The equilibrium equation gives: $FU + FC - FD - W = 0$. The elevator remains in tension along the entire length, and the varying tensile force adjusts in a way that the four forces are always in equilibrium for each element, see Fig 2.4. The element at a distance of the radius of the geostationary orbit, the weight and centrifugal forces are equal ($W=FC$). Accordingly, the tension forces at both ends must also be equal ($FU=FD$). If the element is below geostationary height, the weight force (W) exceeds the centrifugal force (FC), which requires $FU > FD$ for equilibrium. This implies that the tension in the tower increases with a height from ground level to geostationary height. Conversely, if the element is above geostationary height, the centrifugal force (FC) exceeds the weight force (W), requiring $FU < FD$ for equilibrium, so the tension in the tower decreases with height. A free-standing structure has zero tension at both ends, and no restraint is needed

to keep it in place. Therefore, the tension in a free-standing space elevator rises from zero at ground level to a maximum value at geostationary height and then decreases to zero again at the upper end. With this qualitative understanding, the author determined the quantitative variation of the tension in the tower with height.

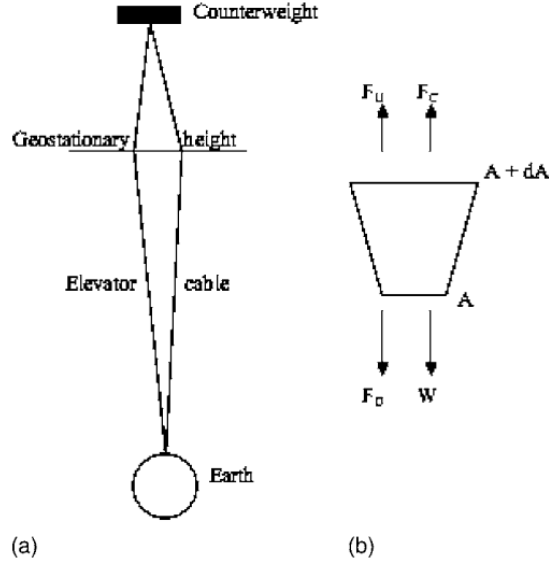


Figure 2.4: (a) Geometry (b) Internal forces acting on an infinitesimal element, reprinted from [2]

To derive the analytical solution that describes the geometry, the equilibrium equation can be rearranged as $F_U - F_D = W - F_C$, see Fig 2.4. Similar to Eq 2.1, the equilibrium means the increase of axial force in the structure ($F_U - F_D$) comes from the weight of the infinitesimal element ($W - F_C$). $F_U - F_D$ can be written as σdA with σ being the constant stress in the structure and dA being the increase of the area of the element. With the explicit expression of W and F_C substituted, the equilibrium becomes:

$$\sigma dA = \frac{A\rho g R^2}{y^2} dy - \frac{A\rho g R^2 y}{R_g^3} dy \quad (2.7)$$

where : σ = constant stress in the elevator

ρ = mass density

g = acceleration of gravity at Earth's surface

y = distance of a point on the elevator from Earth's center

R = Earth's radius

R_g = radius of geostationary orbit

From the basic equilibrium in Eq 2.7, and substitute ρg with γ (specific weight), the following relation of the area can be derived.

$$A(y) = A_0 e^{\frac{\gamma R^2}{\sigma} \left(\frac{1}{R} + \frac{R^2}{2Rg} - \frac{1}{y} - \frac{y^2}{2Rg} \right)} \quad (2.8)$$

where : A_0 = area at $y=R$

γ = specific weight

As it can be seen in Eq 2.8, the area along the elevator $A(y)$ exhibits exponential growth from ground level to geostationary height, followed by exponential decay beyond the geostationary height.

2.1.1.3 Arches

During the seventeenth century, it was discovered that the zero-moment arch shape, also known as a funicular arch, is similar to the shape of an inverted suspension chain, demonstrated by Hooke through the experimental form-finding method [13]. [10] presents a mathematical model predicting the geometrical configuration of a constant cross-section arch by imposing the moment-less condition, in order for such structures to undergo only axial stresses when subjected to permanent loads. Expanding on the previous work, [14] introduces a novel analytical approach for determining the optimal shape of a plane statically determined arch with constant stress cross-section. Building upon the classic problem of a catenary under self-weight, this study extends the analysis to include an inverted catenary under both self-weight and given vertical load distribution. The results indicate the existence of a specific set of analytical solutions that correspond to the minimum ratio of the self-weight to the total applied load, in contrast to previous proposals. The paper derives the center line profile and the changing cross-sectional area of the arch by specifying each cross-section is subject to constant axial compressive stress. Also, for the arch-shape solution, it's necessary to impose the design criterion of zero bending moments and zero shear stress in the entire structure.

Similar to [14], [3] presents a theory that encompasses an extensive range of asymmetric arch configurations and provides a comprehensive derivation of the equation governing the center-line profile, cross-section area, and horizontal reactions of the arch, see the pin-ended arch geometry in Fig 2.5. The design criteria are the same as [14]. Subsequently, symmetric arches are analyzed, and a new concept of including a solution for achieving the least weight by determining the equation for a volume-minimizing, the span-to-rise ratio is also presented.

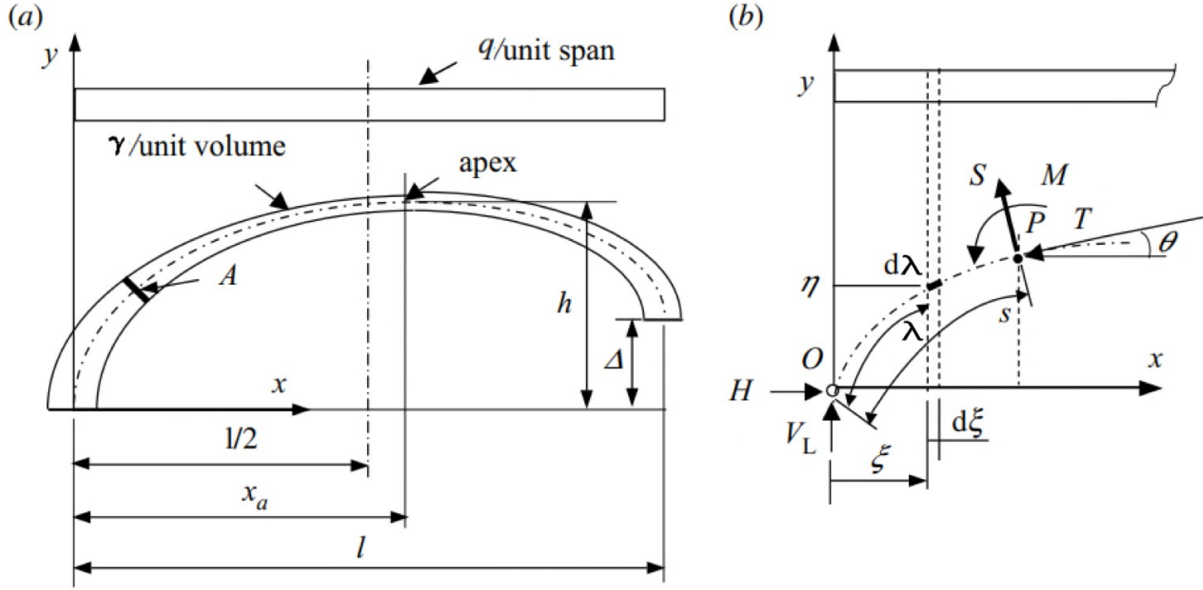


Figure 2.5: (a) Geometry and loads (b) Internal forces acting on the center line, adapted from [3]

The picture on the right-hand side in Fig 2.5 shows the forces acting on the arch, and the coordinate systems used during the derivation process. An arbitrary point between point O and P has coordinates (ξ, η) , and arch length, λ , measured from O . s is the local coordinate along the arch in 2D. Three basic equilibrium equations can be listed based on Fig 2.5 (b) :

1. Vertical equilibrium, $\sum F_V = 0$:

$$-T \sin \theta + S \cos \theta - qx - \int_0^s \gamma A d\lambda + V_L = 0 \quad (2.9)$$

where : T = compressive force in the arch

S = shear force in the arch

q = external load per unit span

γ = specific weight

V_L = vertical reaction force at left end

2. Horizontal equilibrium, $\sum F_H = 0$:

$$-T \cos \theta - S \sin \theta + H = 0 \quad (2.10)$$

where : H = horizontal reaction force at left end

3. Moment equilibrium at point P, $\sum M_p = 0$:

$$M + Hy - V_L x + \frac{qx^2}{2} + \int_0^s \gamma A(x - \xi) d\lambda = 0 \quad (2.11)$$

where : M = bending moment in the arch

As mentioned above, the equation governing the center-line profile, $y = f(x)$, cross-section area $A(x)$, and horizontal reactions of the arch H , can be derived from the three basic equilibrium equations, Eq 2.9 to Eq 2.11. However, some middle products are necessary beforehand, including x_a , the x value of the apex, and A_0 , the cross-sectional area at the apex:

$$x_a = \frac{\cos^{-1}(e^{-\mu h})}{\cos^{-1}(e^{-\mu(h-\Delta)}) + \cos^{-1}(e^{-\mu h})} l \quad (2.12)$$

$$\text{where : } \mu = \frac{\gamma}{\sigma}$$

σ = constant stress

h = y value of the apex

Δ = y value of the right end point

$$A_0 = \frac{\gamma q}{\left(\frac{\sigma}{x_a} \cos^{-1}(e^{-\mu h})\right)^2 - \gamma^2} \quad (2.13)$$

With Eq 2.12 and Eq 2.13, the center line profile and the area can be expressed as:

$$y = h + \frac{1}{\mu} \ln \cos\left(\frac{1}{x_a} \cos^{-1}(e^{-\mu h})(x - x_a)\right) \quad (2.14)$$

$$A = A_0 \sqrt{1 + \frac{\kappa}{\mu} \tan^2[\sqrt{\mu\kappa}(x - x_a)]} \quad (2.15)$$

$$\text{where : } \mu = \frac{\gamma}{\sigma}$$

$$\kappa = \mu \left(1 + \frac{q/\gamma}{A_0} \right)$$

It's worth mentioning that the center-line profile, Eq 2.14, is independent of the external load, q . This has been previously proved in [15]. The visualization of the arch can be seen in Fig 2.6.

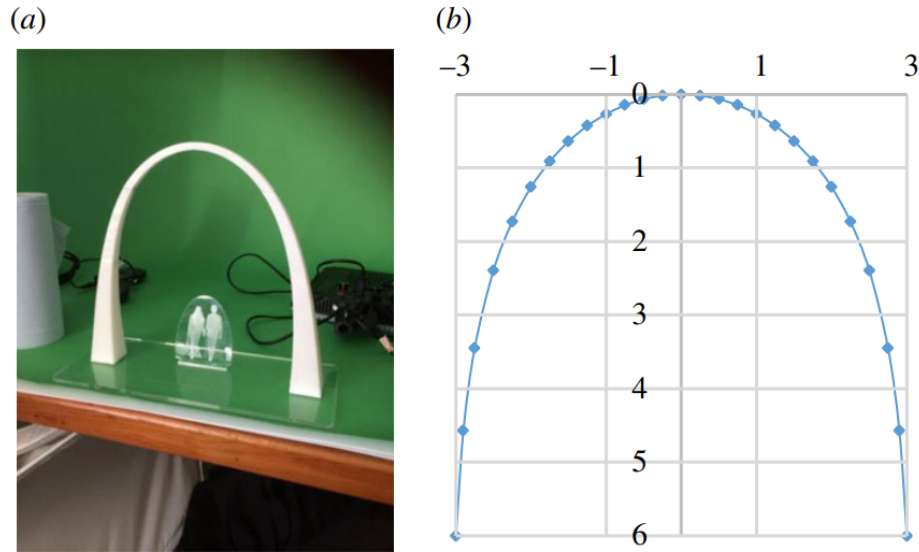


Figure 2.6: (a) Stand-alone, constant stress 1:20 model (b) center-line profile. Input variables for a real-size structure: $\gamma = 25kN/m^3$, $l = 6m$, $h = 6m$, $A_0 = 0.3m^2$, reprinted from [3]

2.1.1.4 Beams

Timoshenko [4] proposed that the distance from the neutral axis of the beam to the most remote fibers in the tension and compression side should have the same ratio of the tensile strength to the compressive strength of the material to maintain uniform strength.

The maximum bending stress depends upon the section modulus of the beam. Accordingly, consider a uniform-strength cantilever beam subjected to a vertical point load at the free end to provide bending, the resulting shape is non-prismatic with varying cross-sections, see Fig 2.7.

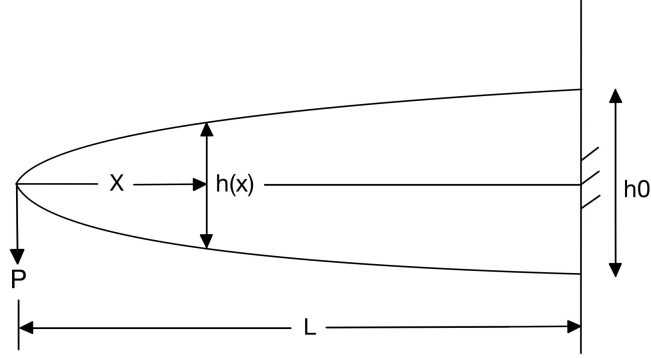


Figure 2.7: Cantilever beam with a point load at the end, adapted from [4]

The bending moment at distance x along the beam axis from the free end is Px . In order to maintain constant maximum bending stress at the extreme fibre of the beam, the section modulus should vary along the beam in the same proportion as the bending moment, the following equation is valid for the beam with constant width b (perpendicular to the plane of the paper) and variable depth $h(x)$ at x :

$$\frac{M}{S} = \frac{6Px}{bh(x)^2} = \frac{6PL}{bh_0^2} = \sigma \quad (2.16)$$

where : M = bending moment

S = section modulus

L = length of the cantilever beam

h_0 = depth at $x=L$

σ = constant maximum bending stress

Solve $h(x)$, and Eq 2.17 holds.

$$h(x) = h_0 \sqrt{\frac{x}{L}} \quad (2.17)$$

$$\text{where : } h_0 = \sqrt{\frac{6PL}{b\sigma}}$$

The shape of $h(x)$ is shown in Fig 2.7 and follows a parabolic function. The cross-sectional area at the loaded end of the cantilever beam is zero due to the neglect of shear stress in the derivation. However,

in practical applications, it is necessary to consider this stress and give appropriate tip thickness in the shape at the loaded end to ensure that there is enough cross-sectional area to transmit the shear force.

Extend from [4], some literature further includes the self-weight of the beam to establish equilibrium equations and give solutions to particular cases. [16] and [5] derive an analytical solution for beams of uniform strength considering self-weight and the specified uniformly distributed load.

The papers also discuss different possibilities, including constant depth with various widths or constant width with various depths, to achieve uniform strength in the given boundary condition, like simply supported, cantilever, or fixed beam.

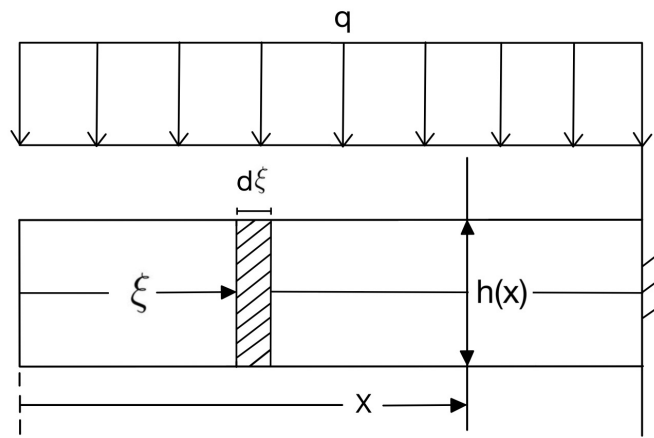


Figure 2.8: General case of a beam subjected to uniformly distributed load q , adapted from [5]

Fig 2.8 shows a beam that is subjected to uniformly distributed load q . With constant width, variable depth $h(x)$ and the boundary condition is cantilever, constant σ multiplied by section modulus should equal to bending moment from the self-weight of the beam and from uniformly distributed load q . The defining equation is:

$$\sigma \frac{bh(x)^2}{6} = \frac{qx^2}{2} + \gamma b \int_0^x h(\xi)(x - \xi)d\xi \quad (2.18)$$

From Eq 2.18, $h(x)$ can be derived after some math manipulations.

$$h(x) = \frac{\gamma x^2}{2\sigma} + \sqrt{\frac{3q}{\sigma b}} x \quad (2.19)$$

To visualize the shape of a cantilever beam of constant maximum bending stress under self-weight and an external load q , Eq 2.19 was plotted with Maple. The symbolic variables are the properties of C20/25 concrete with: $\gamma = 25kN/m^3$, $\sigma = 1300kN/m^2$. While q load is $2kN/m$. The generated shape is shown

in Fig 2.9.

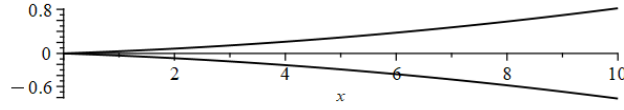


Figure 2.9: Visualization of $h(x)$

2.1.2 Summary of the examples

The examples presented in the previous Sec 2.1.1 can be classified into three types.

1.

The first type of the examples examines structures subject to axial forces and satisfies the constant stress condition throughout the structure. The equilibrium equations demonstrate that the increase of the axial force is attributed to the weight of the infinitesimal segment. The term $e^{\frac{\gamma}{\sigma}}$ shows in the results if there are only axial forces present in the structure.

	Loads	Equilibrium	Shape
	Self-weight W	$dT = \gamma A dy$ $dT = \sigma dA$	$A(y) = A_0 e^{\frac{\gamma y}{\sigma}}$ $\sigma = \text{constant stress}$ $\gamma = \text{specific weight}$ $A_0 = \text{area at the bottom } (y=0)$
	W, FC, FU, FD W : self-weight FC : centrifugal FU : upward force results from the portion of cable above the element FD : downward force results from the portion of cable below the element	$FU-FD = W-FC$ $FU-FD = \sigma dA$	$A(y) = A_0 e^{\frac{\gamma R^2}{\sigma} (\frac{1}{R} + \frac{R^2}{2R_g^2} - \frac{1}{y} - \frac{y^2}{2R^3})}$ $\sigma = \text{constant stress}$ $\gamma = \text{specific weight}$ $A_0 = \text{area at } y=R$ $y = \text{distance from Earth's center}$ $R = \text{Earth's radius}$ $R_g = \text{radius of geostationary orbit}$

Table 2.1: Constant stress examples: Type 1

2.

As described in [1], a homogeneous cable of constant diameter hanging under its own weight takes the form of a catenary when supported by the two endpoints. The basic two-dimensional catenary

function $y = a \cosh \frac{x}{a}$ describes the fundamental geometric shape. On top of that, if add the constant stress condition to the fundamental shape, it's necessary to derive the new center line profile, constant-stress catenary, and tapered cross-sections. The general mathematical form $y = \frac{\sigma}{\gamma} \ln \sec \frac{\gamma x}{\sigma}$ defines the geometrical form of the constant-stress catenary. Similar to the two-dimensional hanging cable example, the arch example has the same inverted catenary function, when considering a rigid, two-pin, moment-less arch with a constant diameter cross-section under self-weight [10]. Adding the condition of constant stress as the criterion, the result shows a similar fundamental form: $y = h + \frac{\sigma}{\gamma} \ln \cos \frac{\gamma x}{\sigma}$, if specifies a symmetric form under self-weight.

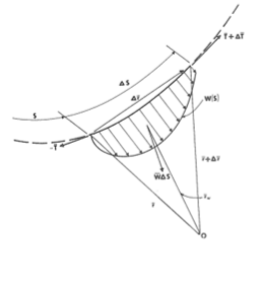
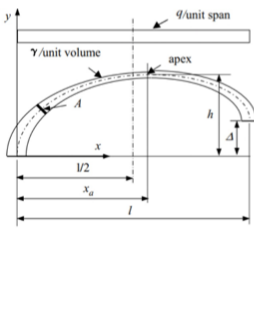
	Loads	Equilibrium	Shape
	self-weight W	$\sum \vec{F} = 0$ $-\vec{T} + (\vec{T} + \Delta\vec{T}) + \vec{w}\Delta s = 0$ $\sum \vec{M}_o = 0$ $\vec{r} * -\vec{T} + (\vec{r} + \Delta\vec{r}) * (\vec{T} + \Delta\vec{T}) + \vec{r}_w * \vec{w}\Delta s = 0$	$y = \frac{\sigma}{\gamma} \ln \sec \frac{\gamma x}{\sigma}$ $A(s) = \frac{T_H}{\sigma} \cosh \frac{\gamma s}{\sigma}$ <p>T_H = axial horizontal force in the cable s = corordinate along the cable</p>
	self-weight + external load q	$\sum F_V = 0$ $-T \sin \theta + S \cos \theta - qx - \int_0^s \gamma A d\lambda + V_L = 0$ $\sum F_H = 0$ $-T \cos \theta - S \sin \theta + H = 0$ $\sum M_p = 0$ $M + Hy - V_L x + \frac{qx^2}{2} + \int_0^s \gamma A(x - \xi) d\lambda = 0$	$y = h + \frac{1}{\mu} \ln \cos \left(\frac{1}{x_a} \cos^{-1}(e^{-\mu h})(x - x_a) \right)$ $A = A_0 \sqrt{1 + \frac{\kappa}{\mu} \tan^2[\sqrt{\mu\kappa}(x - x_a)]}$ $\mu = \frac{\gamma}{\sigma}$ $\kappa = \mu \left(1 + \frac{q/\gamma}{A_0} \right)$

Table 2.2: Constant stress examples: Type 2

3.

The third type of constant stress example considers cantilever beams subjected to forces that induce a bending moment in them. The criterion is that the maximum bending stress remains constant along the beam axis. The results indicate that the relationship between the shape and the x-axis is determined by taking half the exponent of the x in the bending moment expression. For instance, in the case of a point load P applied on the free end of the beam resulting in a bending moment of Px , the exponent of x is 1, which when divided by 2 becomes $\frac{1}{2}$. Therefore, it shows a square root function of x, \sqrt{x} , in the result.

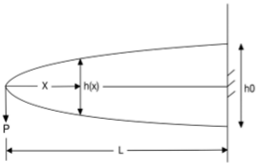
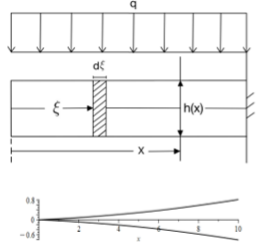
	Loads	Equilibrium	Shape
	Point load P	$\frac{M}{S} = \frac{6Px}{bh(x)^2} = \frac{6PL}{bh_0^2} = \sigma$ <p> M = bending moment S = section modulus L = length of the cantilever beam h_0 = depth at $x=L$ σ = constant maximum bending stress </p>	$h(x) = h_0 \sqrt{\frac{x}{L}}$ $h_0 = \sqrt{\frac{6PL}{b\sigma}}$
 <p>Figure 2.9: Visualization of $h(x)$</p>	Self-weight + External load q	$\sigma \cdot S = M$ $\sigma \frac{bh(x)^2}{6} = \frac{qx^2}{2} + \gamma b \int_0^x h(\xi)(x - \xi)d\xi$	$h(x) = \frac{\gamma x^2}{2\sigma} + \sqrt{\frac{3q}{\sigma b}} x$

Table 2.3: Constant stress examples: Type 3

2.2 Numerical structural optimization

This chapter provides an overview of the relevant literature on numerical structural optimization techniques. It begins by discussing different methods for structural optimization in Sec 2.2.1. Then, Sec presents relevant research that explores the incorporation of these methods into optimization processes. Sec offers an overview of optimization algorithms, while Sec delves deeper into the selected algorithm.

2.2.1 Structural optimization

Structural optimization aims to optimize the design of structures to achieve the desired structural performance and efficiency. This section discusses the application of computational techniques to find the optimal configuration, size, or shape of structural elements, considering various design objectives, constraints, and criteria. By optimizing the structural design, engineers can enhance structural strength, stiffness, stability, and durability, while also ensuring that the structure meets safety standards and functional requirements.

Generally, the main component of an optimization problem includes the objective function, which should be either maximized or minimized. The formation of the objective function is based on the input design variables. Constraints are the limitations or conditions that must be satisfied during the optimization process. These constraints can be related to design variables or limits on stress levels or displacements. To solve an optimization problem, an appropriate optimization algorithm is necessary. Throughout the optimization process, it is common to perform sensitivity analysis to understand the influence of each design variable on the objective function and constraints. Sensitivity analysis helps in identifying critical variables and provides insights into their impact on the optimization results.

The structural optimization problem can be divided into three distinct types: size, shape, and topology, based on the design freedom of the problem [17]. The choice of the design variables influences the final optimized results. However, the three categories of structural optimization techniques describe only the design problem and design space, and to solve the problem, an optimization algorithm is necessary.

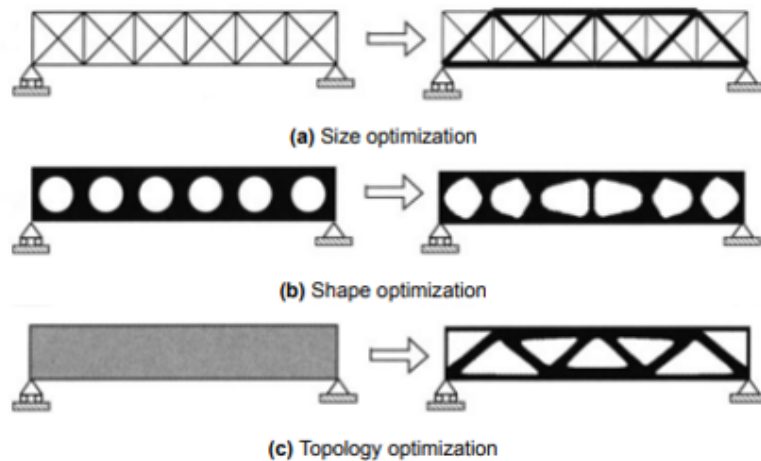


Figure 2.10: Three different structural optimization techniques, reprinted from [6]

The level of design freedom increases from (a) to (c) in Fig 2.10. In (a), the geometry of the structure is predetermined, with only the size of the members allowed to vary. (b) offers a bit more design freedom, although still quite constrained by the predefined structure. In (c), only a design space and boundary conditions are given, allowing for the creation of any form within these constraints during the optimization process. However, the advantage of greater design freedom comes with the drawback of an increased number of design variables, which often leads to longer computing times. Additionally, the results of topology optimization may require more post-processing due to less manufacturability in general.

2.2.1.1 Size optimization

Size optimization, where the design variables are restricted to the cross-sectional dimensions of the members, is the easiest and earliest approach to improving structural performance. The technique exhibits the lowest degree of design freedom, as only the sizes of the members are variables, and the overall geometry remains unchanged. The most common purpose of this type of optimization is to minimize material usage and thus the least cost. Since the structural members are usually manufactured in discrete sizes and shapes, necessitating the treatment of size variables as discrete entities during the optimization process [17].

The technique is particularly applied in spatial structures such as trusses, frames, and cable-strut systems [18] [19]. However, size optimization is commonly combined with the other two optimization techniques as a final step in multilevel optimization, which yields improved outcomes [20].

2.2.1.2 Shape optimization

The second type is shape optimization, also known as configuration optimization [17]. This type of optimization considers the continuous variation of geometric parameters, such as dimensions, angles, and

curves, to explore different design possibilities in the predefined domain boundaries, yet the topology remains fixed [21]. The objective of modifying the shape can be minimizing weight, maximizing stiffness, minimizing stress concentrations, or achieving a specific aerodynamic performance [22]. Shape optimization finds applications in various structural systems, including beams, trusses, shells, and complex three-dimensional structures.

The general setup of shape optimization consists of three components: 1.) A way of describing geometry. 2.) Structural analysis. 3.) Optimization algorithm [23]. The first step of conducting shape optimization is to define design variables to represent the boundary of the structural shape. This step is crucial because if the design variables are not carefully selected, the accuracy of the FEA model for structural analysis can deteriorate during optimization, rendering the results useless. This issue commonly arises when using the coordinates of boundary nodes as design variables, as seen in early shape optimization studies [24]. A visual representation in Fig 2.11 demonstrates this problem, where the finite element model is suitable for the initial design but clearly not accurate for the final design. To address the challenge, it is essential to avoid a direct correspondence between the FEA model and the design variables, ensuring an adequate number of elements for accurate structural analysis [25].

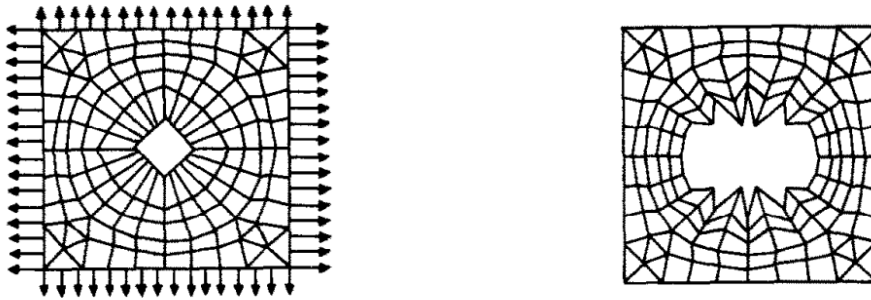


Figure 2.11: Independent node movement of a hole in a plate. Left: initial design, Right: final design, reprinted from [7]

The three most used ways to represent the boundary shape of the structural elements are addressed below:

1. Polynomial Representation of Boundaries:

Polynomials have been commonly employed to describe boundaries in shape optimization, with polynomial coefficients as design variables [25]. After [26] used this technique, many studies have followed this approach. A more comprehensive method involves defining the boundary as a linear combination of shape functions, where the coefficients serve as design variables [27].

2. Spline representation of boundaries:

Spline representation of boundaries is a modified technique to avoid oscillations in boundary shape resulting from high-order polynomials. The spline function consists of low-order polynomial pieces, ensuring smoothness. For example, the cubic spline function, known for its continuity and minimum mean curvature, is often favored [28]. Other approaches, like using Bezier and B-spline blending functions, have been explored by Braibant et al [29]. The approach offers flexibility and automatic consideration of boundary regularity requirements.

3. The Design Element Concept:

To enhance the accuracy of the FEA model for structural analysis, the design element concept, introduced by Imam [30], has been employed. This approach divides the structure into distinct regions or design elements, controlled by a set of key nodes that determine the geometry. Each design element corresponds to a group of finite elements and is associated with a specific set of design variables that determine the movement of key nodes during optimization. Isoparametric finite element interpolation functions are commonly used to describe the boundaries of design elements in two-dimensional space [25].

After selecting the design variables, they can formulate the below structural optimization problem by defining the objective function:

$$\begin{aligned}
 & \text{minimize} && f(x) \\
 & \text{subject to} && g_e(x) \leq 0 \\
 & && g_i(x) \leq 0
 \end{aligned} \tag{2.20}$$

Eq 2.20 [23] is the general mathematical representation of the optimization problem, where $f(x)$ represents the objective function to be minimized. The formulas involve minimizing the objective function while satisfying a set of constraints $g_e(x) \leq 0$ and $g_i(x) \leq 0$. The former one is an explicit constraint, which can be directly expressed in terms of the design variables, such as upper and lower bounds, while the latter one is an implicit constraint, which often pertains to structural responses, such as stress, displacement, and natural frequency, and require a more complex evaluation to ensure they are satisfied. The objective is to find the optimal values of the vector design variables x that lead to the minimum value of the objective function while satisfying the given constraints.

After the initial geometrical model is built, the design model will be converted into a structural analysis model to evaluate the structural performance of the model (implicit constraints). The results of the analysis then provide the information for the optimization algorithm to find a new set of design variables. The iteration terminates when the specified design criteria are satisfied. There are numerous

optimization algorithms available. These are broadly divided into two types: gradient-based optimization techniques and gradient-free optimization algorithms. Gradient-based algorithms, such as the commonly used gradient descent method, steer the search toward the optimum by calculating derivatives of the objective function. Gradient-free algorithms, on the other hand, such as genetic algorithms or particle swarm optimization, do not rely on derivatives and instead explore the search space through repetitive iterations and evaluations of the objective function.

2.2.1.3 Topology optimization

The last optimization type is topology optimization. The numerical optimization methods proposed by Bendsøe and Kikuchi [31] is a systematic approach to exploring the most efficient and lightweight configurations for structural components. Most of the methods are based on finite element analysis (FEA) where the design domain is discretized into a fine mesh of elements [8]. The fundamental concept behind topology optimization is to represent the design domain as a grid or mesh of discrete elements, where each element can either be active (filled with material) or inactive (void). By assigning design variables to each element, which define its activity status, the optimization process seeks to find the optimal distribution of active and inactive elements that minimizes a predefined objective function while satisfying certain constraints. It allows the most freedom as the shape of a structure is significantly less influenced by the input of the designer. Topology optimization inherently deals with discrete choices in terms of elements' presence or absence, and it aims to determine the optimal layout or distribution of structural components [17].

The objective function can be defined based on various performance criteria such as minimizing structural compliance, maximizing stiffness, or minimizing material usage. Constraints can be imposed to ensure structural stability, limit stress levels, or satisfy other design requirements. The optimization algorithm iteratively updates the design variables, evaluating the objective function and constraints at each iteration, until a satisfactory optimal solution is reached.

Topology optimization allows for the exploration of innovative and unconventional structural designs, often resulting in complex and organic shapes that are highly efficient in terms of material usage and structural performance, yet are mostly hard to manufacture and need post-processing. Nevertheless, it provides insights into the fundamental behavior and load paths within a structure, leading to improved designs that can be further refined and optimized through subsequent engineering processes. Topology optimization has gained huge attention in recent years, accordingly, several numerical methods have advanced to the point of practical implementation, notably the Solid Isotropic Material with Penalization (SIMP) method and the Evolutionary Structural Optimization (ESO) method. The SIMP method was originally introduced by Bendsøe in 1989 [32]. It involves penalizing intermediate densities to achieve

optimal material distribution. On the other hand, the ESO method gradually eliminates inefficient material from a structure. These methods have proven effective in optimizing the topology of structures and have found practical applications in various fields. The methods are elaborated below:

1. Evolutionary Structural Optimization (ESO):

The ESO method, first proposed by Xie and Steven in the early 1990s [33], is a powerful numerical method used to optimize the topology of structures. The fundamental concept behind ESO is the gradual removal of inefficient material from a structure to improve its overall structural performance. By iteratively eliminating elements or regions with low stress or strain energy, ESO aims to achieve an optimal distribution of material within the given design domain. This method utilizes evolutionary algorithms or optimization techniques to evolve the structure and find the most efficient configuration and topology.

Determining the stress distribution of a structure with FEA is a crucial step during the evolutionary procedure when ESO is dealing with stress level problem. Low-stress values in certain areas indicate inefficiency, while a well-designed structure should ideally have stress levels close to a safe and uniform level. To address this, a rejection criterion based on local stress levels is employed, where material underutilized is progressively removed. The stress level of each element is evaluated by for example comparing its von Mises stress (σ_e^{vm}) with the maximum von Mises stress of the entire structure (σ_{max}^{vm}). RR_i in Eq 2.21 is the current rejection ration [8].

$$\frac{\sigma_e^{vm}}{\sigma_{max}^{vm}} < RR_i \quad (2.21)$$

The process of conducting FEA and element removal is iteratively repeated with the same rejection ratio RR_i until a steady state is achieved. In the steady state, no more elements are deleted based on the current rejection ratio. ER (evolutionary rate) is then added to the rejection ratio, resulting in an updated rejection ratio: $RR_{i+1} = RR_i + ER$. The iteration process is started again with the increased rejection ratio until a new steady state is reached. The evolutionary process stops when the optimum is reached.

On the other hand, the ESO method can be also used to optimize a structure based on stiffness or displacement, which means the mean compliance C , the inverse of the overall stiffness, is minimized. The mean compliance is defined as the total strain energy or external work done by applied loads, expressed as:

$$C = \frac{1}{2} \mathbf{f}^T \mathbf{u} \quad (2.22)$$

The stiffness matrix of the structure changes when the element is removed, thus the mean compliance also varies:

$$\Delta C = \frac{1}{2} \mathbf{u}_i^T \mathbf{K}_i \mathbf{u}_i \quad (2.23)$$

where : u_i = displacement vector of the i th element

From Eq 2.23, the sensitivity number for the mean compliance can be defined as:

$$\alpha_i^e = \frac{1}{2} \mathbf{u}_i^T \mathbf{K}_i \mathbf{u}_i \quad (2.24)$$

According to the expression of α_i^e , the increased mean compliance results from the elimination of the i th element is equal to its elemental strain energy. Obviously, the most efficient way of minimizing C is to remove the items with the lowest α_i . The element removal ratio (ERR) determines the number of elements to be removed, which is the ratio of the number of elements removed at each iteration to the total number of elements in the initial structural model [34].

The ESO method facilitates structural optimization by deactivating inefficient material based on stress or strain energy levels. It is simple to use and comprehend, with no sophisticated mathematical programming approaches. ESO is also applicable to 2D and 3D situations. However, since the ESO method cannot restore eliminated material, material discarded early in the process may be necessary later for an optimal design. As a result, while ESO improves initial ideas in general, it may not always achieve the absolute optimum. The ESO algorithm is heuristic in nature and lacks theoretical rigor. Early ESO research ignored critical numerical concerns in topology optimization, such as checkerboard patterns, mesh dependency, and local optima problems. To solve these shortcomings, an improved algorithm known as bi-directional evolutionary structural optimization (BESO) has been developed.

2. Bi-directional Evolutionary Structural Optimization (BESO):

The BESO method is a variation of the ESO method that allows for both the addition and removal of material during the optimization process, initially proposed by y Yang et al [35]. BESO combines the advantages of ESO with the flexibility of modifying the structure by adding new material. This bi-directional approach enables the exploration of a larger design space, leading to improved solutions. By iteratively modifying the structural topology based on predefined design criteria, BESO seeks to achieve an optimal balance between material reduction and structural performance. The addition and removal

of material are guided by sensitivity analysis, allowing for efficient and effective optimization of complex structures.

BESO estimates the sensitivity numbers of void elements through linear extrapolation of displacement fields obtained from FEA. Elements with the lowest sensitivity numbers are removed, while void elements with the highest sensitivity numbers are converted into solid elements [35]. The numbers of removed and added elements are determined separately using the rejection ratio (RR) and inclusion ratio (IR) parameters. However, this approach of removing and adding separately requires a careful selection of RR and IR values to get a reasonable result [36].

Huang and Xie [8] developed a BESO algorithm for stiffness optimization that addresses the procedure and various challenges needed to be solved in topology optimization, including defining the optimization problem, dealing with checkerboard patterns, handling mesh-dependency, and achieving solution convergence.

Topology optimization aims to minimize the mean compliance (C), which is the same as maximizing the stiffness, subject to a given constrained volume. The problem is formulated as follows:

$$\begin{aligned}
 \text{minimize} \quad & C = \frac{1}{2} \mathbf{f}^T \mathbf{u} \\
 \text{subject to} \quad & V^* - \sum_{i=1}^N V_i x_i = 0 \\
 & x_i = 0 \quad \text{or} \quad 1
 \end{aligned} \tag{2.25}$$

\mathbf{f} and \mathbf{u} are the applied external force and displacement vectors, respectively. V_i represents the volume of an individual element, V^* is the prescribed total volume, N is the total number of elements, and x_i is the binary design variable indicating the presence (1) or absence (0) of an element.

The BESO method calculates the sensitivity numbers (α_i^e) for each element based on the change in mean compliance (ΔC_i) resulting from the removal of the element. The sensitivity number is defined as:

$$\alpha_i^e = \Delta C_i = \frac{1}{2} \mathbf{u}_i^T \mathbf{K}_i \mathbf{u}_i \tag{2.26}$$

where u_i is the nodal displacement vector of the i th element and K_i is the elemental stiffness matrix.

Two problems, checkerboard and mesh-dependency, occur with the above definition of sensitivity number. The existence of a checkerboard pattern poses challenges in both interpreting and manufacturing the optimal structure, see Fig 2.12. Mesh dependency refers to the issue of obtaining varying topologies when different sizes of finite element meshes are employed. Ideally, finer mesh should result in the same optimal structure but improved boundary representation, rather than producing a more intricate

or qualitatively different structure [37].

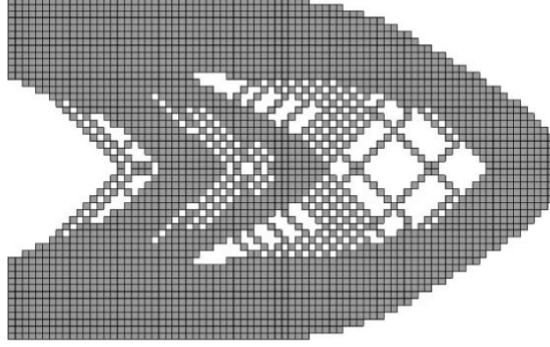


Figure 2.12: A typical checkerboard pattern in the ESO method, reprinted from [8]

To avoid the above problems, a filtering and smoothing scheme is implemented. The nodal sensitivity numbers (α_j^n) are initially calculated by averaging the elemental sensitivity numbers connected to each node. This is achieved by assigning weight factors (w_i) to the elemental sensitivity numbers based on their distances from the node (r_{ij}). Closer elements have a greater influence on the nodal sensitivity number.

$$\alpha_j^n = \sum_{i=1}^M w_i \alpha_i^e \quad (2.27)$$

$$w_i = \frac{1}{M-1} \left(1 - \frac{r_{ij}}{\sum_{i=1}^M r_{ij}} \right) \quad (2.28)$$

Where w_i is the weight factor of the i th element, r_{ij} is the distance between the center of the i th element and the j th node, and M is the total number of elements connected to the j th node.

The filtered nodal sensitivity numbers are then used to compute smoothed elemental sensitivity numbers (α_i). This process involves projecting the nodal sensitivity numbers onto the design domain using a filtering scheme. The filter has a fixed length scale parameter r_{min} , which remains unchanged regardless of mesh refinement. This scale parameter helps determine the nodes that significantly impact the sensitivity of each element. By drawing a circle centered at the centroid of each element with a radius of r_{min} , a circular sub-domain is formed. Nodes within this sub-domain contribute to the calculation of the improved sensitivity number (α_i) for the element.

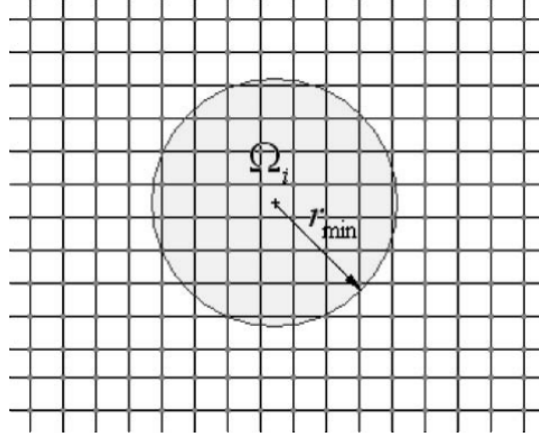


Figure 2.13: Nodes located within the circular sub-domain Ω_i are used in the filter scheme for the i th element, reprinted from [8]

$$\alpha_i = \frac{\sum_{j=1}^K w r_{ij} \alpha_j^n}{\sum_{j=1}^K w r_{ij}} \quad (2.29)$$

$$w(r_{ij}) = r_{min} - r_{ij}, \quad j=1, 2, 3 \dots K \quad (2.30)$$

The filter scheme effectively smooths the sensitivity numbers throughout the entire design domain, including the void elements. The void elements may exhibit high sensitivity numbers due to the presence of nearby solid elements within the sub-domain. Consequently, some void elements may be converted into solid elements in subsequent iterations.

To ensure convergence of the objective function during the evolutionary process, a simple averaging scheme is employed. Huang and Xie [38] discovered that averaging the sensitivity number with its historical information effectively addresses this issue.

$$\alpha_i = \frac{\alpha_i^K + \alpha_i^k - 1}{2} \quad (2.31)$$

In this scheme, the sensitivity number α_i at the current iteration k is computed by averaging the sensitivity numbers from the current and previous iterations. The updated sensitivity number is then used for the next iteration, thereby incorporating the complete history of sensitivity information from previous iterations.

Before each new iteration, a target volume for the next step V_{k+1} needs to be determined. The volume evolution follows a formula:

$$V_{k+1} = V_k(1 + -ER), \quad k=1, 2, 3... \quad (2.32)$$

where ER represents the evolutionary volume ratio. Once the volume reaches its constraint, $V_{k+1} = V^*$ remains unchanged for the remaining iterations.

Next, elements with a sensitivity number below a threshold value $\alpha_{del}^t h$ are removed, while void elements with a sensitivity number exceeding $\alpha_{add}^t h$ are added. It is important to note that $\alpha_{del}^t h$ is always less than or equal to $\alpha_{add}^t h$. The exact values of both thresholds can be determined through the following steps:

1. Start with $\alpha_{add}^t h = \alpha_{del}^t h = \alpha_{th}$. Here, α_{th} can be determined based on V_{k+1} .
2. Calculate AR, the volume addition ratio, which is the number of added elements divided by the total number of elements in the design domain. If AR exceeds the maximum volume ratio ARmax, $\alpha_{del}^t h$ and $\alpha_{add}^t h$ need to be recalculated in the next step. If AR is smaller than ARmax, skip step 3.
3. Compute $\alpha_{add}^t h$ by sorting the sensitivity numbers of void elements = 0. The number of elements that will become solid is equal to ARmax multiplied by the total number of elements in the design domain. The sensitivity number of the element ranked just below the last added element becomes the new $\alpha_{add}^t h$. The value of $\alpha_{del}^t h$ should be chosen in a way that ensures the removed volume equals $(V_k - V_{k+1} + V_{addedelements})$.

The iterations, including finite element analysis and element removal/addition, stop when both the volume constraint and the convergence criterion are satisfied. The convergence criterion is expressed as an error condition:

$$\text{error} = \frac{\left| \sum_{i=1}^N C_{k-i+1} - \sum_{i=1}^N C_{k-N-i+1} \right|}{\sum_{i=1}^N C_{k-i+1}} \leq \tau \quad (2.33)$$

Here, k represents the current iteration number, τ is the allowable convergence tolerance, and N is an integer determining the length of the last considered iterations [8].

In summary, the BESO method for stiffness optimization addresses various challenges in topology optimization and involves iterative element removal and addition based on sensitivity numbers, incorporating smoothing algorithms, filtering schemes, and convergence criteria.

3. Solid Isotropic Material with Penalization (SIMP):

The SIMP technique is another common topology optimization method that assumes each element is made of an isotropic material with variable densities. It penalizes intermediate densities in order to

achieve optimal material distribution within a specific design domain. Intermediate densities are penalized by including an interpolation scheme in the optimization formulation, encouraging the selection of materials with either extremely low or very high densities, ranging from void (near-zero density) to solid (full density). The SIMP method has been shown to be useful in a variety of engineering applications and has had a considerable impact on the field of topology optimization [8].

The problem formulation [8]:

$$\begin{aligned}
 & \text{minimize} && c = \mathbf{f}^T \mathbf{u} \\
 & \text{subject to} && V^* - \sum_{i=1}^N V_i x_i = 0 \\
 & && 0 < x_{min} \leq x_i \leq 1
 \end{aligned} \tag{2.34}$$

The compliance c denoted here is twice the mean compliance C in Eq 2.25, defined in the BESO section. In contrast to BESO, which uses either of the two discrete bound values, the SIMP method allows the design variable x_i to vary continuously from x_{min} to 1. The global stiffness matrix can be written as a function of the design variables while taking the material interpolation technique into account:

$$\mathbf{K} = \sum_i x_i^p \mathbf{K}_i^0 \tag{2.35}$$

The sensitivity of the objective function c is can then be expressed as:

$$\frac{\partial c}{\partial x_i} = -p x_i^{p-1} \mathbf{u}_i^T \mathbf{K}_i^0 \mathbf{u}_i \tag{2.36}$$

To solve the defined optimization problem, several different optimization algorithms can be employed, like Optimality Criteria (OC) methods [39], the Method of Moving Asymptotes (MMA) [40], and so on.

As mentioned above, to avoid checkerboard patterns and mesh dependency issues, a filter scheme for improving elemental sensitivities introduced by Sigmund [41] is utilized:

$$\frac{\partial c}{\partial x_i} = \frac{1}{x_i \sum_{j=1}^N H_{ij}} \sum_{j=1}^N H_{ij} x_j \frac{\partial c}{\partial x_j} \tag{2.37}$$

where : N = total number of elements in the mesh

$$H_{ij} = r_{\min} - r_{ij}, \quad \{i \in N \mid r_{ij} \leq r_{\min}\} \quad (2.38)$$

In Eq 2.37 and Eq 2.38, H_{ij} is the mesh-independent weight factor, which becomes zero when outside the circular filter area, see Fig 2.13. r_{ij} is the distance between the centers of elements i and j .

By introducing material penalization in Eq 2.35, the initial optimization problem, Eq 2.34 becomes nonconvex, which can lead to local optima with grey regions. The continuation method, suggested by Rozvany et al [42], has been proposed and proved to mitigate this issue. In this way, the penalty exponent is progressively increased in small steps in subsequent cycles, which can help avoid local optima and converge closer to the global optimum.

2.2.2 Effect of self-weight on topology optimization

As explained in Sec 2.2.1.3, the general problem statement of topology optimization is to minimize compliance with specified external loads, respecting the volume constrained. However, when density-dependent body forces, such as self-weight, are included, many numerical issues arise that necessitate specific handling. The most challenging problems consist of non-monotonous behavior of the compliance, the possible unconstrained character of the optimum, and the parasitic effect for low densities when using the SIMP method [43].

Huang and Xie [9] developed an advanced BESO method employing SIMP material model, soft-kill and hard-kill BESO, where the material stiffness is penalized using a power-law relationship as:

$$E(x_i) = E^0 x_i^p \quad (2.39)$$

where : E^0 = Young's modulus for solid material

p = penalty exponent

In the soft-kill approach, a large penalty exponent p is used ($p \geq 3$), and void elements are represented as soft material, done by reducing the thickness of inefficient material. On the other hand, in the hard-kill approach, the penalty exponent is infinity, resulting in zero stiffness for void elements.

To overcome the non-monotonous behavior of the compliance when including self-weight, the sensitivity of the mean compliance C should be able to change sign when adjusting the value of the design variable. Accordingly, the sensitivity might be either positive or negative to behave non-monotonous. To do this.

a vector of Lagrangian multiplier $\lambda = \frac{1}{2}\mathbf{u}$ is added to Eq 2.25:

$$C = \frac{1}{2}\mathbf{f}^T\mathbf{u} + \lambda^T(\mathbf{f} - \mathbf{K}\mathbf{u}) \quad (2.40)$$

The sensitivity of the objective function that has the ability to be either negative or positive can then be repressed as:

$$\frac{dC}{dx_i} = \frac{\partial\mathbf{f}^T}{\partial x_i}\mathbf{u} - \frac{1}{2}\mathbf{u}^T\frac{\partial\mathbf{K}}{\partial x_i}\mathbf{u} \quad (2.41)$$

However, the above expression of sensitivity encounters problems in the low-density regions when using power-law material interpolation. Accordingly, a different interpolation scheme presented by Stolpe and Svanberg [44] is adopted. The density ρ_i and Young's modulus of the material E_i becomes:

$$\rho_i = x_i\rho^0 \quad (2.42)$$

$$E_i = \frac{x_i}{1 + q(1 - x_i)}E^0 \quad (2.43)$$

q is a new variable of the penalty factor and is larger than 0, which directly influences the non-monotonous the behavior of the objective function. For the soft-kill BESO method, a large penalty factor q is preferred to ensure convergence to a stable design. As for the hard-kill BESO method, q approaches infinity, and Young's modulus of soft elements becomes zero. A higher penalty factor q leads to weaker non-monotonous behavior. When the penalty factor is infinite, the non-monotonous behavior completely disappears. Consequently, the hard-kill BESO method may yield different solutions compared to the soft-kill BESO method. Despite this, the hard-kill BESO method offers higher computational efficiency, making it worth exploring for certain applications.

Several examples are presented in the paper [9] to prove the effectiveness of the proposed method for the topology optimization including self-weight, and also the comparison between the soft-kill and the hard-kill method.

Example 1

In the first example, a rectangular plate measuring 1 m x 0.5 m is pinned at both bottom ends. The goal is to determine the optimal structure topology considering only its self-weight. The target amount of available material after the optimization is limited to 15% of the design domain. The material properties

assumption: Young's modulus of 200 GPa, Poisson's ratio of 0.3, and a density of 78 kg/m^3 . To exploit symmetry, only half of the design domain is analyzed using a mesh of 100×50 four-node plane stress elements. After the evolutionary process, the symmetric half region is mirrored to visualize the entire structure. Both the soft-kill and hard-kill BESO methods are employed in this example. The parameters for the soft-kill BESO include $ER = 3\%$, $AR_{max} = 2\%$, $q = 5$, and $r_{min} = 30 \text{ mm}$. The settings for the hard-kill BESO are the same as those for the soft-kill BESO except for q is infinite.

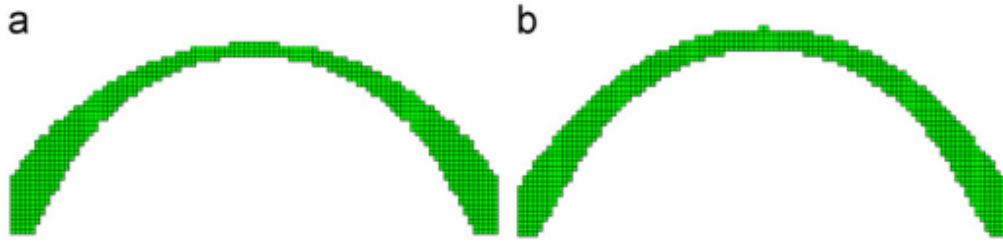


Figure 2.14: (a) the soft-kill BESO method with $q=5$ (b) the hard-kill BESO method with $q=\infty$, reprinted from [9]

Both the soft-kill and hard-kill BESO methods give an arch-shaped structure that spans both end supports to effectively carry its self-weight. Only a slight difference in the optimal shapes because of different penalty factors q .

Example 2

The second example aims to optimize the classic MBB beam under a concentrated load F applied at the mid-span of the beam and its self-weight. The support condition is the same as in the previous example. Making use of symmetry, only half of the design domain meshes using 100×50 four-node plane stress elements. The target volume ratio is set to 40% of the entire design domain. Young's modulus $E = 200 \text{ GPa}$, Poisson's ratio $\nu = 0.3$, and density $\rho = 78 \text{ kg/m}^3$. Consequently, the expected total weight of the final design is 3120 kg. The BESO method utilizes the following parameters: $ER = 2\%$, $AR_{max} = 2\%$, $q = 5$, and $r_{min} = 0.3 \text{ m}$.

Fig 2.15 shows the results with the use of the soft kill method when considering different ratios between external loads and self-weight. Bruyneel and Duysinx [45] draw the same conclusion that the optimal topology varies depending on the ratio between the external force and self-weight. As F decreases, the materials between the loading point and supports are removed accordingly.

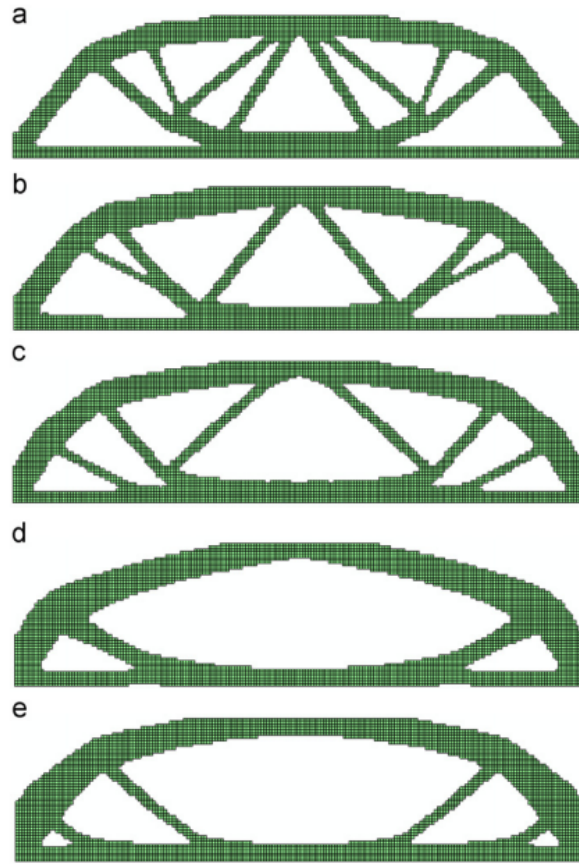


Figure 2.15: (a) zero self-weight (b) $F=100\%$ self-weight (c) $F=50\%$ self-weight (d) $F=10\%$ self-weight (e) self-weight only, reprinted from [9]

The hard-kill BESO method is also tested with self-weight only in this non-monotonous problem, using the same parameters as the soft-kill, except for $q=\infty$. The result shown in Fig 2.16 is similar to that achieved with the soft-kill BESO method in Fig 2.15 (e). The mean compliance of the hard-kill design is 0.037 N m, while in the soft-kill design, it's 0.034 N m. This implies that the soft-kill BESO method yields a somewhat better solution than the hard-kill BESO method, yet the hard-kill solution can still be considered an approximation optimal design.

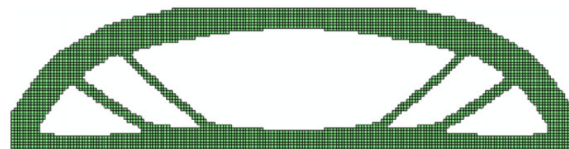


Figure 2.16: optimal topology with self-weight, hard-kill method, reprinted from [9]

2.2.3 Optimization in Grasshopper

Grasshopper is a Rhinoceros 3D visual programming language and environment that allows for parametric design and computational modeling. Grasshopper's parametric design capabilities, which allow for the

production of flexible and adaptable models by defining relationships between design parameters, is one of its key features, making it perfect for iterative and exploratory design processes.

Grasshopper can also work in collaboration with powerful Finite Element Analysis plugins to do structural analysis. This enables designers to analyze and optimize their designs' performance and behavior under various load scenarios. It may simulate structural behavior such as stress distribution, deflections, and natural frequencies.

Grasshopper also includes a variety of optimization algorithm plugins that can be used to improve the design process. These plugins offer a variety of optimization algorithms, including evolutionary algorithms, genetic algorithms, particle swarm optimization, and others. These algorithms allow designers to search for the best design solution based on predefined objectives and limitations.

Designers can develop an integrated and seamless workflow for parametric design exploration, structural analysis, and optimization by combining Grasshopper's parametric design capabilities, structural analysis tools, and optimization algorithm plugins.

2.2.3.1 Opossum

Opossum is an optimization plugin developed for Grasshopper. It is a model-based optimization tool specifically designed for architectural practice. According to Wortmann and Nannicini [46], model (or surrogate)-based optimization strategies obtain satisfactory outcomes with a small number of simulations, which means it reaches convergence faster.

Global black-box optimization

Unlike simulation-based optimization, which evaluates parametric models with numerical simulation to find the relationship between variables and performance goals, Global black-box optimization methods, also known as derivative-free methods, do not require a mathematical formulation. These methods offer a balance between exploring the entire design space and focusing on promising regions to find the best solution. (1) Direct search, (2) model-based methods, and (3) metaheuristics are the three categories of Black-box methods for optimization. The first two types switch between local and global search, while the third one limits an initially global search to an increasingly local one as the optimization process develops.

Opossum employs two different best-performing, single-objective optimization algorithms: model-based Radial Basis Function Optimization (RBFOpt) and evolutionary Covariance Matrix Adaptation Evolution Strategy (CMA-ES) [47].

1. RBFOpt: A global optimization algorithm based on radial basis function interpolation. It constructs a response surface using a set of sample points and approximates the objective function based on this

surface. RBFOpt iteratively selects new sample points to improve the interpolation and search for the global optimum. It is suitable for problems with a moderate number of design variables and a smooth objective function.

2. CMA-ES: For complex optimization problems in continuous search spaces, such as non-convex, ill-conditioned, multi-modal, rough, or noisy, CMA-ES is a stochastic derivative-free numerical optimization algorithm. It operates by sampling a normal distribution to generate candidate solutions. With each iteration, the mean and variance of the distribution are updated based on the outcomes of the population, gradually converging towards a global maximum.

Opossum GUI

Opossum's GUI includes three tabs that provide increasing levels of control, see Fig 2.17. (1) The first tab can choose between minimization or maximization of the objective function, select one of three pre-sets of parameters: 'RBFOpt (fast and good)', 'CMA-ES (slow but steady)', and 'CMA-ES from start point', and start the optimization process. The first tab additionally shows an animated convergence graph to keep viewers updated on the optimization's progress. (2) The second tab allows users to establish halting criteria depending on the number of iterations or the amount of time spent, as well as to report the optimization runs. (3) The third tab receives RBFOpt command line options. When enabled, this "expert" window offers the user complete control, with settings input here overriding those specified by the first two tabs. Opossum mimics the appearance and function of existing optimization tools, including color schemes for optimization components and their relationships to variables and goal values. Double-clicking on an optimization component launches a window with a GUI specific to that tool, which includes the three tabs mentioned above for Opossum. Thus, Opossum delivers a difficult and unique optimization package in an easy-to-use format.

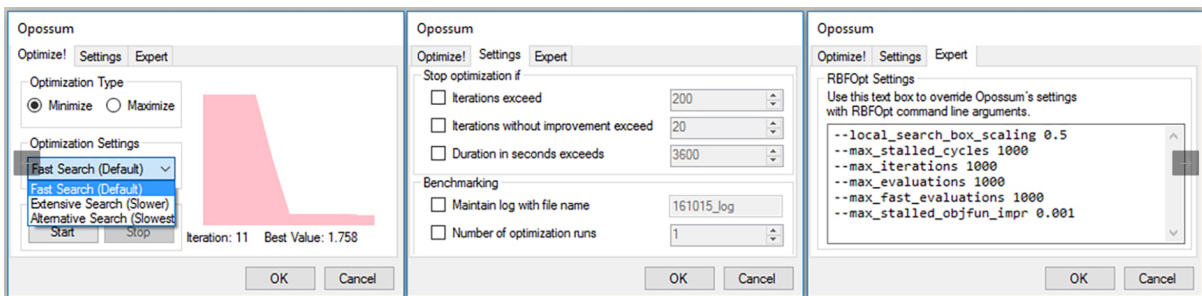


Figure 2.17: Opossum GUI, reprinted from food4Rhino-Opossum

Evaluation

Abdul [48] compares Opossum with another optimization plugin for Grasshopper, GA and SA from Galapagos, and concluded that RBFOpt and CMA-ES are the most robust algorithms in this benchmark. CMA-ES was the best-performing and most convergent algorithm for evaluating large functions.

Thomas [47] compared the performance of RBFOpt with five other solvers available in Grasshopper: the GA and SA in Galapagos, the PSO of Silvereye, the DIRECT algorithm in Goat, and HypE in Octopus. The results depict that DIRECT is the worst-performing solver and exhibits minimal improvement during the optimization process. This is because its recursive subdivision in the dimensions corresponding to the variables is too slow. The remaining metaheuristics, including the Pareto-based HypE, have similar performance. Opossum's RBFOpt is proven to be the best-performing solver. Take note of RBFOpt's quick progress in a few iterations. In conclusion, DIRECT is fully deterministic. RBFOpt experienced the most stable convergence, while the single-objective metaheuristics exhibited wider, less stable ranges.

2.2.3.2 Karamba3D: Topology optimization

Karamba3D is a structural analysis plugin making use of FEM for Grasshopper. It stands out among other Finite Element commercial programs due to its unique advantages: It is designed to be user-friendly, making it accessible even to non-experts. Specifically tailored for architects and engineers during the early design phase, Karamba3D offers an interactive experience [49].

A key feature of Karamba3D is its seamless integration with Grasshopper. This integration allows for an easy combination of parameterized geometric models, FEA, and optimization algorithms such as Opossum or Galapagos. This integration enhances the capabilities of Karamba3D, enabling efficient and flexible design exploration and optimization.

BESO for Shells

The background knowledge and logic behind 'BESO for Shells' has been described in Sec 2.2.1.3.

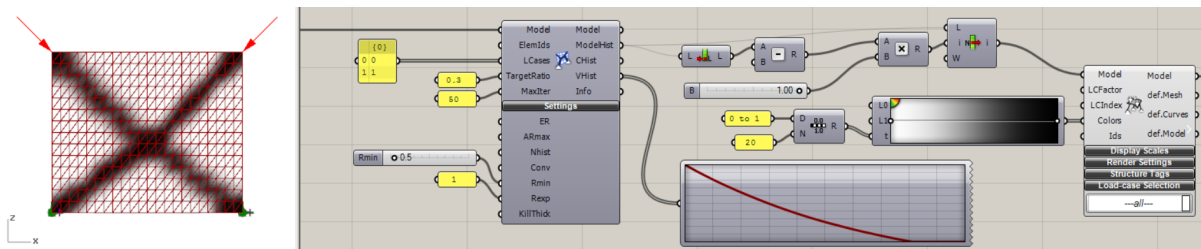


Figure 2.18: BESO for a rectangular plate under two corner loads, reprinted from Karamba3D 1.3.3

The main input to "BESO for Shells" includes: Model / ElemIds / LCases / TargetRatio / MaxIter. Important to note, ElemIds takes identifiers of the shell mesh that participates in the optimization, which can exclude the mesh in non-design space. TargetRatio is the ratio between the final mass, only taking into account the active elements, to the initial mass.

More advanced options under the submenu "Settings" allow the user to further control the optimization procedure. The mathematical meaning of each option is described in Sec 2.2.1.3: ER / ARmax / Nhist / Conv / Rmin / Rexp / KillThck. ER is the evolutionary ratio that specified the relation between the

volume in two consecutive iteration steps, see Eq 2.32. ARmax means the proportion of the maximum number of elements that can be added per step. Nhist is the number of iterations that happened before achieving the convergence. Conv is the change of mass between two cycles. As mentioned before, to prevent the occurrence of checkerboard patterns, a filtering scheme is implemented in the BESO algorithm to evaluate the fitness of individual elements. Rmin is used to determine the sensitivity of the element by defining the radius of the influence, see Fig 2.13. On the other hand, Rexp plays a role in weighting the strain energy at nodes when calculating the sensitivity of an element. It determines the distance within which the nodes are considered and influences the weight assigned to each node. The weight is determined in Eq 2.44, with $R_{ij} = Rmin - R$. R is the distance between a sample node and the center of the element, while $\sum R_{ij}$ is the sum of the distances from the center of the element to all nodes that are closer than Rmin. KiillThick is the thickness of the soft element, which is a necessary value for the BESO soft-kill method addressed in Sec 2.2.2.

$$w = \left(\frac{R_{ij}}{\sum R_{ij}} \right)^{R_{exp}} \quad (2.44)$$

The output of "BESO for Shells" includes the data of: Model / ModelHist / CHist / VHist / Info. ModelHist, CHist, and VHist provide information on the intermediate result, including the history of volume-weighted compliance and the volume of the structure.

Different Grasshopper Plugins for Topology Optimization

Apart from Karamba3D: BESO for Shells, there are several other plugins for topology optimization using different methods available in the Grasshopper environment. For example, Millipede, TopOpt, and tOpos use SIMP while Ameba uses BESO. Mariam and Zeynep [50] utilized a box as a case study in order to compare the three plugins: Millipede, tOpos, and Ameba. The potential and efficiency of the three plugins are addressed from an architectural approach. In conclusion, Ameba gives the noisiest optimized geometry and tOpos produces the most realistic result. Considering computing speed, tOpos utilizing GPU first reached convergence, while Ameba spent reasonable time, and they both eventually achieved the desired volume fraction. On the other hand, Millipede is the least effective and took the most time, yet did not achieve the desired volume fraction.

Though tOpos has been proven to be the most powerful topology optimization plugin in the paper, its ability to include self-weight in the optimization process is lacking. Nevertheless, the dimension of tOpos is only in three dimensions, and it was unable to generate shell shape geometry from a box design domain to carry its self-weight eventually. In comparison, Karamba3D has a super intuitive "Loads"-component that is able to simulate the effect of gravity load in optimization iterations.

Chapter 3

Analytical Derivation and Numerical Integration

According to S. Timoshenko [4], the form of equal strength has a design criterion of constant stress in all the cross-sections as explained in Section 2.1. The proposed mathematical model presented below is based on the assumption that the structure is inextensible, and the material is homogeneous. These are the common assumptions utilized in the previous works for structural optimization [1] [10] [3]. The aim of the analytical form finding is to derive the math solutions of the constant stress geometry under different load cases.

The research involves three analytical form-finding practices: two load cases and one load combination. Each derivation initiates by establishing equilibrium according to the predefined criteria. Subsequently, the obtained mathematical solutions are validated by Finite Element Analysis (FEA) tool Karamba, aligning with the constant stress criterion.

3.1 Form of constant stress: self-weight

The first load case to be explored is self-weight. Firstly, the analytical expression of the cross-sectional area is derived. Secondly, the geometrical model is built in Grasshopper and validated by Karamba.

3.1.1 Analytical derivation: self-weight

In order to obtain the equations that satisfy the uniform strength criterion, we must first examine an infinitesimal segment of the member, see Fig 3.1.

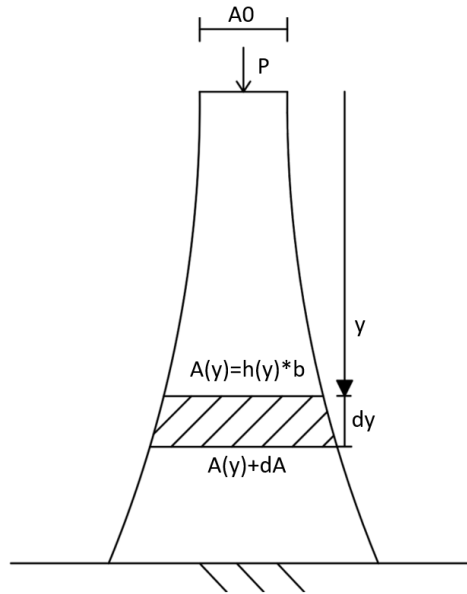


Figure 3.1: Infinitesimal segment of the member

$A(y)$ represents the cross-sectional area at any arbitrary position y , while $h(y)$ denotes the depth of the cross-section at y . b stands for the unit width of the cross-section, oriented perpendicular to the plane of the paper.

As the compressive stress in both the upper and lower cross-sections of the infinitesimal segment must remain constant, the incremental increase in the cross-sectional area, denoted as dA , is intended to compensate for the added weight of the segment, represented on the left-hand side of Equation 3.1. Accordingly,

$$\gamma \cdot A(y) \cdot dy = dA \cdot \sigma \quad (3.1)$$

where : $\sigma = \text{constant stress}$

$\gamma = \text{specific weight}$

Dividing Equ 3.1 by $A\sigma$ and integrating both sides, gives the following equations:

$$\int \frac{\gamma}{\sigma} dy = \int \frac{1}{A} dA$$

$$\frac{\gamma y}{\sigma} + c_1 = \ln A$$

$$A = e^{\frac{\gamma y}{\sigma} + c_1} = C e^{\frac{\gamma y}{\sigma}}, \text{ with } C = e^{c_1} \quad (3.2)$$

$$A(y = 0) = C = A_0 \quad (3.3)$$

$$A(y) = A_0 e^{\frac{\gamma y}{\sigma}} \quad (3.4)$$

At $y = 0$, the area is A_0 , and Equ 3.4 gives the relation between $A(y)$ and A_0 . To avoid A_0 as 0 because there is no self-weight on top of it, a point load P should be applied at the upper end $y=0$ to ensure a valid area at $y=0$. A_0 can be calculated by $A_0 = \frac{P}{\sigma}$.

To visualize the outcomes of the mathematical solution given by Equation 3.4, the material properties of concrete C20/25 have been utilized as input parameters for the equation, as detailed in Table 3.1.

Input to the variables		
σ	Constant stress	13300 kN/m ² (Compressive strength)
γ	Specific weight	25 kN/m ³
P	Point load applied at $y=0$	2660 kN
A_0	Cross-sectional area at $y=0$	$A_0 = \frac{P}{\sigma}$ $A_0 = \frac{2660}{13300} = 0.2m^2$

Table 3.1: Input values to the variables in Eq 3.4

Fig 3.2 provides a graphical representation of Eq 3.4. Given that the cross-sections have a unit width of $b = 1m$, the area $A(y)$ is equivalent to the depth of the cross-sections $h(y)$. Therefore, when considering the location $y=0$, the area corresponds to $0.2m^2$, which can be expressed as $20cm$.

Form of constant stress: Self-weight

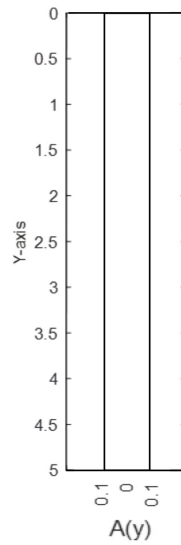


Figure 3.2: Static form of uniform strength: self-weight

The geometry appears as a rectangle with two linear boundaries instead of exhibiting an exponential behavior. This arises due to the substantial difference in magnitude between the value of σ and γ . Consequently, the term $e^{\frac{\gamma y}{\sigma}}$ tends toward one, leading to a negligible difference in the cross-sectional area at the bottom and top positions. In this example, the structure possesses a height of 5 meters, and the depth of the cross-section experiences a marginal increment, progressing from 20 cm to 20.19 cm.

3.1.2 FEA check: self-weight

The Grasshopper geometry model is built with the center axis y and varying cross-sections according to the derived equations. The input parameters have been mentioned in the previous section 3.1.1, see Table ???. The setup and results of the FEA model can be seen in Fig 3.3 and 3.4.

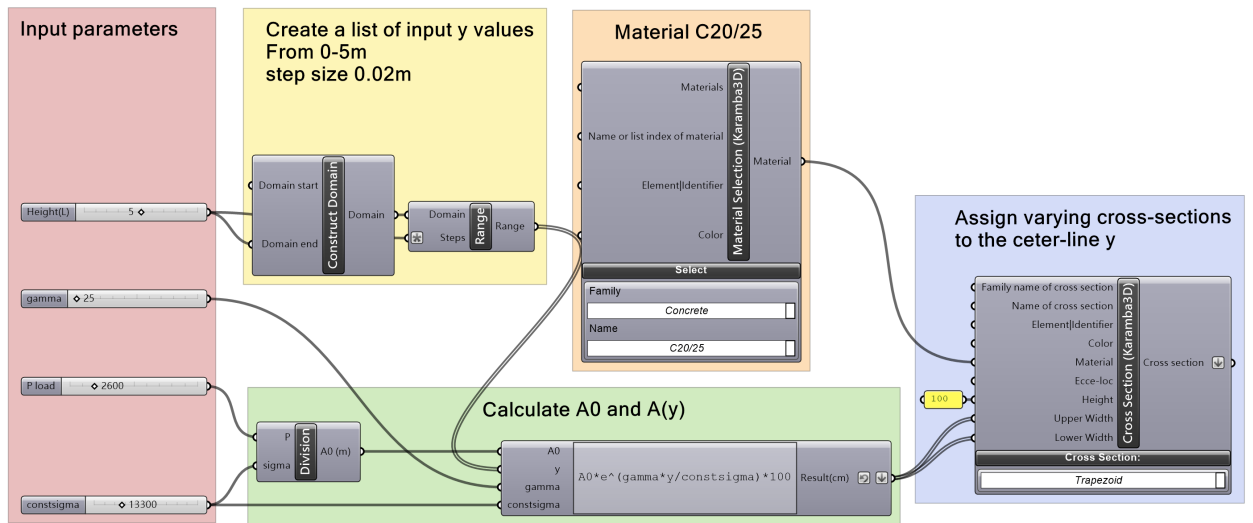


Figure 3.3: Geometry model setup in Grasshopper

The structural input for Karamba includes three components: 1.) elements, 2.) boundary and support conditions, and 3.) load cases.

Input to FEA tool Karamba3D	
Elements	“Line to beam”-component
Support	Moment fixed at $y=L=5m$
Loads	Gravity load+P load 2660kN at $y=0$

Table 3.2: Input components for Karamba3D: self-weight

The shape and the axial stress can be seen in Fig 3.4. It remains under constant compressive stress $13300kN/m^2$, which is the compressive strength of C20/25, in the entire structure. The area at $y = 0$ is $A_0 = 20cm$ and increases exponentially to $20.19cm$ at the fixed bottom end at $y=5$. Based on the analysis, it is evident that the influence of self-weight is minor when specifies a large number as constant stress σ .

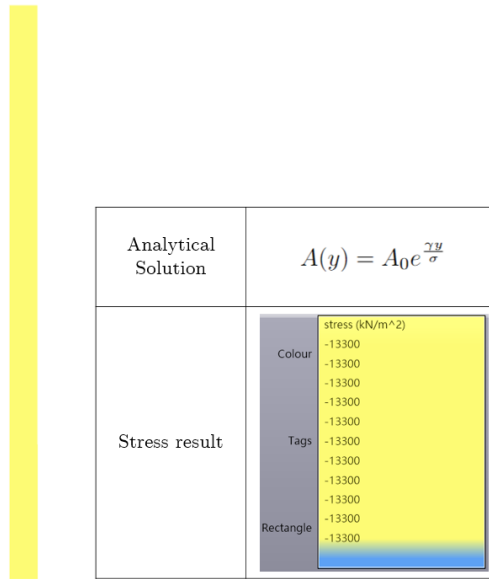


Figure 3.4: Stress result of the constant stress shape considering self-weight: Uniform compressive stress in the entire structure

3.2 Form of constant stress: uniformly distributed load q

Based on [4], it can be inferred that the maximum tensile and compressive stresses in a beam undergoing pure bending are directly proportional to the distance of the out-most fibers from the neutral axis of the cross-section. Therefore, when using a material with equal strength in tension and compression, it is logical to choose a symmetric cross-section where the centroid lies in the middle of the beam's height. This ensures that the same factor of safety is obtained for fibers in both tension and compression that will yield at the same time. In cases where the section is not symmetrical, the material is distributed between the top and bottom in such a way that the centroid is still located at the center of its height.

3.2.1 Analytical derivation: uniformly distributed lateral load q

To obtain the form of constant stress under a uniformly distributed load q , it can be predicted that the section modulus S varies along the height y in the same proportion as the bending moment M resulting from the load, see Eq 3.5. In this way, the maximum bending stress located at the out-most fibre remains constant σ along the height of the structure. This condition is advantageous in terms of material usage as each cross-section would have the minimum required area to meet the strength requirements.

Fig 3.5 (a) shows a free-standing structure with height L loaded with the uniformly distributed lateral load q . The bending moment at distance y is equal to $\frac{qy^2}{2}$. In order to gain the form of uniform strength, the section modulus should be in proportion to y , explained in Eq 3.6. The structure has a unit width b in the direction perpendicular to the plane of the paper, and a changing depth $h(x)$ of cross-sections.

Accordingly,

$$\frac{M}{S} = \sigma \tag{3.5}$$

where : σ = constant maximum bending stress

S = section modulus

When the cross-section is a rectangle with unit width b and varying depth $h(y)$, the section modulus S can be written as below:

$$\frac{M}{bh(y)^2/6} = \sigma$$

Then, the maximum bending stress at $y=L$ and at any point y should equal to constant σ to obtain the form of equal strength. Eq 3.6 shows the linear relation between $h(y)$ and h_L .

$$\frac{qL^2/2}{bh_L^2/6} = \frac{qy^2/2}{bh(y)^2/6} = \sigma$$

$$\frac{h(y)}{h_L} = \frac{y}{L}, \quad \text{where } h_L = L\sqrt{\frac{3q}{b\sigma}} \tag{3.6}$$

$$h(y) = y\sqrt{\frac{3q}{\sigma b}} \tag{3.7}$$

To visualize the constant maximum bending stress represented by Eq 3.7 with Matlab, the input for symbolic variables is:

Input to the variables		
σ	Constant stress	1300 kN/m ² (tensile strength)
q	Uniformly distributed lateral load	2 kN/m
b	Unit width	1m

Table 3.3: Input values to the variables in Eq 3.7

In contrast to the previous case where self-weight induced only compressive stress in the structure, the specified constant stress σ is the tensile strength of the concrete instead of compressive strength in this example. This deviation is justified by the fact that tensile stress is more critical in terms of material. Consequently, if the structure is subjected to tensile stress, the design should be based on this criterion. Fig 3.5 (b) shows the constant stress shape of $h(y)$ in Eq 3.7. To sum up, the form of uniform strength considering only uniformly distributed lateral load results in linear varying cross-sections along the center axis.

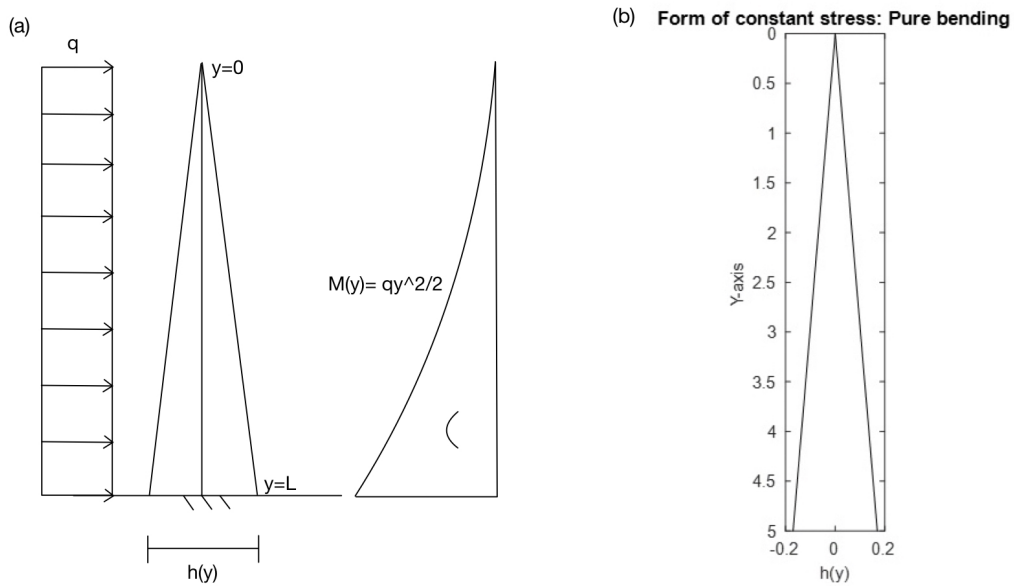


Figure 3.5: (a) Geometry and loading (b) Form of constant maximum bending stress: uniformly distributed load q

3.2.2 FEA check: uniformly distributed load q

The Grasshopper geometry model is again built with the center axis y with the assigned cross-sections varying in accordance with the derived equations $h(y)$. The specific input parameters utilized for the model are provided in Table 3.3, and the process of constructing the geometry model can be referenced from Fig 3.3.

The components of Karamba3D include:

Input to FEA tool Karamba3D	
Elements	“Line to beam”-component
Support	Moment fixed at $y=L=5m$
Loads	Uniformly distributed lateral line load $q=2kN/m$ applied to the center line of the structure

Table 3.4: Input components for Karamba3D: uniformly distributed load q

The shape and the axial stress can be seen in Fig 3.6. As depicted in the figure, the maximum tensile bending stress and the maximum compressive bending stress remain constant stress $1300kN/m^2$, which is the tensile strength of C20/25, on both boundaries of the structure. The depth of the cross-section increases from 0 to $27.17cm$ at the fixed bottom.

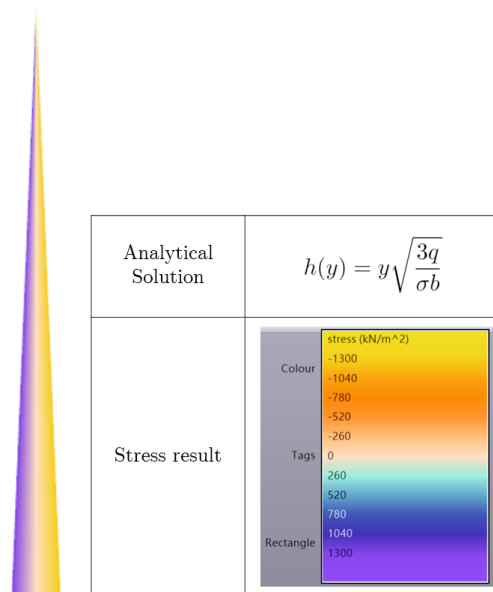


Figure 3.6: Stress result of the constant stress shape considering uniformly distributed lateral load q : Uniform maximum bending stress

3.3 Form of constant stress- load combination

Extending from the above analytical derivation with either self-weight or uniformly distributed load q , this section combines the two load cases and searches for the form of constant stress.

The present section covers three distinct cases, namely, Section 3.3.1 to Section 3.3.4, which address the establishment of constant stress on the tension side of the structure. Secondly, Section 3.3.5 and Sec-

tion 3.3.6 investigate the possibility of maintaining constant stress on both the tension and compression boundaries of the structure. The criteria for Section 3.3.7 are twofold: 1) Zero bending moment throughout the structure, and 2) Constant stress in all cross-sections. To satisfy these criteria, it is imperative to determine the center-line profile of the structure and subsequently derive the varying cross-sections.

3.3.1 Analytical derivation: constant maximum tensile stress ($\sigma = 0$)

The first specified criterion when considering the combined load case of self-weight + uniformly distributed load q is: the addition of the maximum tensile bending stress induced by external loading q , and the stress results from self-weight should maintain constant stress at the extreme side in tension, see Eq 3.8. Specifically, the critical situation for a material with a lower tensile strength compared to compressive strength is to ensure that the maximum allowable tensile stress in the structure is not exceeded. In each cross-section along the height axis y , the maximum bending stress occurs at the extreme fibre, while the stress induced by self-weight remains constant. Therefore, the logical criterion when adopting uniform stress theory in this case is to fix the stress at one boundary of the structure along the height to tensile strength, shown in Fig 3.7. The derived equation results in a symmetric shape, ensuring that no matter where the uniformly distributed load q comes from, either from the right or left, the tensile boundary remains under constant stress.

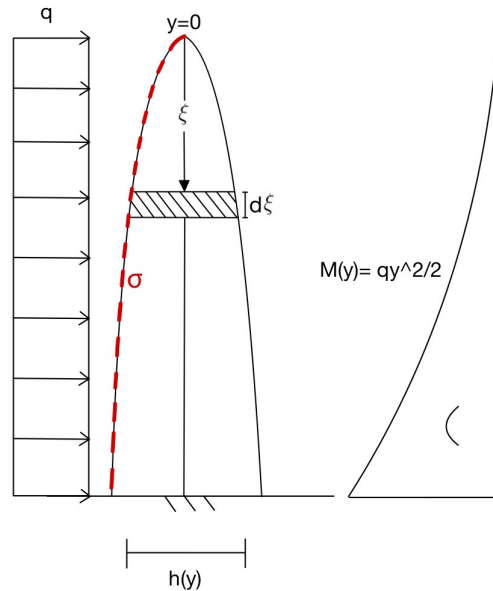


Figure 3.7: Geometry and loading: load combination

$$\frac{qy^2/2}{bh(y)^2/6} - \frac{\gamma b \int_0^y h(\xi)d\xi}{bh(y)} = \sigma \quad (3.8)$$

where : σ = constant maximum bending stress

γ = specific weight

ξ = the coordinates along beam axis for an arbitrary cross-section

b = unit width of the cross-section

$h(y)$ = depth of the cross-section at y

q = uniformly distributed load

The first term is the maximum tensile bending stress from load q , while the second term is the compressive stress from self-weight. Rearrange Eq 3.8, the boundary condition is determined when $y=0$:

$$h(0) = 0 \tag{3.9}$$

To simplify the math problem, firstly, the constant σ is set to zero at the right-hand side, and multiply the equation by $h(y)$:

$$\frac{3qy^2}{bh(y)} - \gamma \int_0^y h(\xi)d\xi = 0$$

Derive the equation with respect to y .

$$\frac{6qy}{bh(y)} - \frac{3qy^2h'(y)}{bh(y)^2} - \gamma h(y) = 0 \tag{3.10}$$

With the boundary condition Eq 3.9, the exact solution of $h(y)$ in Eq 3.10 is solved with Matlab:

$$h(y) = \frac{3\sqrt{2\gamma qy}}{2\gamma} \tag{3.11}$$

From the solution, it is noticeable that the depth of the cross-section $h(y)$ has a basic shape of \sqrt{y} along the y -axis, see Fig 3.8. The input for symbolic variables in Eq 3.11:

Input to the variables ($\sigma = 0$)		
q	Lateral load	2 kN/m
γ	Specific weight	25 kN/m ³

Table 3.5: Input values to the variables in Eq 3.11

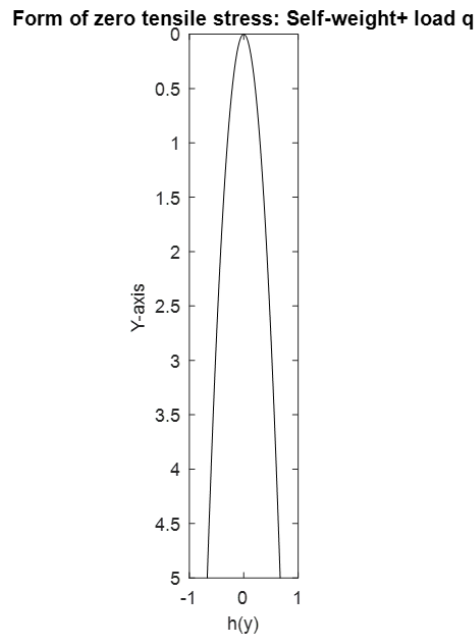


Figure 3.8: Form of constant 0 tensile stress: load combination

3.3.2 FEA check: constant maximum tensile stress ($\sigma = 0$)

The Grasshopper geometry model is again built with the center axis y and varying cross-section according to the derived equations $h(y)$. The input parameters are shown in Table 3.5. As the constant stress σ is specified as zero, it is expected that the tension boundary has constant zero stress in the entire structure. The process of constructing the geometry model can be referenced from Fig 3.3.

The components of Karamba3D include:

Input to FEA tool Karamba3D	
Elements	“Line to beam”-component
Support	Moment fixed at $y=L=5m$
Loads	Gravity load + Uniformly distributed lateral line load $q=2kN/m$ applied to the center line of the structure

Table 3.6: Input components for Karamba3D: load combination

The shape and the axial stress can be seen in Fig 3.9. The stress on the tension boundary indeed remains constant zero stress. The depth of the cross-section increases from 0 to 120cm at the fixed bottom $y=5m$. Evidently, the figure illustrates that to maintain zero tensile stress in the structure as specified, a huge amount of material is necessary.

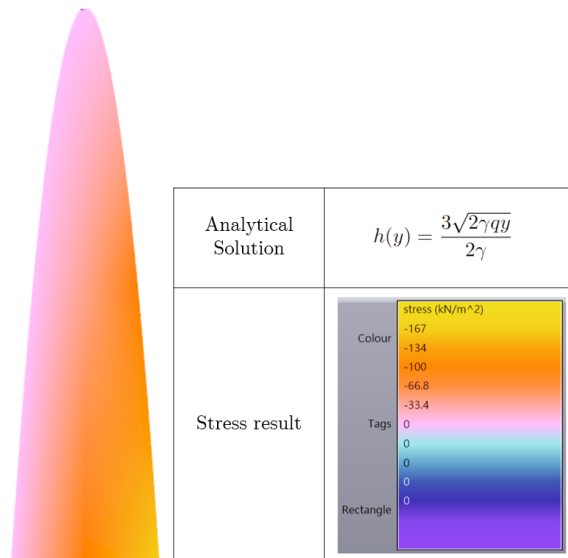


Figure 3.9: Results of the constant stress shape (load combination): zero tensile stress on the tension boundary

3.3.3 Analytical derivation: constant maximum tensile stress

In this section, the basic formula is the same as Eq 3.8 in the above Sec 3.3.1. However, different from the previous part that set the constant $\sigma = 0$ to simplify the math problem and derive the closed-form solution, the constant stress σ here is a non-zero value. Eq 3.8 can be written as follow:

$$\frac{3qy^2}{bh(y)} - \gamma \int_0^y h(\xi)d\xi = \sigma h(y)$$

Derive the equation with respect to y .

$$\frac{6qy}{bh(y)} - \frac{3qy^2 h'(y)}{bh(y)^2} - \gamma h(y) = \sigma h'(y) \quad (3.12)$$

The boundary condition is the same as above Eq 3.9. However, there is no closed-form solution to the above non-linear differential equation. Accordingly, numerical methods are needed to approximate the solutions.

ODE113 is a numerical solver in MATLAB for initial value problems, which means it is used to solve differential equations where the value of the function and its derivative are known at a single point. It uses an explicit Runge-Kutta (4,5) formula for non-stiff differential equations and an efficient method based on backward differentiation formulas (BDF) for stiff differential equations. It is an adaptive step-size solver, meaning that it automatically adjusts the step size to achieve the desired level of accuracy. It is also a variable-order solver, which means that it can adjust the order of the method to estimate the solution at each time step and balance the errors in the approximation. In summary, the reason to choose ODE113 to solve the equation here is that it's a robust and efficient solver for non-linear differential equations, which provides accurate and reliable numerical solutions for a wide range of problems.

Now, rearrange Eq 3.12 to get $h'(y)$ as the second input argument for ODE113:

$$h'(y) = \frac{6qyh(y) - \gamma h(y)^3}{\sigma h(y)^2 + 3qy^2} \quad (3.13)$$

With y as the independent variable and h as the dependent variable $h(y)$, the code below is provided for Matlab ODE113:

```

q = 2;
γ = 25;
σ = 1300;

yspan = 0 : 0.01 : 5;

h0 = 0.001;

[y,h] = ode113(@(y,h);(6qyh - γh3)/(σh2 + 3qy2),yspan,h0);

plot(-h/2,y,'k');

hold on;

plot(h/2,y,'k')

set(gca, 'YDir', 'reverse');

title('Form of constant tensile stress: Self-weight+ load q');

xlabel('h(y)', 'FontSize', 10);

ylabel('Y-axis', 'FontSize', 10);

```

As indicated in the third line of the code, the input step size for 'y' is set to 0.01m, from y=0 to 5m. The ODE113 solver approximates the dependent value 'h(y)' for each input 'y' to fit equations Eq 3.12 and Ed 3.13. This process generates a total of 501 'h(y)' values. Table 3.7 displays some intermediate input 'y' values at intervals of 0.5m along with their corresponding 'h' values, with units in meters.

y	h
0	0.001
0.5	0.0269
1	0.0540
1.5	0.0809
2	0.1077
2.5	0.1344
3	0.161
3.5	0.1875
4	0.2139
4.5	0.2402
5	0.2671

Table 3.7: Input y and output h

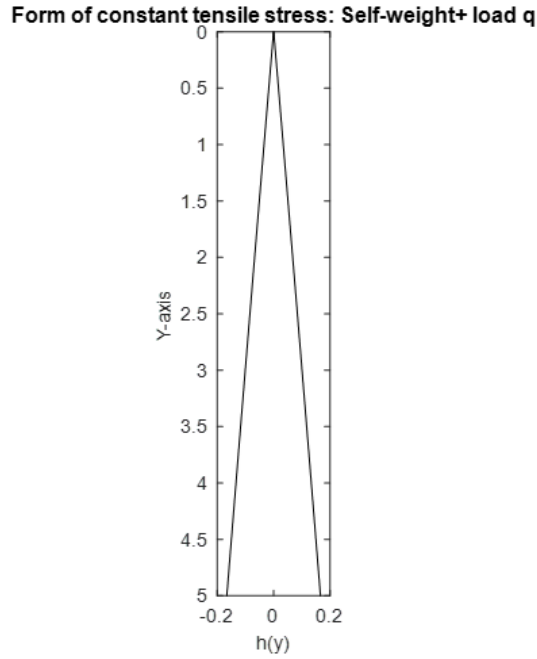


Figure 3.10: Result of ODE113

3.3.4 FEA check: constant maximum tensile stress

The Grasshopper geometry model is constructed using the values obtained from the Matlab solver ODE113. The cross-sections are assigned to each 0.02-length beam segment along the center-line 'y' following Table 3.7. The structural input for Karamba can be found in Table 3.6.

The results of the FEA model can be seen in Fig 3.11. As evidenced by the Karamba model, the numerical approximation derived from Matlab ODE113 is accurate, as the maximum tensile stress on the tension boundary remains constant $\sigma = 1300kN/m^2$.

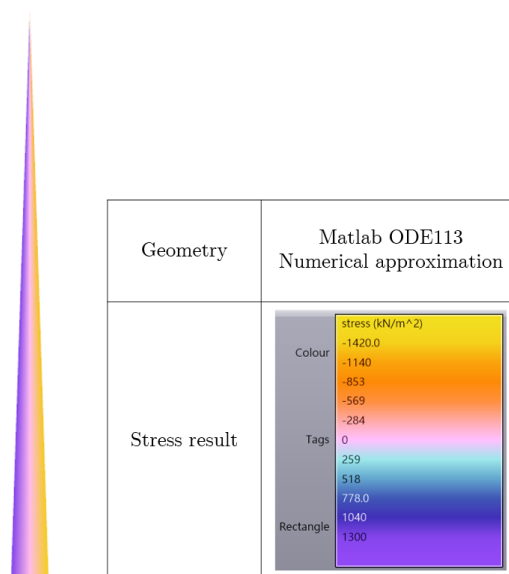


Figure 3.11: Results of the constant maximum tensile stress shape (load combination)

With the strict criterion of zero stress on the tension boundary along the height of the structure, Fig 3.9 in Sec 3.3.2 has a depth of 120 cm at the bottom. Compared with that, $h(y=L)$ in this case is only 26.71 cm. This indicates that it's much more efficient to set the constant stress to a non-zero allowable tensile stress instead of 0. On the other hand, Fig 3.6 in Sec 3.2.2 has a depth of 27.17 cm at the bottom when considering only stress from uniformly distributed load q , the value is also larger than the result in this case. That is because the compressive stress from self-weight is in favor of the tension side, the material can be decreased accordingly. However, there is no big difference between the two shapes when taking into account self-weight which has only a minor influence on the structure.

3.3.5 Analytical derivation: constant stress on both boundaries

The previous sections considered the criterion of constant stress on the tension boundary, whereas this section explores the possibility of a shape that maintains constant stress on both boundaries.

As we know, self-weight induces compressive stress, while a uniformly distributed load q creates tensile stress on one side and compressive stress on the other. Achieving constant stress on both sides seems unlikely with only these two stress types. Therefore, the concept is to search for additional stress required to fully balance out the stress induced by load q , namely, the bending stress produced by the geometry's eccentricity, see the explanation shown in Fig 3.12.

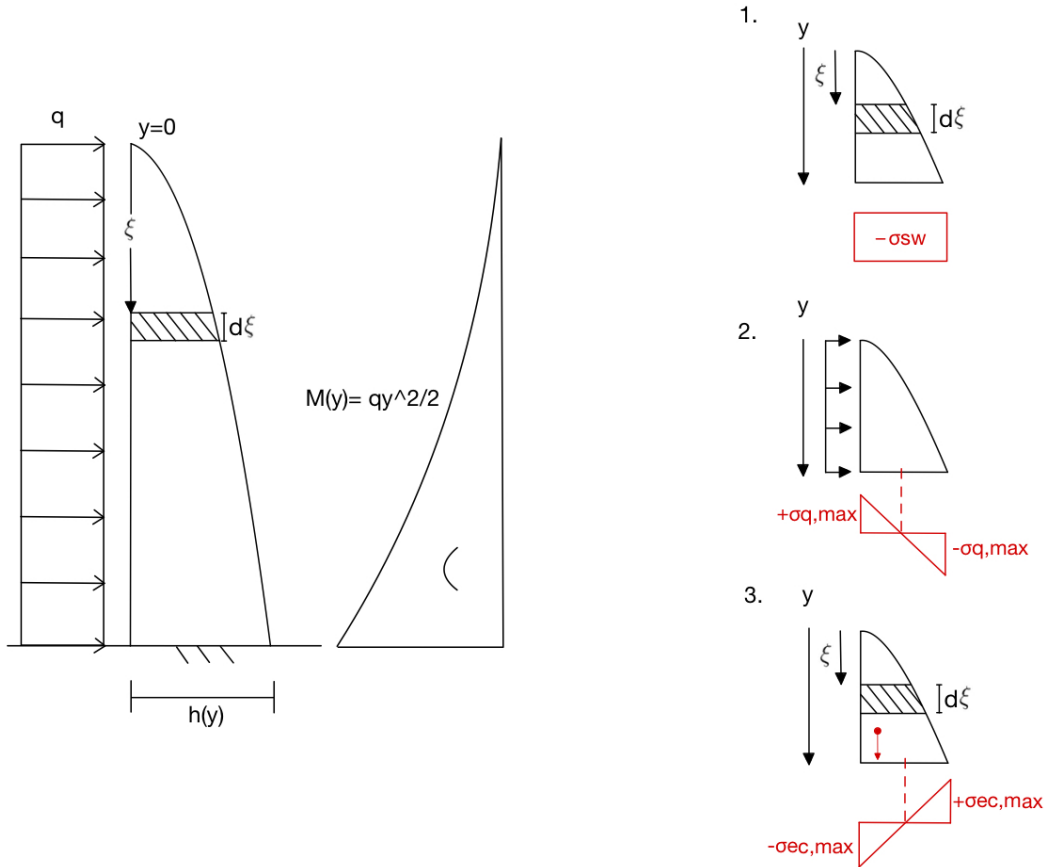


Figure 3.12: Geometry, loading and stress

1. Stress from self-weight:

$$w(y) = \gamma b \int_0^y h(\xi) d\xi, \quad \text{where } w(y) = \text{self-weight at } y \quad (3.14)$$

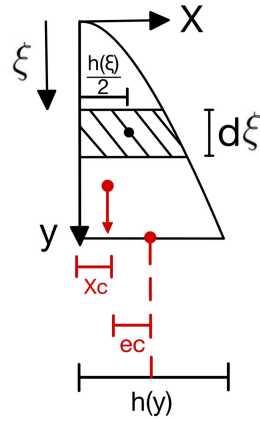
$$\sigma_{sw} = \frac{w(y)}{h(y)b} \quad (3.15)$$

2. Stress from uniformly distributed load q

$$\sigma_{q,\max} = \frac{M_q(y)}{bh(y)^2/6}, \quad \text{where } M_q(y) = \frac{qy^2}{2}$$

$$\sigma_{q,\max} = \frac{3qy^2}{bh(y)^2} \quad (3.16)$$

3. Stress from eccentricity


 Figure 3.13: center of mass: x_c , Eccentricity: ec

$$x_c = \frac{\int_0^y \frac{h(\xi)}{2} h(\xi) d\xi}{\int_0^y h(\xi) d\xi} \quad (3.17)$$

$$ec(y) = \left| \frac{h(y)}{2} - x_c \right| \quad (3.18)$$

With Eq 3.14, Eq 3.17, and Eq 3.18, the bending moment from the eccentricity of self-weight can be expressed as:

$$M_{ec}(y) = w(y) \cdot ec(y) = \gamma b \int_0^y h(\xi) d\xi \cdot \left| \frac{h(y)}{2} - \frac{\int_0^y \frac{h(\xi)}{2} h(\xi) d\xi}{\int_0^y h(\xi) d\xi} \right|$$

$$\sigma_{ec, \max} = \frac{6M_{ec}(y)}{bh(y)^2} \quad (3.19)$$

Now, we can set up the equilibrium equation describing constant maximum stress on both boundaries of the structure:

$$-\sigma_{sw} + \sigma_{q, \max} - \sigma_{ec, \max} = -\sigma_{sw} - \sigma_{q, \max} + \sigma_{ec, \max} = \sigma \quad (3.20)$$

where : σ = constant stress

From Eq 3.20, the following system of equations needs to be solved:

$$\sigma_{q,\max} = \sigma_{ec,\max} \quad (3.21a)$$

$$\sigma_{sw} = \sigma \quad (3.21b)$$

Substitute each term with specific expressions, We can then rewrite Eq 3.21 to:

$$\frac{3qy^2}{bh(y)^2} = \frac{6 \cdot \gamma b \int_0^y h(\xi) d\xi \cdot \left| \frac{h(y)}{2} - \frac{\int_0^y \frac{h(\xi)}{2} h(\xi) d\xi}{\int_0^y h(\xi) d\xi} \right|}{bh(y)^2} \quad (3.22a)$$

$$\frac{\gamma b \int_0^y h(\xi) d\xi}{bh(y)} = \sigma \quad (3.22b)$$

However, the solution $h(y)$ that satisfies Eq 3.22a and Eq 3.22b doesn't exist. The reason is that both equations have their own closed-form solutions which contradict each other. Eq 3.22a has boundary condition:

$$h(0) = 0 \quad (3.23)$$

With the boundary condition, the closed-form solution to Eq 3.22a is solved with Matlab:

$$h(y) = \frac{2\sqrt{\gamma q y}}{\gamma} \quad (3.24)$$

To visualize $h(y)$, input for the variables in Eq 3.24 can be found in Table 3.5. Plot the equation with Matlab:

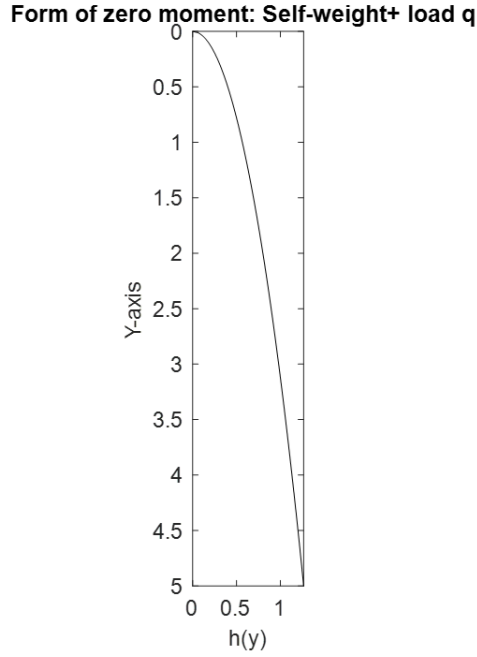


Figure 3.14: Visualization of Eq 3.24

On the other hand, the solution to Eq 3.22b is also solved with Matlab. Firstly, rearrange the equation and derive it with respect to y :

$$h(y) = \frac{\sigma h'(y)}{\gamma} \quad (3.25)$$

The solution to Eq 3.25 is:

$$h(y) = C e^{\frac{\gamma y}{\sigma}} \quad (3.26)$$

The result ends up the same as Eq 3.2 in Sec 3.1.1 which considers only the self-weight of the structure. Also, Eq 3.3 shows that C is the depth at $y=0$ and it should be a non-zero value. Therefore, the fact that $h(0)$ is a non-zero constant instead of zero contradicts the boundary condition of Eq 3.22a.

Though there is no solution to this case, Eq 3.24 gives a shape that is able to balance the bending moment from load q by its self-weight and becomes momentless. The advantage is that without the existence of a bending moment, there is no resulting tensile stress in the structure. This is particularly beneficial for materials with low tensile strength. However, because the constant stress state is not fulfilled, the material usage is not as efficient as in the previous cases.

3.3.6 FEA check: zero bending moment, eccentricity + uniformly distributed load q

The geometry model, based on the expression given by Eq 3.24, is created using Grasshopper to verify the absence of bending moment in the structure. The input values for the variables in this equation are provided in Table 3.5. The structural parameters used as input in Karamba are consistent with the details specified in Table 3.6.

The shape and the axial stress can be seen in Fig 3.15. As shown in the label in Fig 3.15, no tensile stress which implies no bending moment exists in the structure. However, the criterion of constant stress is not met, resulting in an overall compressive stress level that is significantly lower than the material's capacity. The value of $h(y)$ at the bottom of the structure is 113.14 cm.

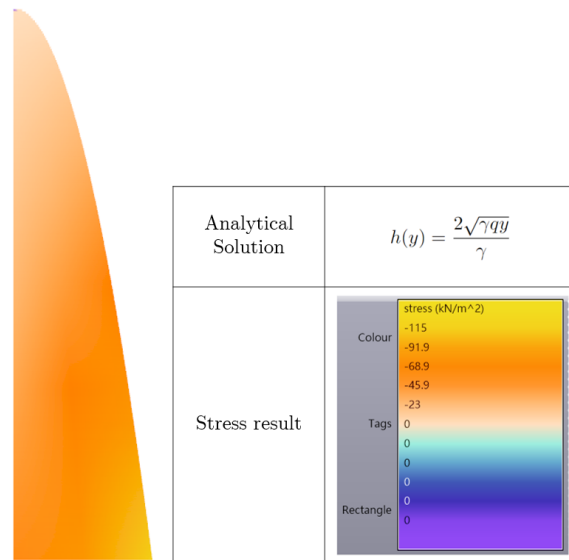


Figure 3.15: Results of the zero moment shape

3.3.7 Analytical derivation: center line profile

The final solution is inspired by the constant stress arches [3] in 2.1.1.3. The criteria for this case include: 1.) zero bending moment and 2.) constant stress in all the cross-sections. The derivation process is similar to the technique used in the paper. Firstly, establish the equilibrium equations, including horizontal and vertical force equilibrium, and moment equilibrium. All the used variables can be seen in Fig 3.16. The length of the wall measured along its center-line profile is denoted as C , where the applied load includes both a uniformly distributed load q and the self-weight of the wall. In order to maintain constant stress σ , the arch is designed with varying cross-sectional area A along its length. The wall is considered pin-ended if no bending moment exists in the structure, as assumed in [3]. With the vertical reaction denoted by V , and the horizontal reaction qL at the support. An arbitrary point between O and P is identified by the coordinate ξ along the x -axis and the arch length σ measured from O . The internal

forces acting on the arch cross-section at a given cross-section P include T , compressive force; S , shear force; and M , bending moment.

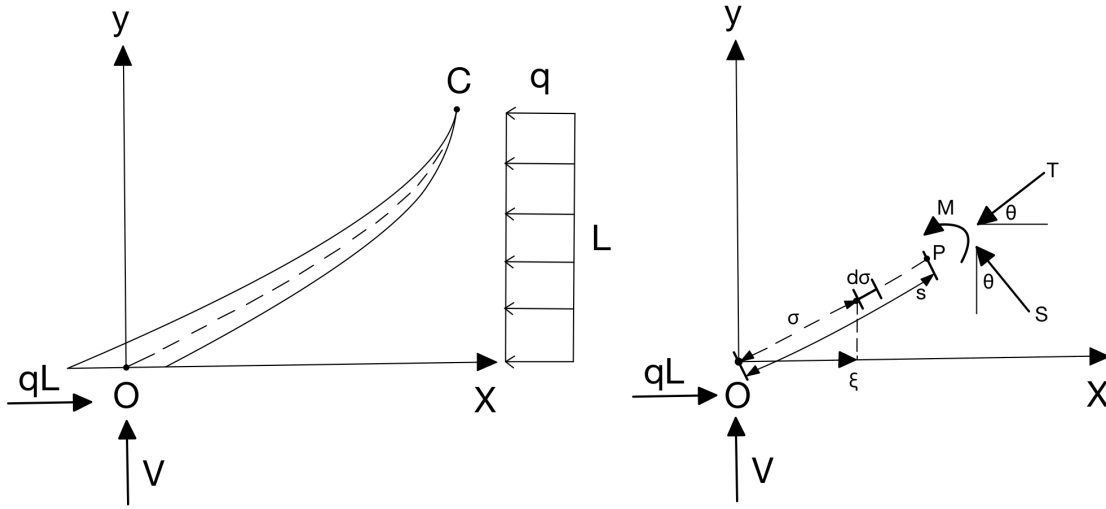


Figure 3.16: A segment of the center line

1. Horizontal equilibrium, $\sum F_H = 0$:

$$-S \sin \theta - T \cos \theta + qL - qy = 0 \quad (3.27)$$

2. Vertical equilibrium, $\sum F_V = 0$:

$$S \cos \theta - T \sin \theta + V - \int_0^s \gamma A d\sigma = 0 \quad (3.28)$$

Solve T (axial force) and S (shear force) with Matrix method:

$$\begin{bmatrix} -\sin \theta & -\cos \theta \\ \cos \theta & -\sin \theta \end{bmatrix} \begin{bmatrix} S \\ T \end{bmatrix} = \begin{bmatrix} qy - qL \\ \int_0^s \gamma A d\sigma - V \end{bmatrix}$$

The results are:

$$S = \left(\int_0^s \gamma A d\sigma - V \right) \cos \theta + (qL - qy) \sin \theta \quad (3.29)$$

$$T = -\left(\int_0^s \gamma A d\sigma - V \right) \sin \theta + (qL - qy) \cos \theta \quad (3.30)$$

3. Moment at S, $M_s = 0$:

$$M - Vx + qLy - \frac{qy^2}{2} + \int_0^s \gamma A(x - \xi) d\sigma = 0 \quad (3.31)$$

Divide Eq 3.31 with ds , and introducing the geometrical relation of ds , dx , dy :

$$\frac{dM}{ds} - V \cos \theta + qL \sin \theta - qy \sin \theta + \cos \theta \int_0^s \gamma A d\sigma = 0 \quad (3.32)$$

Substitute the expression of S in Eq 3.29 into Eq3.32 results in:

$$\frac{dM}{ds} + S = 0 \quad (3.33)$$

Eq 3.33 provides a constraint between M and S, which implies that the condition of zero moment is sufficient to imply zero shear in the structure. As explained in Section 3.3.6, it's possible for the free-standing structure to be moment less if the resulting bending moments from load q and eccentricity of self-weight have the same value but opposite sign in all the cross-sections. Accordingly, we can say that S should be equal to 0. With the explicit expression of vertical reaction force V :

$$V = \int_0^C \gamma A d\sigma \quad (3.34)$$

Insert Eq 3.34 into Eq 3.29, set S to zero, and divide by $\sin \theta$. Note that $\frac{\sin(\theta)}{\cos(\theta)} = \frac{1}{dx/dy} = \frac{1}{x'}$ as x is a function of y , $x(y)$, and now we can get:

$$\int_s^C \gamma A d\sigma = (qL - qy) \frac{1}{x'} \quad (3.35)$$

Derive Eq 3.35 with respect to y , it becomes:

$$\frac{-\gamma A}{\sin \theta} = \frac{-q}{x'} + (qL - qy) \frac{-x''}{x'^2} \quad (3.36)$$

The varying area A is known to be a dependent variable to y , therefore, it's necessary to substitute A with another expression in Eq 3.36. Since $S = 0$, Eq3.27 and Eq3.28 can be rewritten as:

$$T \cos \theta = qL - qy \quad (3.37)$$

$$T \sin \theta = \int_s^C \gamma A d\sigma \quad (3.38)$$

Also, in the absence of shear force, axial force T becomes:

$$T = \sigma A \quad (3.39)$$

With Eq 3.37, Eq 3.38, and Eq 3.39, varying cross-sectional area A can be expressed by:

$$A = \frac{qL - qy}{\sigma \cos \theta} \quad (3.40)$$

After substituting Eq 3.40 into Eq 3.36, and utilizing $\frac{1}{\sin \theta}$ as $\sqrt{1 + x'^2}$ and $\frac{1}{\cos \theta}$ as $\sqrt{\frac{x'^2+1}{x'^2}}$, the resulting expression for Eq 3.36 can be expressed as:

$$\frac{\gamma}{\sigma}(L - y)x'(x'^2 + 1) = x' + (L - y)x'' \quad (3.41)$$

As y is the independent variable and x is a function of y, Eq3.41 is a non-linear second-order differential equation. There are two boundary conditions: 1.) $x(0)=0$ as the center-line start from the origin (0,0), 2.) $x'(L)=0$, this can be observed from Eq 3.41 when $y=L$. Unfortunately, there is no analytical solution for the equation. However, we can again use ODE113 to find an approximate numerical solution. To do so, it's necessary to rearrange Eq 3.41 to get the expression of x'' first:

$$x'' = \frac{\gamma}{\sigma}x'(x'^2 + 1) - \frac{x'}{(L - y)} \quad (3.42)$$

Below is the code for Matlab ODE113. ode_system in the first line represents the system of equations as a function that accepts four input arguments: y, x, L, g, and s, where g represents specific weight γ and s represents constant stress σ . dxddy(1) is the first derivative of x(y), and dxddy(2) is the second derivative of x(y)

```

function dxdy=ode_system(y,x,L,g,s)

    dxdy=zeros(2,1);

    dxdy(1)= x(2);

    dxdy(2)= g*(x(2)^2 + 1)*x(2)/s - x(2)/(L - y);

end

```

Define the function handle with the aim of passing the predetermined values for L, g, and s to *ode_system*. The constant stress σ here is 1300 kN/m^3 as the tensile strength of C20/25, γ is 25 kN/m^3 . The input of the wall height is 0.5m. The assumed height is only 0.5m because the final shape is really tilted and not feasible, there is no reason to make it higher as it will be more tilted.

```

L = 0.5;

g = 25;

s = 1300;

yspan = 0 : 0.001 : L;

x0 = [0 10.377];

[y,x] = ode113(@(y,x) ode_system(y,x,L,g,s),yspan,x0);

```

The solution of x and x' can be retrieved from the workspace in Matlab and directly fed into the Grasshopper geometry model. Note that the numerical approximate solution of x' can solve the varying area A along the y-axis with Eq 3.40 and $\frac{1}{\cos \theta}$ as $\sqrt{\frac{x'^2+1}{x'^2}}$.

3.3.8 FEA check: center-line profile

The geometry model of Eq 3.41 is set up with Grasshopper to check if there is no bending moment in the structure and if the stress remains constant in all the cross-sections. The input parameters for Eq 3.40 is $q = 2 \text{ kN/m}$, y is from 0 to 0.5 meter-height with step 0.001. The structural input for Karamba includes the support: pin end at the bottom end, two load cases, uniformly distributed line load q acting on the center line, and self-weight of the structure that provides both axial compressive stress and bending stress due to eccentricity.

The geometrical input of the FEA model was taken from the numerical solutions of ODE113, including x and x' , which can solve the center line profile and the varying area respectively.

The center line profile is illustrated in Fig 3.17. Although the varying areas are not visible due to their extremely small size, the bending moments for all cross-sections are nearly zero. However, it is important to note that the resulting shape and cross-sectional area are not practical or feasible for a wall.

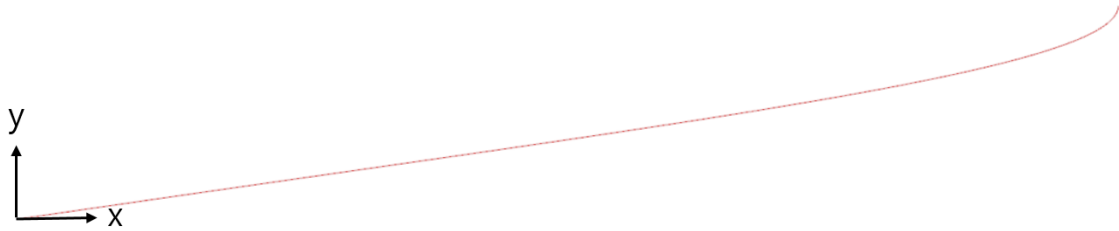


Figure 3.17: Results of the zero bending moment and constant stress shape

3.4 Discussion

This chapter presents the mathematical solutions of constant stress geometries under various load cases. The constant stress condition is derived from the uniform strength theory, which ensures that all parts of a structure are equally stressed (constant (maximum) stress) under specific loading conditions. When the specified constant stress equals the maximum allowable stress of the material, it maximizes the utilization of the entire structure.

In Sec 3.1, we derived the analytical solution for constant stress geometry under self-weight. The exponential increase of the cross-section in Eq 3.4: $A(y) = A_0 * e^{\frac{\gamma y}{\sigma}}$ is mainly influenced by the ratio of $\frac{\gamma}{\sigma}$. Typically, σ has a much higher value than γ . For example, in the case of a standing wall made of C20/25 concrete, σ is $13300kN/m^2$ (compressive strength), and γ is $25kN/m^3$ (specific weight of concrete). Consequently, the exponent $\frac{\gamma}{\sigma}$ is nearly zero, leading to a negligible increase in the cross-section depth of 0.19cm in a 5-meter-high structure, representing a percentage increment of 0.94%. Thus, for cases where σ significantly outweighs γ , the constant-stress geometry subjected to self-weight exhibits only a minor change in increasing the area.

In Sec 3.2, we derived the analytical solution for constant maximum stress geometry under uniformly distributed load q . As the maximum bending stress in a symmetric and homogeneous cross-section is proportional to the distance to the neutral axis, the maximum tensile bending stress is equal to the maximum compressive bending stress at one cross-section. Consequently, Fig 3.6 illustrates the same maximum stress on the tension and compression boundaries.

The last load case discussed in Sec 3.3 involves the combination of self-weight and uniformly distributed load. The criterion for this case is to achieve "constant maximum stress on the tension boundary," which leads to two distinctly different geometries depending on the specified constant stress σ equals 0 or 1300 kN/m^2 , the tensile strength of the C20/25 concrete. When $\sigma = 0$, an analytical solution was found. However, when $\sigma = 1300 \text{ kN/m}^2$, no analytical solution exists for this particular case, and numerical approximation is employed, resulting in a triangular geometry, similar to the form obtained under uniformly distributed load q only. Fig 3.18 displays a comparison of the three results.

Loads	Section 3.2 Uniformly distributed load q	Section 3.3 Self-weight + Uniformly distributed load q	Section 3.3 Self-weight + Uniformly distributed load q
Criterion	Constant maximum bending stress σ	Constant 0 tension boundary	Constant maximum tensile stress σ
	 <p data-bbox="485 1128 561 1151">Figure 3.7</p>	 <p data-bbox="826 1128 919 1151">Figure 3.11</p>	 <p data-bbox="1177 1128 1270 1151">Figure 3.13</p>
Bottom depth $h(y=L)$ cm	27.17	120	26.71

Figure 3.18: Comparison of the constant stress geometries

The middle and right graphs depict the forms of constant maximum tensile stress with $\sigma = 0$ and $\sigma = 1300$, respectively. It is evident that when allowing tensile stress to occur in the structure, the required material decreases significantly, resulting in a completely different geometry. The bottom depth decreases from 120 to 26.71 cm. When $\sigma = 0$, the structure achieves a compression-only form when subjected to bending moment. Though require more material, the advantage of compression-only configuration is remarkable when using materials with low tensile strength. Additionally, the symmetric shape ensures that the tension boundary always remains at the specified constant stress no matter whether the load comes from the left or right side, making it practical in real-world applications.

On the other hand, the difference between the left and right graphs lies in the inclusion of self-weight in the derivation. As self-weight generates compressive stress, it proves beneficial for supporting the side in tension, thereby requiring less material to maintain constant stress. The bottom depth decreases from 27.17 to 26.71 cm with the assistance of self-weight. However, it is surprising that the numerical

approximation of the right graph results in a similar linear shape, and the decrease in bottom depth is negligible. To determine if self-weight truly does not significantly influence the form of constant stress when the specified σ is non-zero, a comparison is conducted with various uniformly distributed loads q . As a precautionary measure, the scale of load q needs to be adjusted as the current value of $q=2\text{kN/m}$ may be relatively large for the structure, potentially making the influence of self-weight indistinguishable. Therefore, investigating the impact of self-weight under different loads q is essential to comprehend its significance in shaping the constant stress geometry.

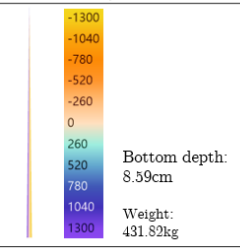
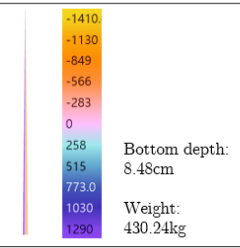
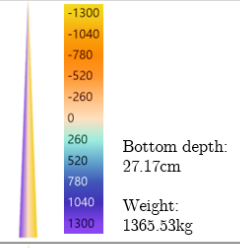
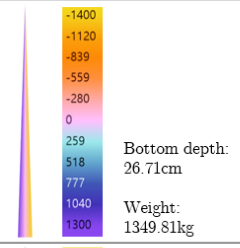
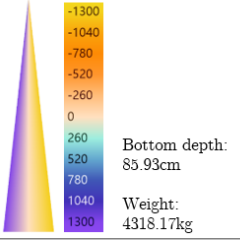
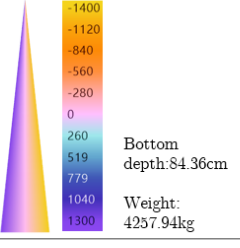
	Load q only	Load q + self-weight	Mass reduction
	$h(y) = y \sqrt{\frac{3q}{\sigma}}$	ODE113 approximation	
$q=0.2\text{kN/m}$	 <p>Bottom depth: 8.59cm Weight: 431.82kg</p>	 <p>Bottom depth: 8.48cm Weight: 430.24kg</p>	0.37%
$q=2\text{kN/m}$ (current case)	 <p>Bottom depth: 27.17cm Weight: 1365.53kg</p>	 <p>Bottom depth: 26.71cm Weight: 1349.81kg</p>	1.15%
$q=20\text{kN/m}$	 <p>Bottom depth: 85.93cm Weight: 4318.17kg</p>	 <p>Bottom depth: 84.36cm Weight: 4257.94kg</p>	1.39%

Figure 3.19: The influence of self-weight inclusion under different scales of uniformly distributed load q

The investigated variable q load includes 10 times larger and 10 times smaller values than the current value. The results clearly demonstrate that, regardless of the scale of the uniformly distributed load, the effect of self-weight on the constant stress geometry remains minor. The geometry retains its linear shape, and the reduction in weight is negligible. However, one notable finding is that as the load q increases, the positive influence of self-weight also slightly increases. While this influence remains small overall, it indicates that self-weight can play a more significant role in optimizing the structure’s constant stress geometry under higher load conditions.

The final comparison is between Fig 3.9 and Fig 3.15. Both load cases are the same, while one criterion aims for constant stress of zero on the tension boundary, and the other focuses on achieving zero bending

moment in the structure, achieved by utilizing the bending moment resulting from the eccentricity of self-weight.

Loads	Sec 3.3 Self-weight + Uniformly distributed load q	Sec 3.3 Self-weight + Uniformly distributed load q
Criterion	Constant 0 tension boundary	0 bending moment
	 Figure 3.11	 Figure 3.18
$h(y)$	$h(y) = \frac{3\sqrt{2\gamma q y}}{2\gamma}$	$h(y) = \frac{2\sqrt{\gamma q y}}{\gamma}$
Bottom depth $h(y=L)$ cm	120	113.14

Figure 3.20: Comparison of constant stress geometry and zero bending moment geometry

Fig 3.20 shows that the two graphs exhibit high similarity, with both analytical expressions containing a term of $\frac{\sqrt{\gamma q y}}{\gamma}$. This similarity may be attributed to the underlying equilibrium logic shared by both criteria: the effect of self-weight compensates for that of the uniformly distributed load. However, one approach seeks to equalize stress, while the other equalizes the bending moment. It is observed that the bottom depth of the right graph is slightly lower due to the use of eccentricity. However, the asymmetric shape may not be practical in the real world, where the load q might come from another side, resulting in this geometry working in the opposite way and worsening the stress condition.

In conclusion, this chapter's results demonstrate the effectiveness of constant stress geometries under various load cases and criteria. By utilizing analytical solutions and numerical approximations, we can achieve optimal designs that ensure efficient material usage and practicality in real-world applications.

3.5 Case study

In this case study, we explore the use of sustainable materials in the design of a noise barrier. As mentioned in Chapter 1, the chosen sustainable material is earth, which offers environmentally friendly and cost-effective advantages. To ensure long-term durability, we account for the influence of water and

frost on the material's properties by reducing its tensile strength from 0.49 MPa to 0.2 MPa and flexural strength from 1.25 MPa to 0.5 MPa.

The height of the noise barrier is set at 3 meters, and the density of the earth material is 2067 kg/m^3 (20.28 kN/m^3). Additionally, the uniformly distributed load q comprises two components: wind load as the primary action and aerodynamic pressure as the accompanying action.

Wind load is calculated by: Extreme wind pressure * wind pressure coefficient (wall zone D)=

$$0.49 \text{ kN/m}^2 * 1.2 = 0.59 \text{ kN/m}^2 \quad (3.43)$$

Aerodynamic pressure is calculated by: aerodynamic pressure * reduction streamlined train * combination factor=

$$0.24 \text{ kN/m}^2 * 0.6 * 0.8 = 0.12 \text{ kN/m}^2 \quad (3.44)$$

In SLS:

$$0.59 + 0.12 = 0.7 \text{ kN/m}^2 \quad (3.45)$$

The height of the noise barrier is set at 3 meters, and the density of the earth material is determined to be (20.28 kN/m^3). Additionally, the uniformly distributed load q comprises two components: wind load as the primary action and aerodynamic pressure as the accompanying action.

Using the real values as inputs to Eq 3.11, the optimized bottom depth is calculated to be 68 cm, and the total weight of the structure is estimated at 34213 kg.

The sustainable noise barrier is designed and built at the InnovA58 site. Remarkably, the analytical derivation indicates that no tension occurs in the structure, eliminating the need for reinforcement to handle tension forces. Moreover, the conventional concrete strip foundation commonly used for noise barriers is unnecessary in this case. Instead, the structure stands freely on a surface gravel foundation. The gravel foundation not only provides a stable base but also aids in efficient water drainage and prevents capillary action that might otherwise harm the structure.

To enhance sound insulation, a step-wise part is added on top of the base shape derived from the analytical solution. This ensures that the noise barrier effectively serves its intended purpose.



Figure 3.21: Sustainable noise barrier built at the InnovA58 site

In conclusion, this case study showcases the successful application of constant stress geometry in the design of a noise barrier, offering an eco-friendly and economical solution while maintaining structural integrity.

Chapter 4

Numerical structural optimization-2D

Sec 2.2 has elaborated the general numerical structural optimization techniques. Topology optimization focuses on determining the optimal distribution of material within a given design space, allowing for the identification of crucial regions or patterns that provide optimal structural performance. This process helps obtain an initial idea of the overall geometry and layout of the structure, which should be the optimal topology.

Once the topology optimization provides a fundamental model, shape optimization can be employed to refine further and optimize specific design variables. Shape optimization involves modifying the geometry or boundaries of the structure to improve specific performance criteria, such as stress distribution, displacement, or other design objectives. It allows for more precise adjustments and design fine-tuning based on given requirements or constraints.

In conclusion, preliminary design benefits greatly from topology optimization. Shape optimization, on the other hand, is more advanced but relies on a foundational design to establish the initial parameters of the optimization problem. When the problem is adequately defined and parameterized, shape optimizations hold significant potential for achieving optimal outcomes [51]. By integrating topology optimization and shape optimization techniques, designers can benefit from an iterative process that starts with a coarse design approximation and progressively refines it to achieve a more sophisticated and optimized shape. This approach can help balance structural performance, manufacturability, and other design considerations.

The purpose of this chapter is to compare the numerical optimized results with the analytical representation of shapes derived from the previous Chapter 3. The procedures for integrating topology optimization

and shape optimization are as follows:

- 1.) Validate Karamba3D "BESO for Shells"-component's ability to include self-weight in topology optimization.
- 2.) Conduct topology optimization and compare it with results from Sec 3.3.
- 3.) Find an efficient parameterized interpretation of topology-optimized geometry to further perform shape optimization.
- 4.) Write a penalty function to combine constraints (maximum allowable stress and minimum thickness) into the objective function.
- 5.) Retrieve the least weight combination of design variables as the optimized result.

4.1 Validation of Grasshopper's Topology Optimization Tool

It is crucial to consider the impact of self-weight during the topology optimization procedure, as to compare the numerical results with analytical results which include self-weight in the derivation. Consequently, the first step is to assess the capability of the topology optimization tool to incorporate self-weight considerations. In this study, the chosen tool for this purpose is the "BESO for Shells"-component in Karamba3D, as it offers an intuitive approach for defining gravity loads, as discussed in Sec 2.2.3.2.

In Section 2.2.2, we discussed the application of the extended BESO algorithm to incorporate the effect of self-weight in each iteration of the topology optimization process. As demonstrated in the first example, when considering a rectangular design domain measuring $1m \times 0.5m$ with pin supports at both ends, the optimization resulted in an arch-shaped structure after removing 85 % of the material [9]. Building upon this assumption:

Material: Young's modulus of 200 GPa, Poisson's ratio of 0.3, and a density of 78 kg/m^3

BESO parameters: ER = 3%, ARmax = 2%, $r_{min} = 30 \text{ mm}$, Target ratio 15 %

The topology optimization conducted with Karamba resulted in a shape similar to Fig 2.14 [9]. Notably, the "BESO for Shells" component in Karamba3D utilizes the soft-kill method, which suggests that the expected result should be closer to Figure (a) as illustrated in the paper [9]. However, the obtained result appears to resemble Figure (b) instead. This discrepancy could be attributed to the absence of a user-defined input for the penalty factor q in Karamba, which is set to 5 in the referenced paper.

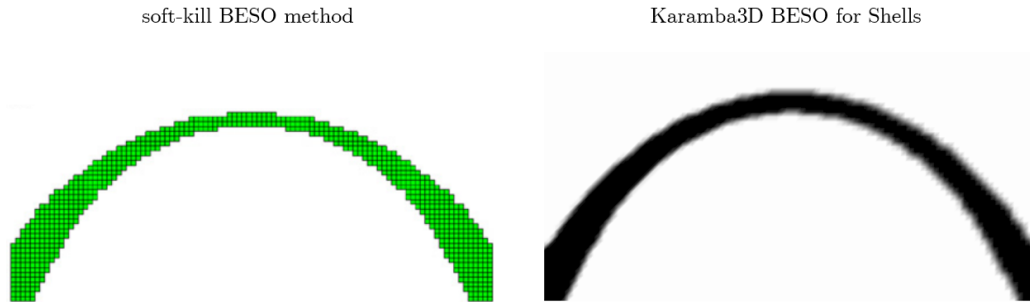


Figure 4.1: Comparison of BESO soft-kill result from [9] example 1 and Karamba3D result

In the second example, both self-weight and a point load F are applied to the classic MBB beam. With the same material properties and parameters setting, except for the Target ratio $\bar{40}$ %, Karamba is able to generate similar results shown in Fig 2.15, see the comparison below.

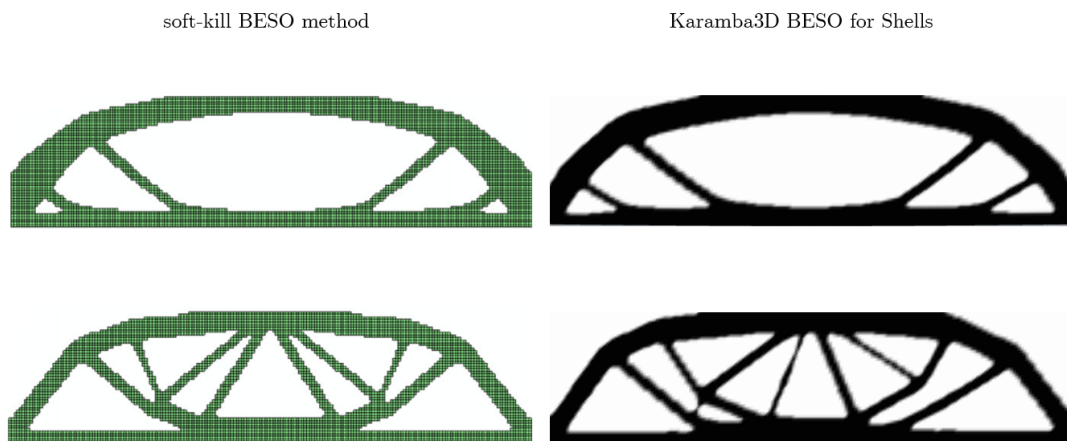


Figure 4.2: Comparison of BESO soft-kill results from [9] example 2 and Karamba3D result

The two examples presented serve as validation for the "BESO for Shells" component in Karamba3D, demonstrating its capability to generate satisfactory results while considering the influence of self-weight. This successful validation allows for the continuation of the research.

4.2 Topology optimization

Topology optimization was conducted in this section to gain initial insights into the most efficient shape. The assumptions are the same as the ones made in the analytical derivation in Sec 3.3.6.

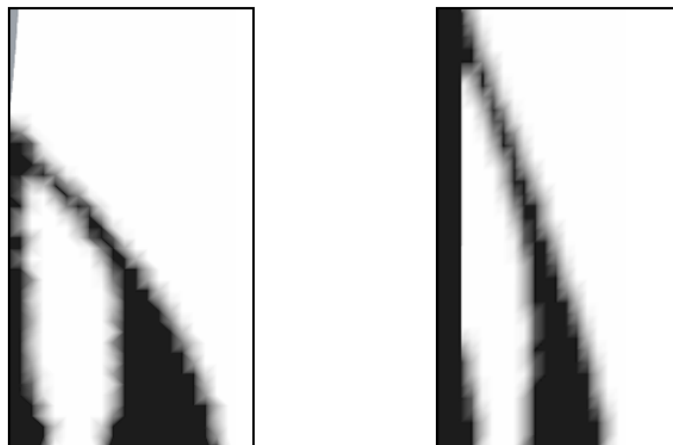
4.2.1 Topology optimization model setup

The design space was defined as a rectangular area with dimensions of 1.6m x 5m. The selected material for the optimization was concrete C20/25 with a specific weight of $\gamma = 25kN/m^3$ and Young's modulus of $E = 200$ GPa. The load combination consisted of the self-weight of the structure plus a uniformly distributed load of $q = 2kN/m$ applied on the left boundary of the design space. The support condition was set as a moment fixed at the bottom end. Additionally, a mesh size of 0.1m x 0.1m was chosen.

It's somewhat tricky with the "Loads"-component to demonstrate line load for mesh, as "MeshLoad" only takes surface loads. To properly transfer line load to the mesh shell employed here, short truss elements that have the same length as the mesh size were integrated at the loaded boundary using Karamba3D's 'MeshBreps'-component, in order to take the block load. The cross-sectional area of such intermediate truss elements must be extremely small, or else the structural analysis results will be influenced.

Following the preparation of the model, topology optimization was conducted to determine the optimal shape. The initial result is depicted in Figure 4.3 (a). The graph reveals that the mesh at the top left corner experiences the greatest displacement and is therefore unable to effectively transfer the line load anymore. Consequently, material in that region is removed. However, it is important to maintain a fixed height of 5 meters to ensure comparability with the analytical derivation result, which assumes a height of 5 meters.

To address this issue, a non-design space needs to be constrained, with the associated mesh elements excluded from the topology optimization process. Specifically, a 0.2m x 5m rectangle was defined at the left boundary and set as a fixed region, as illustrated in Fig 4.3 (b).



(a) Without non-design space (b) 0.2*5m non-design space

Figure 4.3: The effect of defining non-design space, design domain box:1.6 * 5m

The results of topology optimization provide clear insights into the efficient utilization of materials within the structure. Fig 4.3 demonstrates that the core of the cross-section has zero density, indicating that these areas have less influence on the overall structural performance and can be removed without compromising the structural integrity.

4.2.2 Comparative results from analytical and numerical methods

The numerical method has a limitation in that the optimized shape is dependent on a particular load case. Specifically, when a uniformly distributed load q is applied in one single direction, causing one side to be in tension and the other side to be in compression, the topology optimization algorithm removes mesh based on the result from this specific load case, and results in asymmetric shape. In contrast, analytical derivation employing the concept of constant stress allows for a logical criterion: 'maximum tensile stress from load q in all cross-sections along the height + compressive stress from self-weight = constant.' This criterion gives a symmetric shape and ensures that the side in tension always remains constant regardless of the direction of the uniformly distributed load, which is the case in the real world.

Given the aforementioned limitation, the topology optimization algorithm is incapable of producing a symmetric shape based on the specified load case. Therefore, for a meaningful comparison, the analytical result for the second criterion presented in Sec 3.3 is considered, where the eccentricity of self-weight is utilized to balance the bending moment induced by the load q . Figure 4.4 depicts the optimized shapes obtained through analytical and numerical methods. Remarkably, the boundaries of these two shapes exhibit a striking similarity.

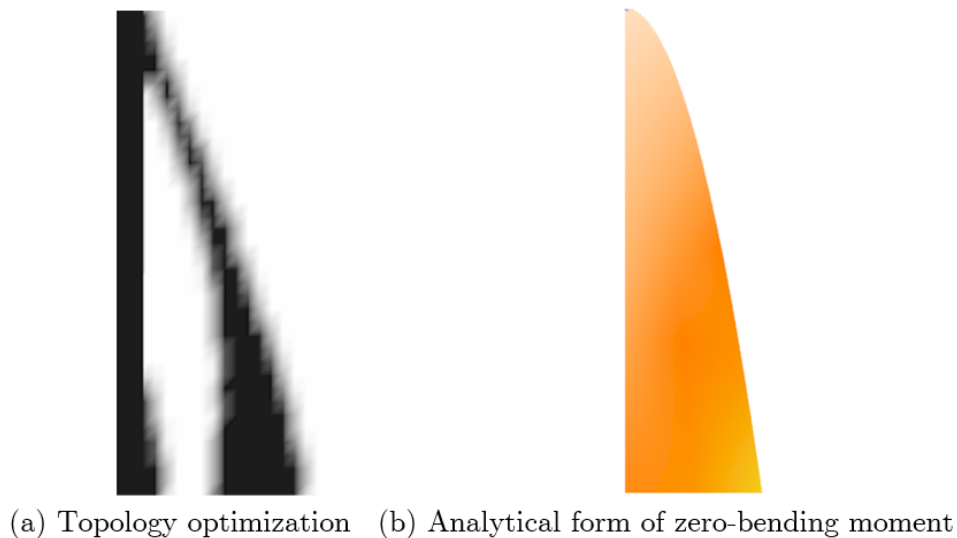


Figure 4.4: Comparison of numerical and analytical results from Sec 3.3.6

4.3 Shape optimization

Two main reasons drive the decision to perform shape optimization on the results of topology optimization. Firstly, it is crucial to avoid having a hollow core in the structure, as mass plays a critical role in providing effective sound insulation. While one approach is to fill the void with non-structural and more environmentally friendly material, another intriguing possibility is to conduct shape optimization assuming the use of a monolithic material, aiming to achieve the lightest possible weight while maintaining structural integrity.

Secondly, topology optimization often yields non-smooth skeletal structures that are impractical and challenging to manufacture. Therefore, it becomes necessary to employ a smoothing algorithm to refine and interpret the result, making it more feasible for practical implementation [52].

4.3.1 Shape optimization model setup

In Sec 2.2.1.2, three approaches for representing the boundary shape of structural elements were discussed. In this study, the chosen strategy involves utilizing a polynomial representation of the boundaries.

Polynomials have been extensively employed in shape optimization to represent boundaries, where the coefficients of the polynomial function serve as design variables [25]. To implement this approach, a C# code was developed within the Grasshopper environment. Two inputs are required for the code: p takes a list of points lying on the target curve as input, and d is the desired degree of the resulting polynomial function. As output, the code generates a function of y , denoted as $f(y)$, with the desired degree and its corresponding coefficients. Below is the Pseudo code representation:

Algorithm 1 Polynomial function approximation

```

Create empty lists  $x$  and  $y$ 
for each point in  $p$  do
    Add the  $x$ -coordinate of the point to list  $x$ 
    Add the  $y$ -coordinate of the point to list  $y$ 
end for
Sort the list  $y$  in ascending order while maintaining the corresponding order of elements in  $x$ 
Find the polynomial coefficients  $factors$  that best fit the data points  $(y, x)$  using the desired degree  $d$  and the QR method
Create an empty list  $elements$ 
for each coefficient in  $factors$  do
    Add a string element to list  $elements$  in the format  $coefficient * y^{index}$ 
end for

```

A polynomial function with a degree of at least 6 would be required to achieve a perfect fit of the curve, resulting in more than 7 coefficients. With the use of polynomials to represent the design space, the coefficients are the variables to optimize. However, optimizing such a large number of variables simultaneously is not efficient and hard to control.

In order to balance computational efficiency and accuracy, the degree of the polynomial function was set to 2, which provides a reasonable approximation of the numerical result. By reducing the degree and the number of coefficients to just three, it becomes more manageable to optimize the variables.

The three coefficients have distinct influences on the resulting curve. The coefficient for x^2 determines whether the curve is concave or convex, while the coefficient for x governs the starting angle of the curve. The constant term allows for horizontal shifting of the curve. By focusing on these three variables, it becomes clear how they individually affect the shape of the curve, simplifying the optimization process and saving significant computational time.

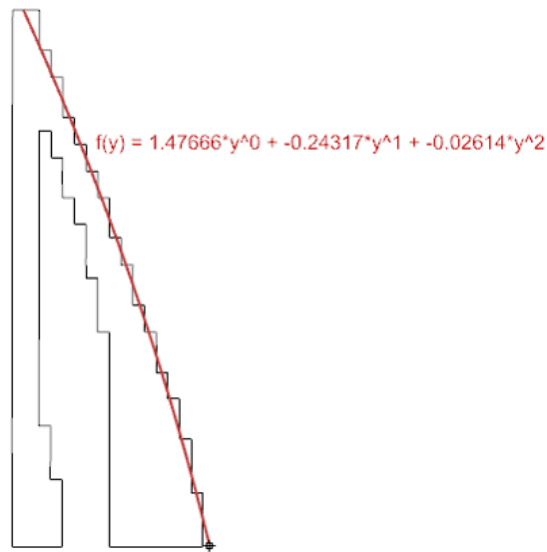


Figure 4.5: Polynomial approximation: coefficients as design variables

After defining the design variables, the structural performance of the design is evaluated using Karamba3D, a finite element analysis (FEA) tool. The boundary condition and load cases are the same as those in the previous sections. For shape optimization, the selected tool is Opossum, as discussed in Sec 2.2.3.1.

4.3.2 Penalty function

The objective of the optimization is to minimize the weight of the structure while ensuring that the maximum allowable tensile stress of the material is not exceeded. Since Opossum is a single objective optimization tool, it is necessary to incorporate the constraints into the objective or fitness function to guide the optimization process. This is achieved by using a penalty function, which allows the optimization algorithm to consider and enforce the satisfaction of the constraints.

In the context of optimization, constraints represent limitations or conditions that the solution must adhere to. These constraints can take the form of equality or inequality constraints. The penalty function assigns a penalty value based on the violation of each constraint, with the penalty value increasing as the

constraint violation becomes larger [53]. The objective function, which is the function to be minimized or maximized, is modified by adding the penalty term that accounts for the constraint violations. This modified objective function, incorporating the penalty term, is then optimized by the algorithm to find feasible solutions that satisfy the constraints.

By incorporating the penalty function into the objective or fitness function, the optimization algorithm is guided toward finding solutions that not only minimize the objective but also respect the specified constraints. This ensures that the optimized design meets the required performance criteria while considering the constraints imposed by the design problem.

The concept of the penalty function is mathematically defined based on the work of Thomas [54]. In Fig 4.6, the application of the penalty function is illustrated. The demonstrated list presenting stress values is shown on the left-hand side as input, which should be the maximum tensile stress that occurs in the structure.

The utilization, in this case, is calculated as the ratio between the tensile strength of the material ($0.13kN/m^3$) and the maximum tensile stress in the structure. It is desirable to have design solutions with utilization ranging from 0.6 to 0.8 as these values indicate an efficient use of the material. Therefore take this desired design space as the target utility that results in a value of 1, indicating no penalty. If the utilization falls below this range, it is considered an inefficient shape and is penalized by assigning a penalty value greater than 1. This penalty value serves to amplify the weight of the inefficient shape during the optimization process, discouraging its selection. Conversely, designs with maximum stress exceeding the maximum allowable stress in the structure should not be considered. These designs receive a higher penalty function than the inefficient range, effectively eliminating them from consideration in the optimization process.

	Maximum tensile stress (kN/cm ²)	Penalties
0	0	0
1	0.01	1
2	0.02	2
3	0.03	3
4	0.04	4
5	0.05	5
6	0.06	6
7	0.07	7
8	0.08	8
9	0.09	9
10	0.1	10
11	0.11	11
12	0.12	12
13	0.13	13
14	0.14	14
15	0.15	15
16	0.16	16
17	0.17	17
18	0.18	18
19	0.19	19
20	0.2	20

Less efficient space: with penalty

UC=0.6 : 0.078 kN/cm²

No penalty

UC=0.8 : 0.104 kN/cm²

Unacceptable design space

Figure 4.6: Demonstration of penalty function

Fig 4.5 illustrates the minimum weight result obtained using the previously mentioned penalty function. However, upon closer inspection, it is evident that the thinnest cross-section depth of 6.3 cm of this solution is not a feasible thickness for a noise barrier.

To address this issue, a second constraint was incorporated into the penalty function. This constraint should ensure that the thickness of the resulting shape remains within the acceptable range. By imposing this additional constraint, the optimization algorithm is guided toward finding solutions that not only minimize weight but also satisfy the thickness requirement.

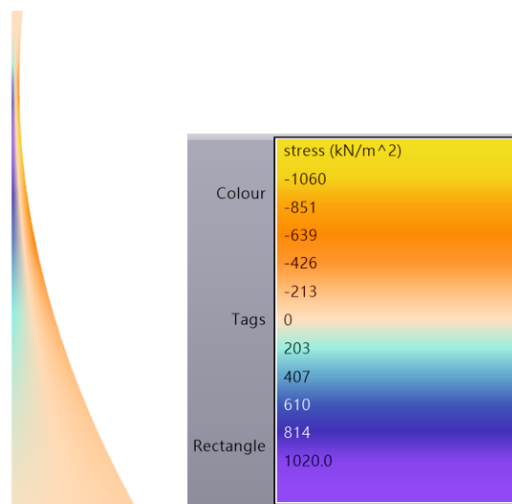


Figure 4.7: Infeasible result without thickness constraint, minimum thickness: 6.3 cm, weight: 3322.8 Kg

4.3.3.1 Asymmetric

Fig 4.4 demonstrates the similarity between the topology optimization result and the analytical result. In the analytical derivation, the criterion for achieving this asymmetric shape is to balance the bending moments caused by the uniformly distributed load and the eccentricity of self-weight, resulting in no bending moment and thus no tensile stress in the structure. To reproduce this geometry through numerical shape optimization, a target utility close to zero is desired, indicating a maximum tensile stress of zero in the structure.

This serves as the starting point to validate the accuracy of the numerical model. Fig 4.9 shows a comparison of the analytical and the numerical shape optimization results.

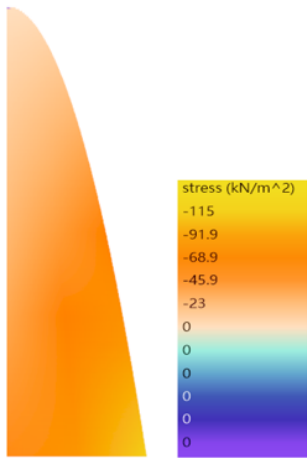
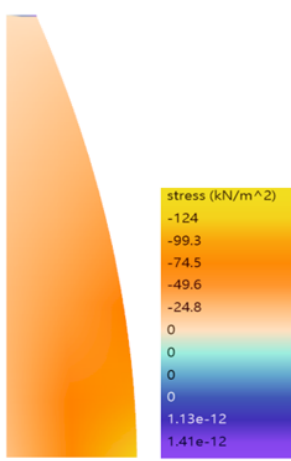
	Analytical derivation	Opossum optimization
		
Criterion	Zero bending moment	Target UC=0 (zero tensile stress)
Cross-sectional height expression	$\frac{2\sqrt{\gamma qy}}{\gamma}$	$1.014 - 0.013y - 0.046y^2$
Max stress (+) (kM/m^2)	0	0
Bottom depth (cm)	113.14	101.4
Weight (kg)	7569.94	7446.34

Figure 4.9: Comparison of analytical derivation (left) and shape optimization (right) results: Asymmetric

The solution obtained through analytical derivation exhibits a square root shape, while the numerical model represents the shape using a second-degree polynomial, resulting in a similar overall shape and the tensile stress in the structure is nearly zero. However, a slight deviation from the analytical solution is observed at the top boundary due to the imposed 20cm thickness constraint. Nevertheless, the bottom depth and weight have a high degree of similarity between the analytical and numerical results, confirming the accuracy of the numerical model.

The subsequent step involves examining the influence of various input values assigned to the target utility on the resulting geometry. This investigation enables a comprehensive understanding of how the shape progresses from a utility value of zero to one, shedding light on the dynamics of the optimization process.

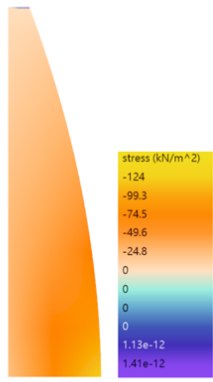
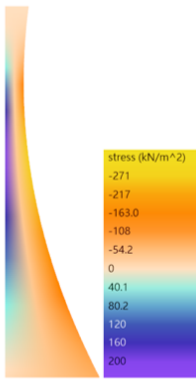
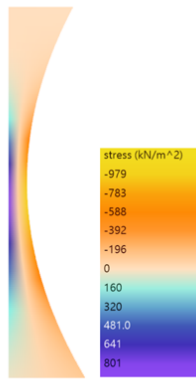
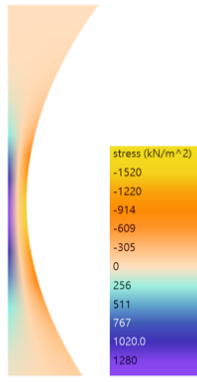
	Target UC=0 (no tensile stress)	Target UC=0.1-0.2 (130-260)	Target UC=0.6-0.8 (780-1040)	Target UC=1 (1300)
<u>Karamba</u>				
Max stress (+)	0	200.41	801.14	1277.53
Min thickness	22.60	20.06	20.04	20.01
Weight (kg)	7446.34	4219.05	3903.09	4318.95
Function a + by+ cy^2 a/b/c	1.014/-0.013/-0.046	1.016/-0.514/0.081	0.826/-0.594/0.141	0.801/-0.643/0.172

Table 4.1: Numerical shape optimization: Asymmetric shape

Once again, the results presented herein were obtained by optimizing for the least weight while considering the constraints related to utility and thickness. It can be observed that as the desired utility increases, the shape undergoes a transition from convex to concave. The highest tensile stress is concentrated in the middle of the tensile side; however, it does not achieve a uniform distribution of tensile stress across the entire height of the structure, which indicates a less efficient design. Moving from the second graph to the rightmost graph, the material is gradually removed from the bottom and added to the top. It is anticipated that with higher utility, the weight of the structure should decrease. However, the final shape exhibits a higher weight compared to the shape with a lower maximum tensile stress in it. This discrepancy may be attributed to the optimization algorithm introducing unnecessary material at the top in order to generate a higher bending moment that satisfies the utility constraint. Consequently, this geometry lacks practicality and loses its physical significance.

4.3.3.2 Symmetric

The content of this section is almost the same as the previous section, with the key difference being that the geometries presented here are symmetric. The first step is again to verify if the numerical model can produce results that align with the analytical solutions. In Sec 3.3.1, a symmetric shape with a constant zero tensile stress at the out-most fibre along the height was examined. To achieve this shape, the target utility is set to zero, indicating a maximum tensile stress of zero in the structure. The figure

below illustrates the comparison between the analytical solution and the numerical optimized results.

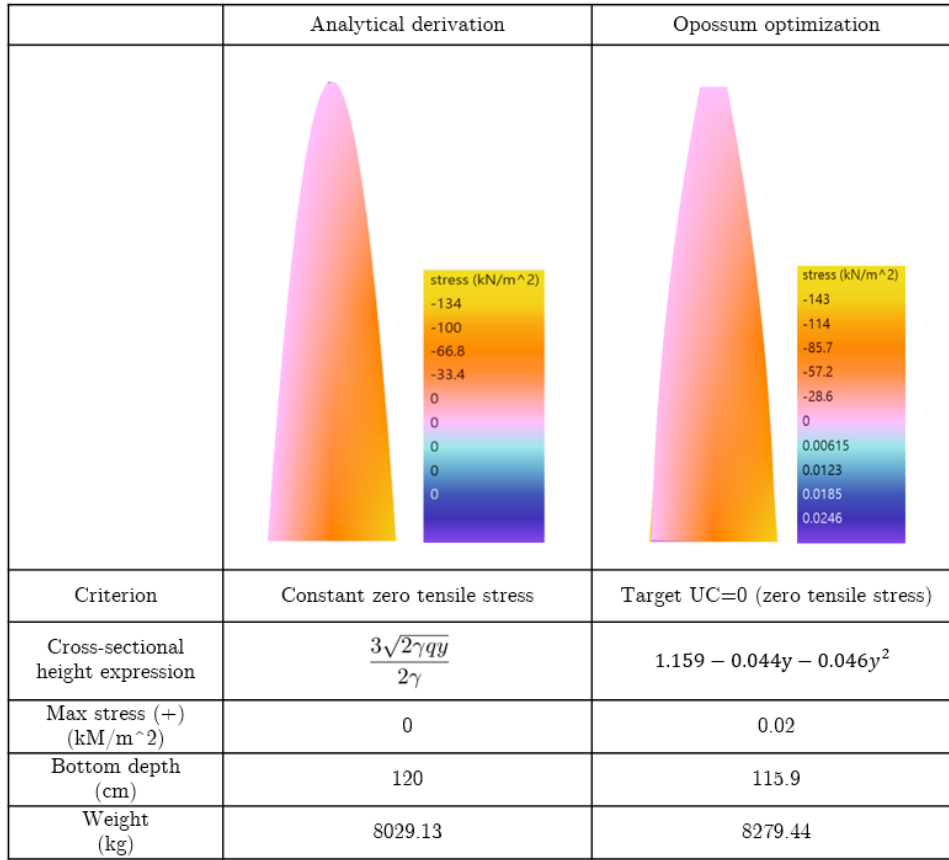


Figure 4.10: Comparison of analytical derivation (left) and shape optimization (right) results: Symmetric

The analytical derivation yields a square root-shaped solution, while the numerical model employs a second-degree polynomial to represent the shape, resulting in a similar overall shape and negligible tensile stress in the structure. The bottom depth and weight exhibit a high degree of similarity between the two results.

Another shape explored in the analytical derivation in Sec 3.3.3 is a geometry with constant tensile stress along the extreme fiber, equivalent to the material's tensile strength. To generate this geometry, the desired utility input should be set to one, indicating a maximum tensile stress equal to the material's tensile strength. It is important to note that there is no analytical solution to this equation, and thus the result was numerically approximated using the Matlab ODE113 method in Sec 3.3.3. The resulting geometry exhibits a triangular shape. Consequently, the second-degree polynomial is expected to have one degree lower, implying that the variable 'c' should be close to zero.

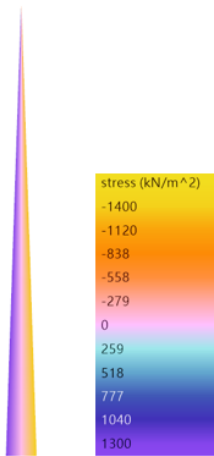
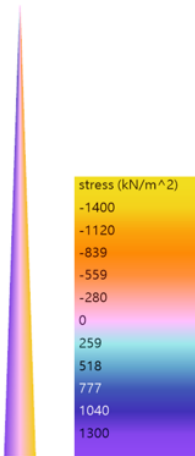
	Analytical derivation	Opossum optimization
		
Criterion	Constant tensile stress	Target UC=1 (1300 kN/m^2)
Cross-sectional height expression	Matlab ODE113 approximation	$0.267 - 0.065y$
Max stress (+) (kN/m^2)	1300	1300
Bottom depth (cm)	26.71	26.7
Weight (kg)	1349.81	1376.50

Figure 4.11: Comparison of analytical derivation (left) and shape optimization (right) results: Symmetric with constant stress

The numerical shape optimization indeed yields a linear shape represented by a linear function. All the values closely align with each other. The slight deviation observed can be attributed to the fact that the analytical result is not a perfect linear shape and is therefore lighter than the numerical result.

The following step is to explore the impact of different input values assigned to the target utility on the resulting symmetric geometry. This analysis will provide valuable insights into how the shape evolves as the desired utility value changes.

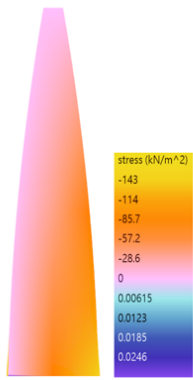
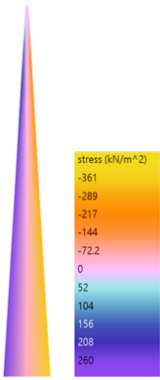
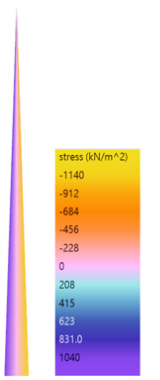
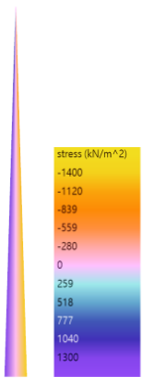
	Target UC=0 (no tensile stress)	Target UC=0.1-0.2 (130-260)	Target UC=0.6-0.8 (780-1040)	Target UC=1 (1300)
<u>Karamba</u>				
Max stress (+) (kN/m ²)	0.02	259.70	1038.3	1300
Bottom depth (cm)	115.9	55.5	29.7	26.7
Weight(kg)	8279.44	2883.80	1517.3	1376.5
Function a + by+ cy ² a/b/c	1.159/-0.044/-0.046	0.355/-0.126/-0.003	0.297/-0.073/0	0.267/-0.065/0

Table 4.2: Numerical shape optimization: Symmetric shape

Except for the first graph, the remaining three graphs all display linear results with a constant maximum allowable stress on the extreme fiber. These numerical results effectively support the "uniform strength theory" utilized in the analytical derivation. In numerical shape optimization, the primary objective is to minimize the weight of the structure while adhering to the stress constraint, which yields the exact same results as the constant stress geometry. From this, we can deduce that the uniform strength theory serves as a valuable criterion for generating structures that are both lightweight and efficient.

4.4 Discussion

In this section, we discuss the methodology and results of numerical structural optimization in two dimensions. Firstly, topology optimization was conducted to determine the optimal distribution of the material within a rectangular box subjected to self-weight and uniformly distributed load from one side. This step provides first insights into the optimal topology and allows us to analyze its similarities with the analytical derivation.

After obtaining the fundamental geometry from topology optimization, shape optimization was conducted to further refine the outcome and eliminate any hollow-core resulting from the previous topology optimization. The contour of the topology optimization result was then interpreted by a second-degree polynomial, which has three coefficients serving as design variables for shape optimization. The objective function of shape optimization is to minimize the weight of the cross-section with unit width while adhering to stress and thickness constraints for practicality. These constraints are implemented in the penalty function since Opossum is a single objective optimization plug-in in Grasshopper.

By setting different desired utilities for the structure, the optimization algorithm generates various minimum weight results accordingly, which can be compared to the analytical derivation to validate its correctness.

Topology optimization:

The first step in topology optimization involved validating the capability of the Karamba3D "BESO for Shells" component to include self-weight in the optimization process. The results obtained from Karamba exhibited a striking resemblance to the outcomes achieved by Huang, Xiaodong, and Xie, YM [9], confirming its effectiveness in handling self-weight considerations. However, it's worth noting that the results of topology optimization are highly sensitive to inputs, such as ER/ARmax/Rmin (as discussed in Sec 2.2.1.3). As a consequence, careful manipulation of these advanced inputs was necessary to obtain the expected outcomes.

Additionally, to ensure the meaningfulness of the results, we found it essential to restrict the non-design space in our research by fixing the desired height of the structure. This constraint was vital in preventing the algorithm from inadvertently removing the upper part of the wall, which could lead to an undesirable short wall that lacks practicality. By successfully managing these critical aspects during topology optimization, we laid a solid foundation for desired results.

Another noteworthy finding was the high similarity between the topology optimization result and one of the analytical results, which followed the criterion of having no bending moment in the structure. This criterion was achieved by balancing the bending moment resulting from the uniformly distributed load and the eccentricity of the geometry. The similarity between the two shapes is expectable, considering the limitation of topology optimization, which can only produce an asymmetric shape due to the assigned uniformly distributed load in a single direction. In real-world scenarios, loads may come from both sides, making the asymmetric shape impractical. In contrast, the analytical derivation employs the concept of constant stress on the loaded boundary in tension, resulting in a symmetric shape that ensures the boundary in tension remains constant regardless of the direction of the uniformly distributed load. As a result of the limitation of topology optimization, the optimized asymmetric geometry compensates for the bending moment from the external load by utilizing the bending moment from the eccentricity of self-weight, leading to a similar shape as the analytical solution.

Additionally, it is worth noting that although the bottom depth of the topology-optimized result is larger than the analytical solution, the weight is lighter. This is due to the algorithm removing the material at the core of the structure as it is considered inefficient. The advantage of this hollow structure lies in identifying the non-structural part, and the empty space can be filled with sustainable materials to provide sufficient sound insulation, allowing for significant structural material savings.

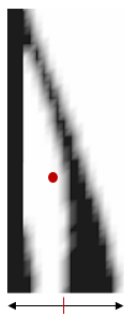
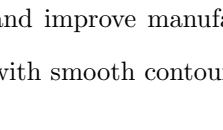
	Topology optimization	Analytical form of zero-bending moment
● : Centre of gravity		
Weight (kg)	5833.69	7446.34
Bottom depth (cm)	142.50	113.14

Figure 4.12: Topology optimization and analytical form of zero-bending moment

Shape optimization:

The decision to conduct shape optimization can be attributed to three main reasons:

Firstly, although topology optimization yields a significant advantage by saving structural material at the core of the hollow geometry, it may not always align with the practical choice of using monolithic material for the entire structure. In such cases, it becomes essential to restrict the zero density, which influences the optimal geometry without including a hollow part, to ensure the geometry remains practical.

Secondly, the results of topology optimization often exhibit a zig-zag boundary. To address this issue and improve manufacturability, it is necessary to find a way to interpret and represent the geometry with smooth contours.

Thirdly, to enable a valuable comparison between numerical methods and analytical derivations, it is crucial to generate a symmetric shape. As topology optimization inherently produces an asymmetric result, a second-degree polynomial is employed to approximate the density contour, and its three coefficients are treated as design variables for shape optimization. By doing so, we can achieve a symmetric shape that aligns with the analytical solution and facilitates a more meaningful comparison between the two methods.

In summary, shape optimization plays a critical role in refining the topology optimization results, improving manufacturability, and enabling valuable comparisons with analytical derivations.

The results of shape optimization demonstrate remarkable similarities to the analytical solutions, as

evident from Fig 4.9, 4.10, and 4.11. The slight discrepancies observed could be attributed to the limitations of the second-order polynomial used in the approximation. As the degree of the polynomial increases, which also means more design variables, the polynomial expressions become more similar to the analytical solutions. Nevertheless, considering the trade-off between computational efficiency and accuracy, the three design variables utilized in the optimization process suffice to achieve favorable outcomes.

Another important factor influencing the results is the penalty function employed in the optimization process. Deviations observed in the numerical optimized results are primarily due to the constraints imposed in the penalty function, particularly the 20-centimeter constraint. In setting up the penalty function, it is advisable to assign higher penalties to unacceptable design spaces compared to inefficient design spaces, promoting faster convergence as the algorithm avoids such regions. Additionally, the square root method, Eq 4.1, for combining two constraints proves to be effective, leading to desired results.

It is noteworthy that the right three graphs in Fig 4.1 were not covered in the analytical part. These shapes fail to satisfy the criterion of uniform strength theory on the loaded boundary, which implies that the analytical solutions for these shapes do not exist. Furthermore, as the desired utility increases, allowing higher tensile stress in the structure, it is observed that the weight of the optimal shape does not decrease, indicating that these results are neither efficient nor practical in achieving uniform strength theory.

In conclusion, Opossum emerges as a robust tool for optimization, producing results comparable to analytical derivations. Despite the different criteria utilized by the two methods—constant maximum tensile stress for analytical derivation and minimum weight geometry with stress constraints for shape optimization—, they yield similar outcomes. It is worth noting that no closed-form solution existed in analytical derivation for "constant maximum tensile stress under self-weight and uniformly distributed load," leading to numerical approximation using Matlab's non-linear differential solver ODE113. The impressive performance of Opossum in achieving nearly identical results underscores its efficacy in numerical optimization.

Chapter 5

Numerical structural optimization-3D

The previous sections focus on two-dimensional cross-sections, while The third part of the research delves into the three-dimensional optimization of the structure. The optimizations primarily target two aspects: the corrugated shape in the longitudinal direction and the cross-sectional area along the noise barrier, varying in both the longitudinal and vertical directions.

In the first section, five variables are introduced to control the longitudinal shape of the noise barrier. These variables play a crucial role in determining the specific corrugated configuration.

The second section focuses on another set of two variables that dictate the assignment of the cross-section along the longitudinal direction of the noise barrier.

Subsequently, the setup for finite element analysis (FEA) using Karamba is presented. This step is crucial for evaluating structural performance and obtaining accurate results during the optimization process.

Finally, the optimization process is carried out using Opossum, where seven design variables are manipulated to attain the minimum weight. The resulting outcomes are subsequently discussed and analyzed.

5.1 Longitudinal direction-3 types of corrugations

The design of the longitudinal shape of the noise barrier takes inspiration from various types of corrugated sheets commonly found in roof structures, floors in railway vehicles or bridges, and the aircraft industry [55]. These corrugated shapes are well-known for their ability to enhance bending stiffness and increase buckling loads in structures, making them particularly intriguing for the current research. The objective

is to leverage the unique stiffening effects offered by these special shapes and incorporate them into the design of the noise barrier.

Three fundamental types of corrugation have been identified as the base shapes, which will then be combined using an interpolation function to create the final longitudinal profile. The interpolation weights assigned to each shape determine their respective contributions and importance in the overall design. Through the optimization process, it becomes evident that the corrugation with a higher weight demonstrates superior structural performance. The five design variables in total encompass both the geometric properties of the shapes and the interpolation process, allowing for comprehensive control over the longitudinal shape.

5.1.1 Individual design variables for each type of corrugations

Three main types of corrugated shapes construct the longitudinal shape of the noise barrier. The first type consists of circular shapes formed by two arcs within one cycle. These shapes are controlled by two design variables: the angle t and the radius R of the circle. The first row in Fig 5.1 illustrates this type of shape.

The second type of shape is trapezoidal, as shown in the second row in Fig 5.1. It requires three variables to control its geometry: the angle θ , half the height h , and half the length l of one cycle.

The third type is the sinusoidal shape, commonly used in corrugated cardboard. It follows the general equation $y = a * \sin(b * x)$, where a controls the amplitude and b controls the frequency of the sinusoidal curve. This shape provides a smooth undulating pattern.

The following top view illustrations depict the longitudinal corrugated shapes:

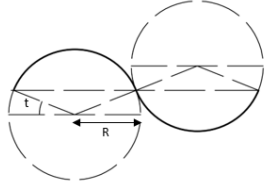
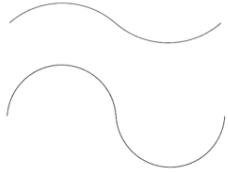
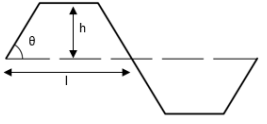
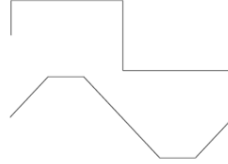
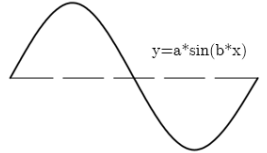
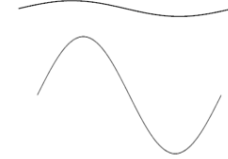
	Corrugated shape	Design variables	Possibilities
Circular		t: start angle R: radius	
Trapezoidal		theta: start angle h: height l: half the length of one cycle	
Sinusoidal		a: amplitude b: frequency	

Table 5.1: Three corrugated shapes and variables

By combining and interpolating these three types of shapes, the final longitudinal shape of the noise barrier can be obtained. The interpolation weights of each type determine their contributions to the overall design.

5.1.2 Combine and reduce the number of variables

In the previous section, each of the three corrugated shapes has its own set of variables to control the generation of individual waves. However, it is possible to reduce the number of variables by identifying the relationships between certain parameters.

The height and length of a single cycle can be controlled by two independent variables for all three types of shapes. The main reason for doing this is to ensure that the three corrugations can be effectively combined using the interpolation function to create the final geometry. To achieve this, it is crucial to maintain consistency in the scale of the shapes. Specifically, the height and length of all three shapes should remain the same but retain their corrugation characteristics when manipulating the input to the design variables.

For the circular shapes, the parameters R and t are chosen to serve as independent variables governing the height and length of the shapes. In the case of trapezoidal shapes, the height h and half-length l depend on both R and t . The relationships between these variables can be seen in the figure below:

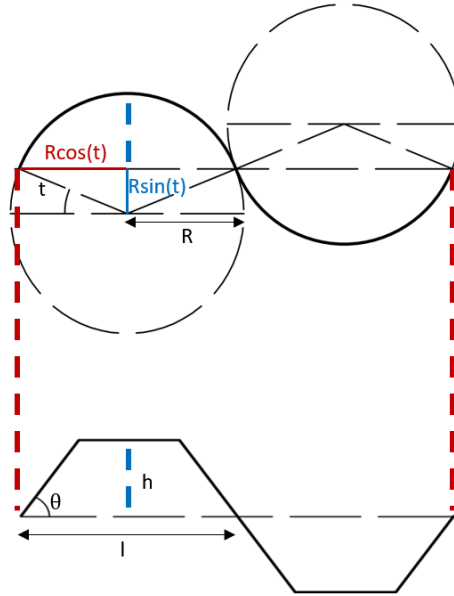


Figure 5.1: Relationships of variables: circular and trapezoidal shape

$$\text{Length:} \quad 4R \cos(t) = 2l, \quad l = 2R \cos(t) \quad (5.1a)$$

$$\text{Height:} \quad R - R \sin(t) = h \quad (5.1b)$$

Similarly, the parameters a and b used in sinusoidal shapes also depend on R and t . The relationships between these variables are shown in Fig:

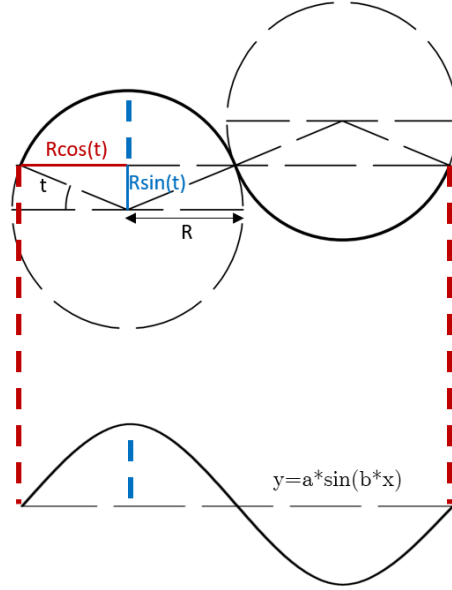


Figure 5.2: Relationships of variables: circular and sinusoidal shape

$$\text{Length:} \quad 4R \cos(t) = \frac{2\pi}{b}, \quad b = \frac{2\pi}{4R \cos(t)} \quad (5.2a)$$

$$\text{Height:} \quad R - R \sin(t) = a \quad (5.2b)$$

It is important to note that there is still one independent variable to control the start angle of the trapezoidal shapes, which is unrelated to the R and t parameters.

Reducing the number of variables provides several advantages. Firstly, it significantly reduces computational time and power requirements, making the optimization process more efficient. Additionally, this step ensures that the three shapes have consistent dimensions, specifically the same length and height in one cycle. This is crucial for interpolation between the shapes. If the initial seven parameters are all independent and result in the three corrugations having different sizes, the interpolation would not be meaningful.

5.1.3 Interpolation function

The interpolation function plays a crucial role in determining the respective contribution of each shape. By assigning weights to the three types of corrugation, the interpolation function allows for a combination of their characteristics to achieve an optimal design solution. The choice of weights becomes particularly important as it determines the relative importance of each shape and can significantly in-

fluence final structural performance. The weights for each shape are S1 (circular), S2 (trapezoidal), and S3(sinusoidal). Inside the triangle shown in Fig 5.3 is the design space of interpolation weights, which have the following relationship [56]:

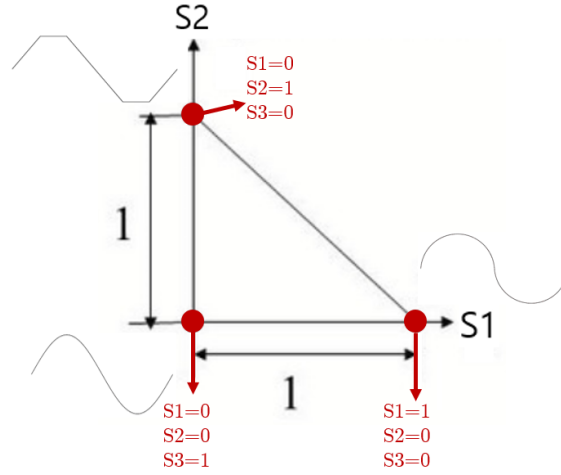


Figure 5.3: Interpolation function

$$0 \leq S1 \leq 1 \tag{5.3a}$$

$$0 \leq S2 \leq 1 \cap S2 \leq 1 - S1 \tag{5.3b}$$

$$S3 = 1 - S1 - S2 \tag{5.3c}$$

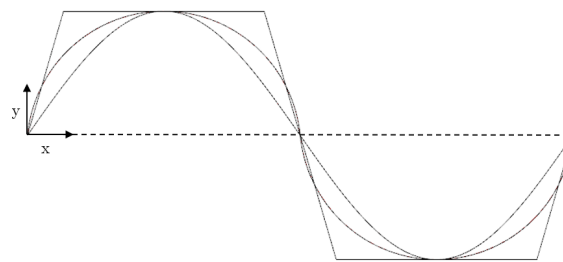


Figure 5.4: Three types of corrugated shape with the same scale

The final shape is the weighted results of three corrugations:

$$y_f = y_1 * S1 + y_2 * S2 + y_3 * S3 \tag{5.4}$$

where : y_f = y value of the final weighted shape

y_1 = y value of the circular corrugation

y_2 = y value of the trapezoidal corrugation

y_3 = y value of the sinusoidal corrugation

Setting design variables to control the weights of the three shapes offers several advantages. Firstly, it provides flexibility in adjusting the contribution of each shape to the overall design. By manipulating the weights, it becomes possible to explore and understand the structural properties of the shapes, like bending stiffness in this case. Additionally, the use of variable weights allows for a more nuanced exploration of the design space in one model. This enables a fine-tuning of the design to meet specific performance requirements or constraints. In conclusion, this approach provides greater control and flexibility in achieving an optimal design solution that meets the desired structural performance requirements.

5.2 Cross-section assignment

After determining the longitudinal curve, another key aspect of defining the geometry of the noise barrier is the assignment of cross-sections. These cross-sections not only vary along the longitudinal direction but also across the height of the wall. The process of assigning cross-sections involves two steps of interpolation.

Firstly, five control points are selected along the longitudinal curve. The cross-sections assigned to these control points are obtained through interpolation between two symmetric shapes derived in Sec 4.3.3.2. Subsequently, a linear interpolation is performed between these control points to determine the cross-sections along the longitudinal curve.

The two chosen base shapes for interpolation are the optimized results with desired utilities of 0 and 0.2, as depicted in the first two graphs of Fig 4.2. These two shapes represent extreme weights, and the interpolation function enables the calculation of intermediate weights. The optimization algorithm gradually reduces the cross-sectional area at the control points with lower stress levels, aiming to achieve the lightest possible result.

5.2.1 Interpolation of two shapes

Five control points have been strategically placed along the longitudinal curve, as shown in Fig 5.5. The red dots denoted as "A" are positioned along the center-line of the curve, while the blue dots, denoted as "B", are located at the extremities of the curve. All the red dots are assigned the same cross-section, while all the blue dots are assigned a different cross-section. As the application of a uniformly

distributed load is on one side in the numerical model, consequently, the blue dot at the crest and the trough experience different stresses, leading to the optimization of distinct cross-sections. However, it is important to note that in real-world scenarios, where loads may be applied from both sides, maintaining symmetry is essential, resulting in the same cross-section being assigned to the two extreme blue spots.

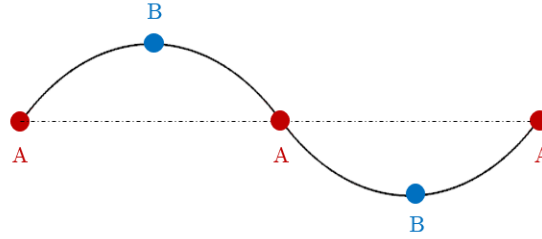


Figure 5.5: Five control points on the longitudinal curve

The cross-sections assigned to the control points are derived through interpolation of two base shapes obtained from the previous 2D optimization in Sec 4.3.3.2. These base shapes represent the optimized minimum weight results under constraint utilities of 0 and 0.2. In the 3D model, the cross-section corresponding to a utility of 0 (referred to as 'shape 1') represents the largest area, while the cross-section with utility 0.2 (referred to as 'shape 2') represents the minimum cross-sectional area that can be assigned to the control points.

	Target UC=0 (no tensile stress) Shape 1	Target UC=0.1-0.2 (130-260) Shape 2
Karamba		
Function $a + by + cy^2$ a/b/c	1.159/-0.044/-0.046	0.555/-0.126/-0.003

Figure 5.6: First two graph taken from Fig4.2, referred to as Shape 1 and Shape 2

With the interpolation function, it becomes feasible to generate intermediate shapes between Shape 1 and Shape 2. Specifically, the resulting three coefficients of the second-degree polynomials lie within the range

of the three coefficients corresponding to Shape 1 and Shape 2. This allows for the creation of a smooth transition between the two base shapes, providing greater flexibility in designing the overall geometry. In Fig 5.7, index 1 corresponds to Shape 1, index 2 corresponds to Shape 2, and N represents the interpolation weight. The interpolation weight N varies from 0 to 1, resulting in a continuous spectrum of intermediate geometries. Here, two more design variables are added to control the interpolation weight of cross-sections at point A and point B.

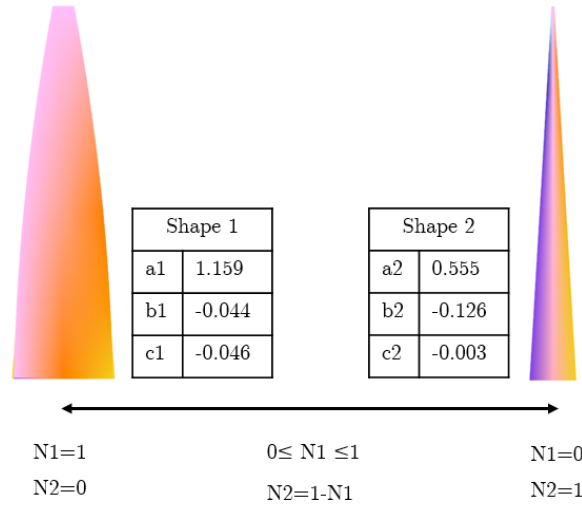


Figure 5.7: Interpolation of two base cross-sections

The weighted coefficients of the polynomial $a + by + cy^2$ can be calculated using the following equations 5.5. Let's take point A as an example, and use the lower index A to represent the weight and resulting coefficients at point A.

$$a_A = a1 * N1_A + a2 * N2_A \quad (5.5a)$$

$$b_A = b1 * N1_A + b2 * N2_A \quad (5.5b)$$

$$c_A = c1 * N1_A + c2 * N2_A \quad (5.5c)$$

The main goal is to find an optimized longitudinal corrugated profile that results in the lowest possible interpolation weight of Shape 1 assigned to the control points. This approach allows us to achieve a geometry with the minimum weight and thinner cross-sections, leading to a more efficient design.

5.2.2 Linear interpolation between control points

After assigning the weighted results of cross-sections at the five control points, the next step involves creating the cross-sections along the longitudinal curve between two consecutive control points, using the

linear interpolation technique to ensure a smooth transition. With this, the design of the longitudinal corrugated shape and the cross-section assignment is completed in one cycle. To effectively compare the weight of all the candidates, which may have different lengths of one cycle, the complete cycle is repeated until it reaches a length of ten meters. The figure below illustrates an example of the linear interpolation technique.

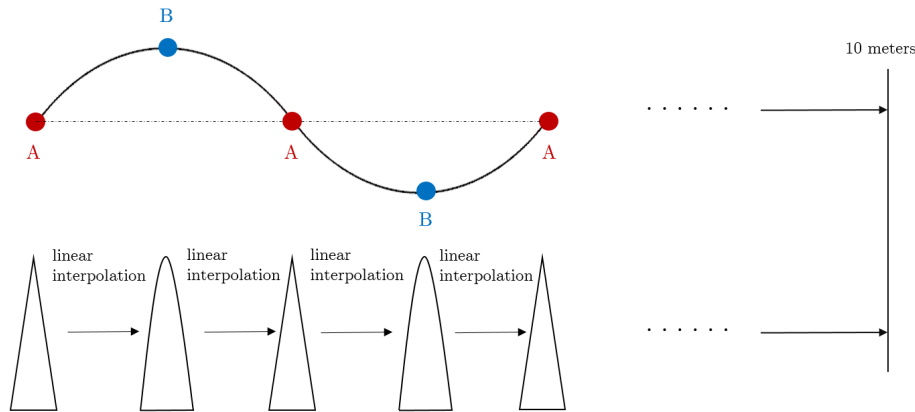


Figure 5.8: Example of the linear interpolation

5.3 Structural optimization

The previous section discussed how the design variables were defined to generate the geometry, and this section focuses on evaluating the structural performance of the design using Karamba3D, a finite element analysis (FEA) tool. The objective function remains the same as in the 2D cross-section optimization, which is to minimize weight while adhering to stress constraints, and the penalty function logic remains unchanged. As mentioned, there are seven design variables in total. Three of them generate the three different corrugated shapes, two of them control the interpolation weight of each corrugation, and the other two control the interpolation weight of the two base cross-sections.

The main difference in this part is: The previous part focus on two-dimensional cross sections, as a result, the support condition at the bottom needs to be moment fixed to resist bending moment from uniformly distributed load. On the other hand, when the model extends to three dimensions, the purpose of optimizing the longitudinal shape aims to find the shape that can provide enough bending capacity when the structure works as a whole. Accordingly, the rotational freedom at the bottom should be released to generate a shape that can provide enough bending stiffness itself.

The main distinction in this section lies in the focus on three-dimensional geometry. In the previous part, the emphasis was on two-dimensional cross-sections, which necessitated fixing the support condition at the bottom to resist bending moments from the uniformly distributed load. However, in the current

three-dimensional model, the optimization of the longitudinal shape aims to discover a configuration that can offer sufficient bending capacity when the structure functions as a whole. Consequently, the rotational freedom at the bottom is released to generate the optimal longitudinal shape capable of providing adequate bending stiffness on its own with the least material.

Ultimately, the interpolation weight of the three corrugated shapes is expected to offer valuable insights into which corrugation yields superior structural performance, as it holds a greater significance in the optimal solution. Additionally, the optimized longitudinal shape is expected to yield the lowest interpolation weight of the larger cross-section, Shape 1, assigned to the control points, Thus contributing to achieving the minimum weight for the final geometry.

5.3.1 FEA

To conduct finite element analysis, the geometry model was transformed into a structural model using the "MeshToShell"-component in Karamba3D. This process converts the mesh into TRIC element, which is a 3-node shear-deformable isotropic flat shell element developed by Argyris et al [57]. The TRIC element has 6 rigid-body and 12 straining modes of deformation, allowing it to capture axial straining, symmetrical and antisymmetrical bending, and transverse shearing. Notably, the element exhibits fast convergence properties.

The "MeshToShell" component takes into account the thickness of each mesh and the material properties as input. In this case, the mesh size is set to 0.1×0.2 m, and the material used is concrete C20/25, consistent with the material selection in the 2D optimization and analytical derivation for comparison purposes.

Regarding boundary conditions, the model simulates an infinitely long wall. Hence, the left and right ends are constrained in the longitudinal direction (x-axis). The bottom support is hinged support with fixed displacements in the x, y, and z directions, while the rotational degrees of freedom are released to allow the optimization algorithm to generate a geometry with sufficient bending stiffness to withstand the loads.

The loads applied include the self-weight of the noise barrier and a uniformly distributed load acting on the wall's surface. In the previous two-dimensional models, the uniformly distributed load q was represented as a $2kN/m$ line load along the centerline of a unit-width cross-section. For the current three-dimensional model, the load is equivalent to a $2kN/m^2$ surface load applied on the mesh's surface. The structural model's configuration can be observed in Fig 5.9.

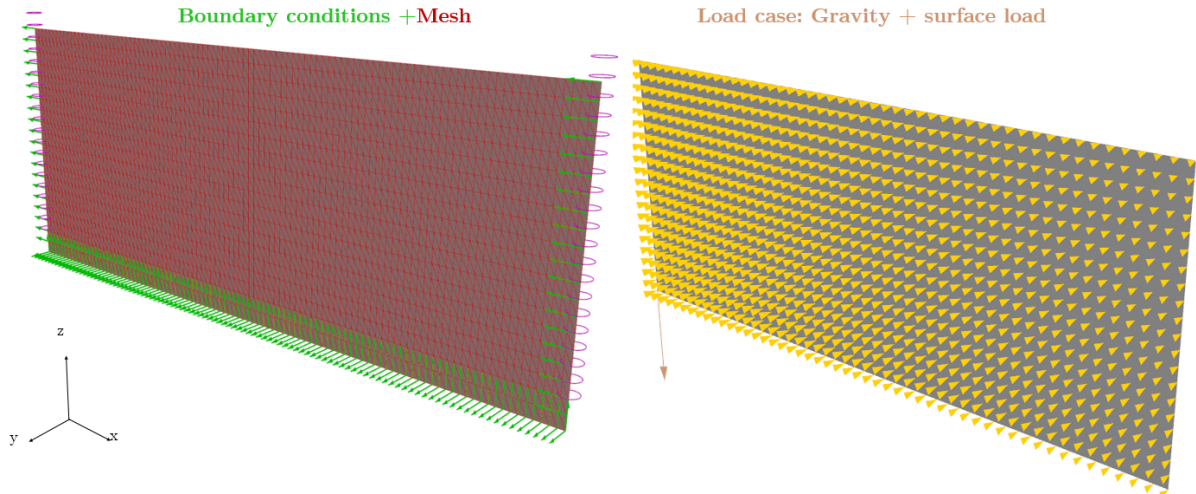


Figure 5.9: Boundary conditions and load case of the structural model

The "ShellView" component is used to visualize the results of the structural analysis. It displays the cross-section of the shell with thickness variations along the longitudinal direction and the height of the wall.

The thickness of the shell may consist of different layers subjected to either tensile or compressive stress. Each layer is identified by an "Index of Layer," with zero spanning the entire cross-section thickness. The "Position of results" ranges from -1 to 1, corresponding to the lower boundary and the upper boundary of the current layer. It is important to note that the local coordinate system might be arbitrary, so the orientations need to be checked beforehand. In this case, the local z-axis points to the upper boundary.

The specific result of interest is the maximum tensile stress occurring in the structure. To obtain this information, we should examine the first principal stress (tensile) at position 1, which represents the upper boundary loaded in tension. This analysis allows us to evaluate the structural performance and identify critical areas of the design, and optimize the geometry based on this value.

5.3.2 Optimization and results

The approach for conducting structural optimization in three dimensions is similar to the two-dimensional method. The primary objective remains the minimization of the structure's weight while ensuring that the maximum allowable tensile stress of the material is not exceeded. To achieve this, the Opossum optimization tool is employed once again. Given that Opossum is a single-objective optimization tool, the stress constraint is incorporated into the objective function using a penalty function, guiding the optimization process effectively. Further details on the definition of the penalty function can be found in Sec 4.3.2.

Within the 3D model, there exist seven design variables that can be manipulated to attain the optimal

geometry. Among these variables, three control the generation of three different corrugated shapes in the longitudinal direction, while two regulate the interpolation weight of each corrugation to produce the combined shape with weighted contributions. Additionally, the other two variables govern the interpolation weight of the two base cross-sections. A visual representation of these seven design variables can be seen in Fig 5.10.

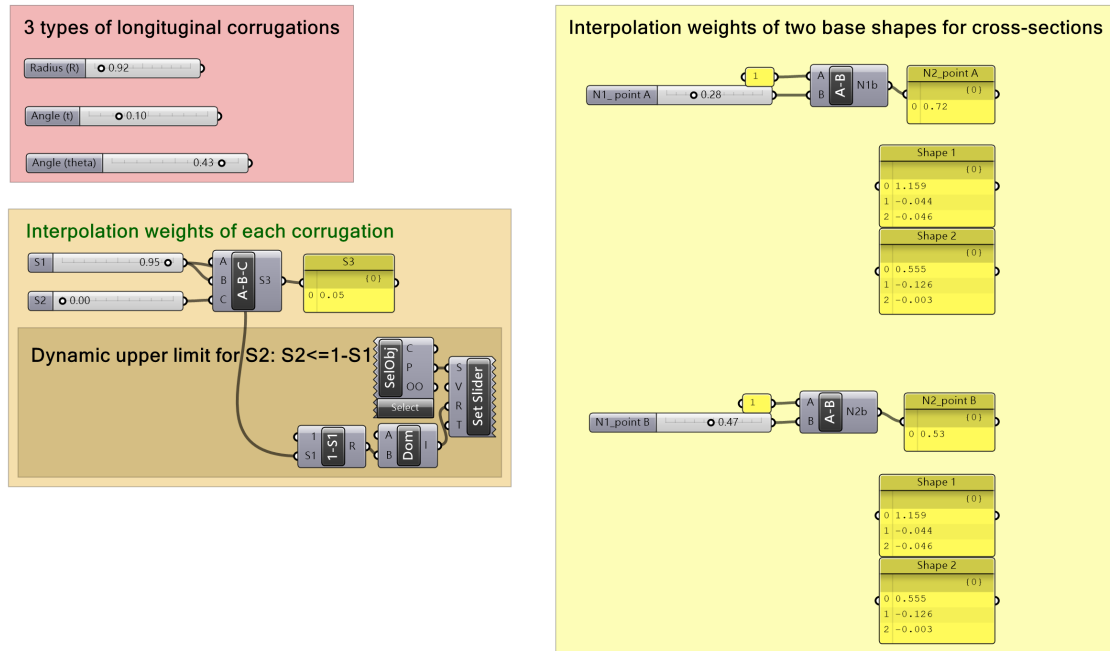


Figure 5.10: Seven design variables in the 3D model

5.3.2.1 Optimization results: $UC=0$

In the first practice, the optimization algorithm minimizes the weight of the geometry while targeting a desired utility of zero, which implies that the maximum value obtained from the first principal stress at the upper boundary should ideally be zero. The details of the longitudinal profile can be observed in Figure 5.2, and the cross-sections assigned at control points A and B are depicted in Figure 5.3. The total numbers of design variables are ten in both figures, however, $S3$, $N2_A$, and $N2_B$ are not independent variables as the sum of the interpolate weight should always be one. As a result, only seven variables are needed to be optimized.

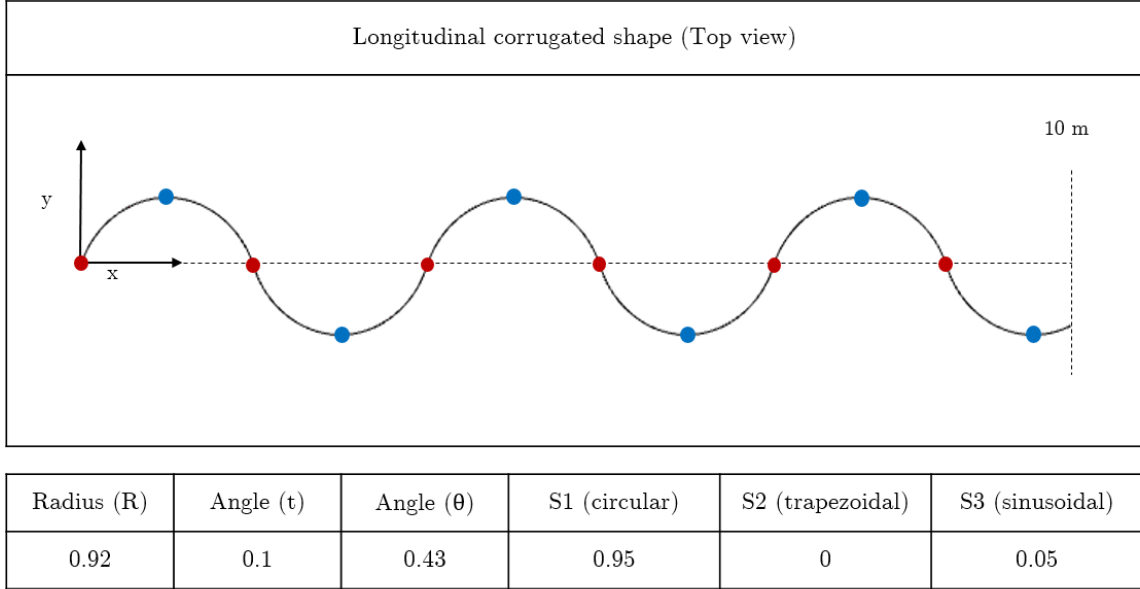


Table 5.2: Optimized design variables for longitudinal profile, UC=0

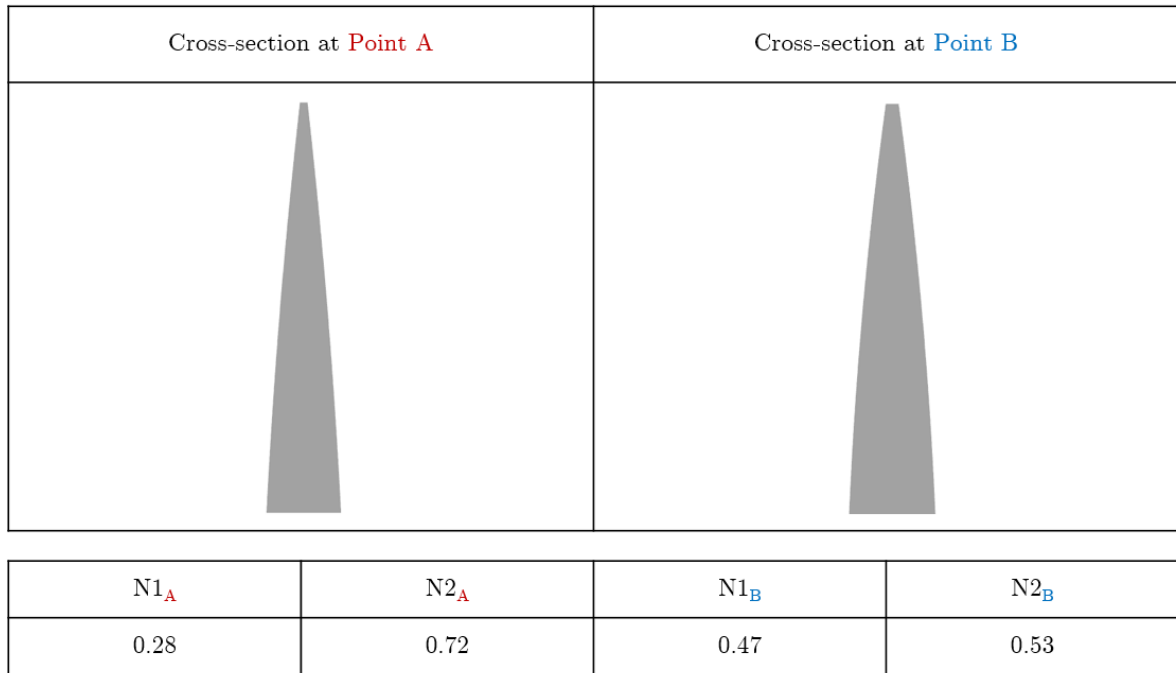


Table 5.3: Optimized design variables for cross-sections at control points A and B, UC=0

The circular corrugated shape exerts significant dominance over the longitudinal profile with an interpolation weight of 0.95, while the trapezoidal shape has no contribution to the results, and the sinusoidal shape has a minor influence with an interpolation weight of 0.05. Since the trapezoidal shape does not impact the final geometry, the third variable, Angle θ , becomes irrelevant. On the other hand, the second design variable, Angle t , is set to 0.1, equivalent to 18 degrees as the start angle of the arc.

Regarding the cross-section, Fig 5.6 has illustrated that Shape 1 boasts the largest area, while Shape 2 has the smallest area. The interpolation function effectively creates intermediate cross-sectional areas between these two extremes. Point A, positioned along the centerline of the profile, is subjected to lower loads and necessitates a thinner cross-section. The optimized results reveal an interpolation weight of 0.28 for Shape 1 and 0.72 for Shape 2 at point A. In contrast, point B, located at the extreme position of the longitudinal profile and experiencing higher loads, yields corresponding interpolation weights of 0.47 for Shape 1 and 0.53 for Shape 2. Consequently, Shape 2 has a higher interpolation weight at point A, and generates a cross-section smaller than the one assigned at point B.

The figure below provides a clearer illustration of the optimized geometry with the utility constraint set to zero. The top view offers insights into the linear interpolation of the cross-sections between the control points located at the wave crest and wave through. This arrangement ensures a smooth transition of the varying cross-sections along the longitudinal profile.

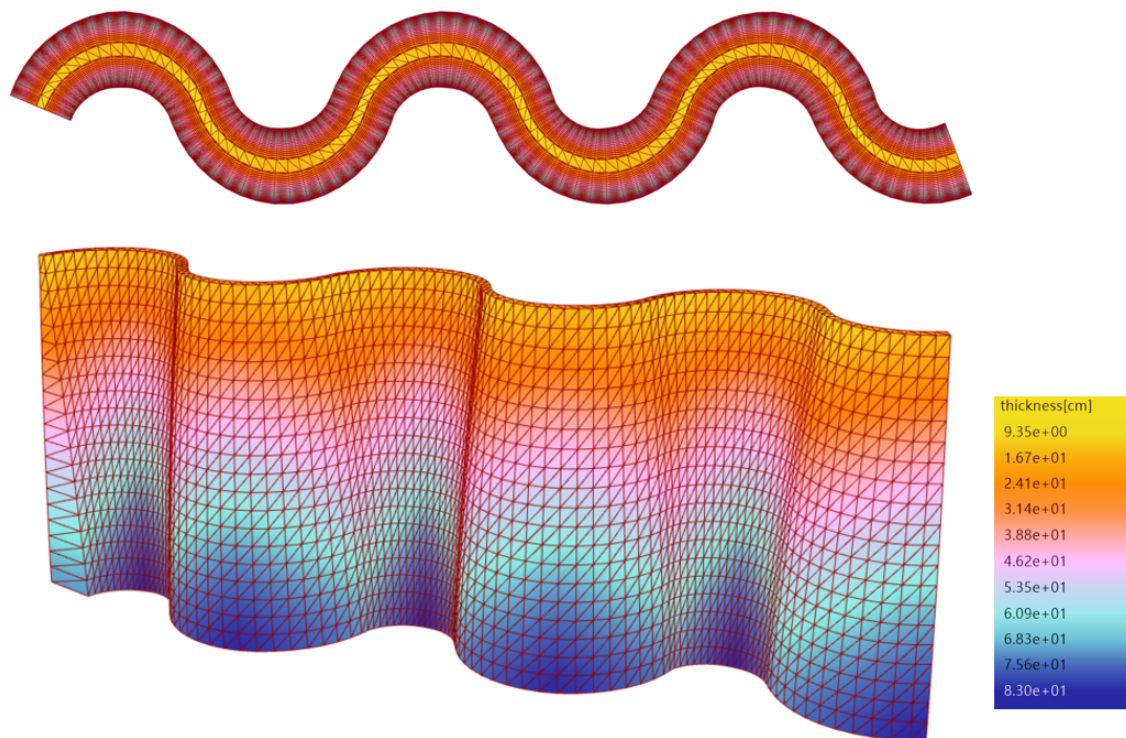


Figure 5.11: Illustration of optimized geometry with $UC=0$, top view and perspective view

Finally, the first principal stress at position 1, representing the upper boundary subjected to tension, is demonstrated below. Note that the right and left boundaries experience extremely high stress, and as a result, the right-most and left-most parts are not visualized, and the tensile stress in these areas is not taken into account. The model is designed to simulate an infinitely long wall; thus, ideally, each cycle should have the same stress results or at least be identical.

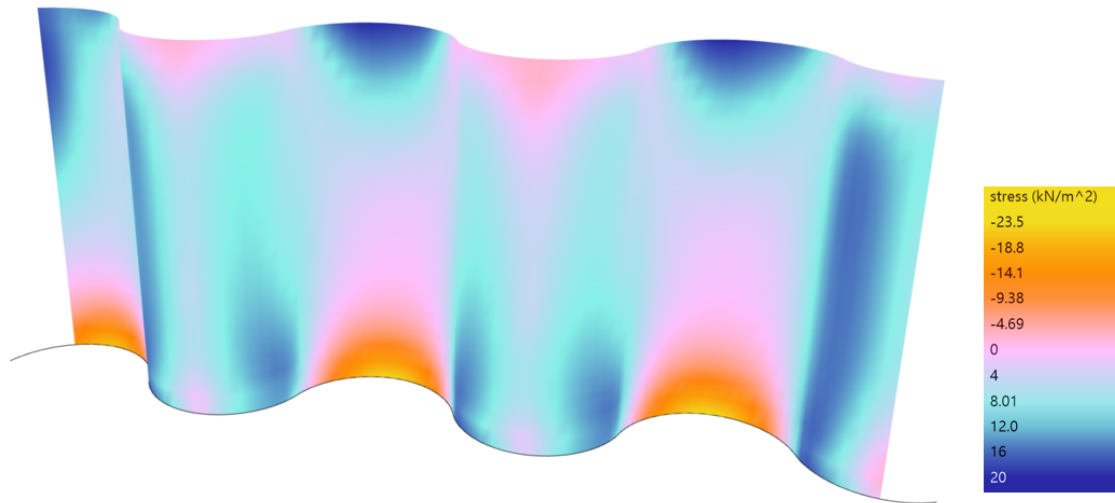


Figure 5.12: First principal stress in the upper boundary layer, UC=0

The maximum tensile stress that occurs in the structure is 20 kN/m^2 , which is close to the target of zero utility. The length of the longitudinal curve is 13.07 meters, and the total weight of the structure is 63949 kg. Therefore, the weight per meter is 4892.8 kg/m. However, since the length of this noise barrier is intended to cover 10 meters, it is more meaningful to divide the total weight by 10m, resulting in 6394.9 kg per meter.

5.3.2.2 Optimization results: UC=0.2

In the second practice, the optimization algorithm minimizes the weight of the geometry with a desired utility of 0.2, which implies that the maximum value obtained from the first principal stress at the upper boundary should ideally be 260 kN/m^2 . The details of the longitudinal profile can be observed in Figure 5.4, and the cross-sections assigned at control points A and B are depicted in Figure 5.5.

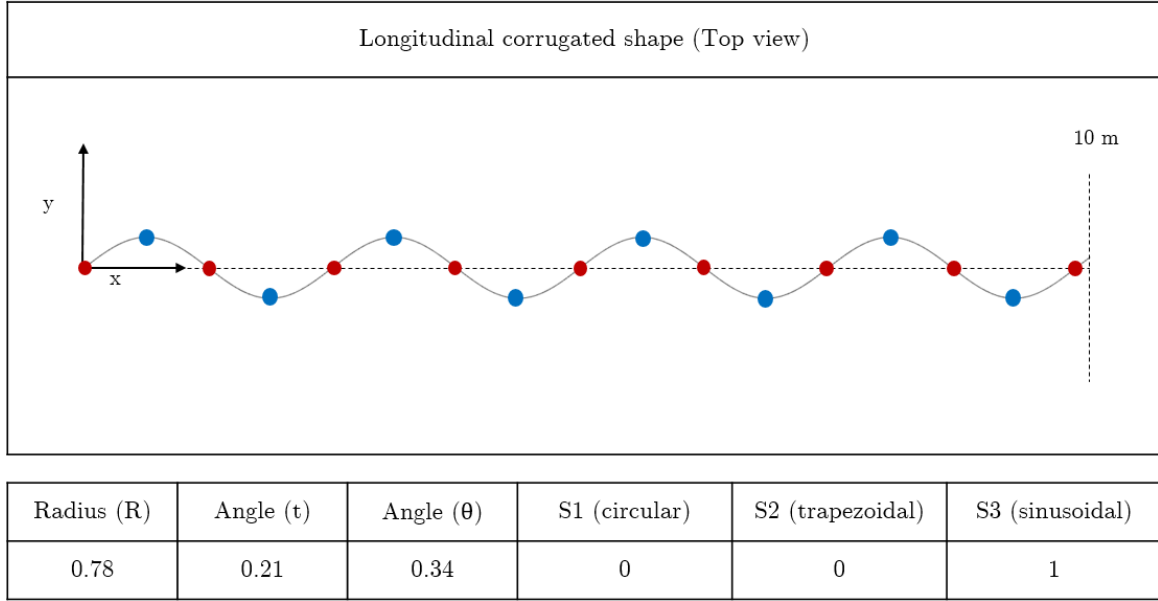


Table 5.4: Optimized design variables for longitudinal profile, UC=0.2

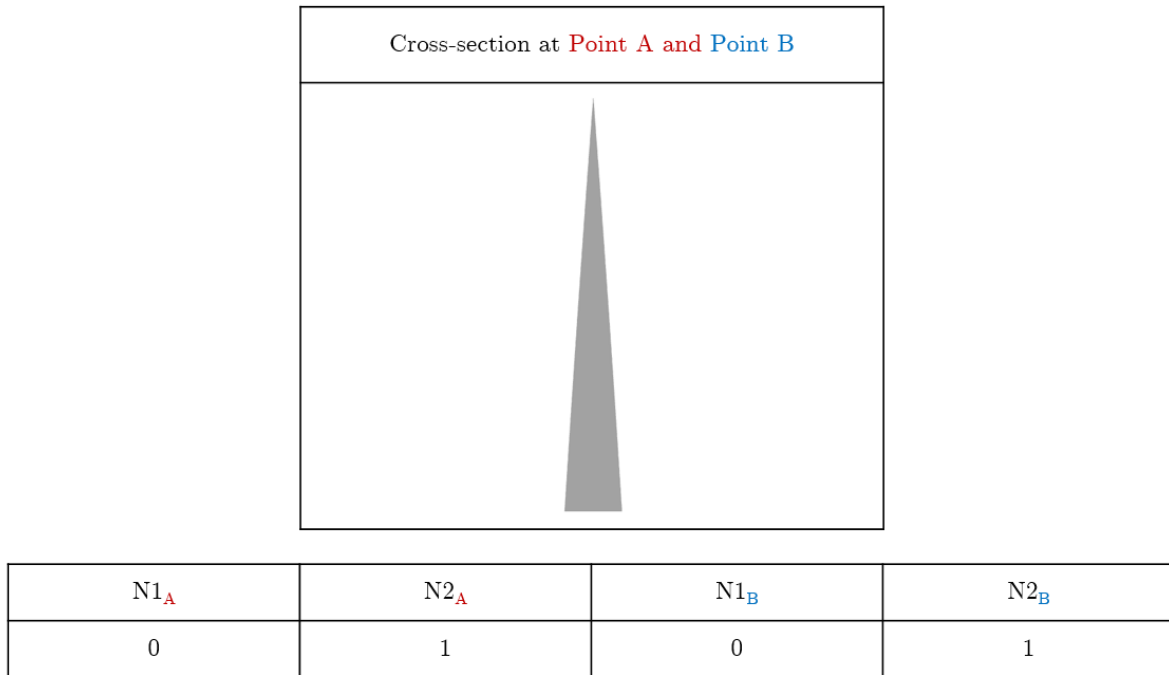


Table 5.5: Optimized design variables for cross-sections at control points A and B, UC=0.2

The sinusoidal corrugated shape completely dominates the longitudinal profile with an interpolation weight of 1, while the other two shapes have no contribution to the results. Since the trapezoidal shape does not impact the final geometry, the third variable, Angle θ , is irrelevant.

In this case, either point A or point B has the smallest cross-section Shape 2, which means Shape 2 is assigned along the entire longitudinal direction. The interpolation weight for Shape 1 is zero at all

the control points. Regarding the objective of minimum weight, it makes sense for the optimization algorithm always to choose the smallest cross-section when stress is allowed to occur in the structure. And the longitudinal shape is manipulated to satisfy the stress constraints.

The figure below provides a clearer illustration of the optimized geometry with the utility constraint set to 0.2. The top view clearly shows that the cross-sections don't vary along the longitudinal direction.

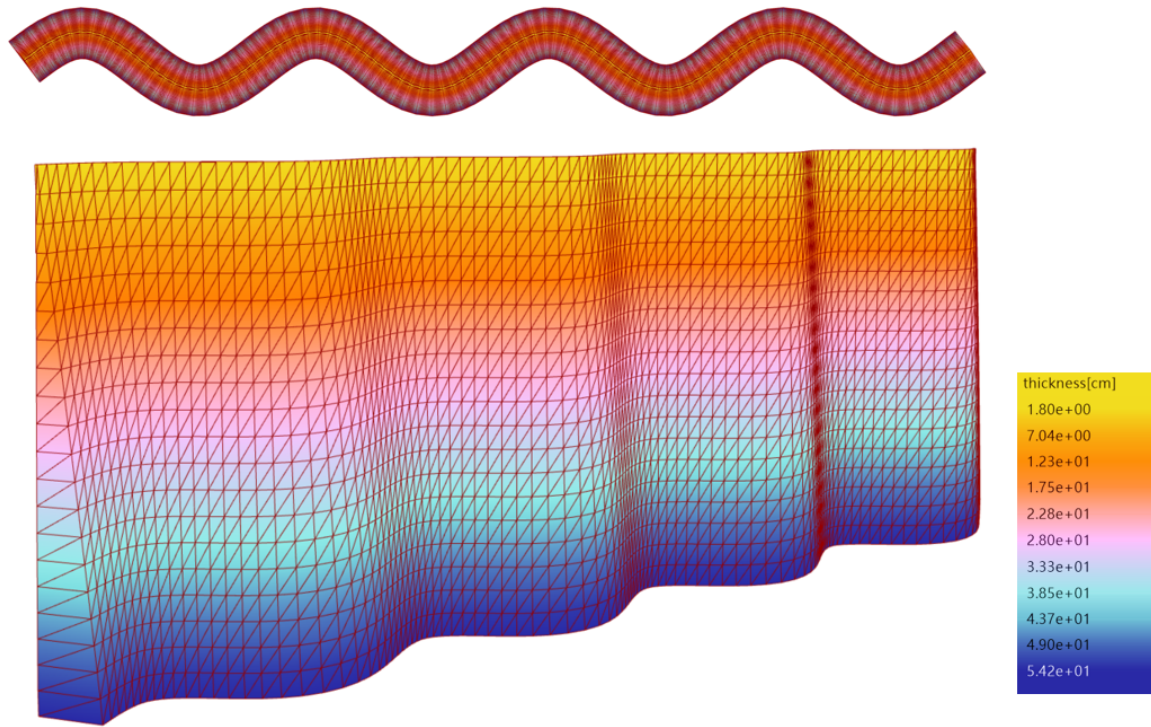


Figure 5.13: Illustration of optimized geometry with $UC=0.2$, top view and perspective view

Finally, the first principal stress at position 1, representing the upper boundary subjected to tension, is demonstrated below. Note that the right and left boundaries experience extremely high stress, and as a result, the right-most and left-most parts are not visualized, and the tensile stress in these areas is not taken into account. The model is designed to simulate an infinitely long wall; thus, ideally, each cycle should have the same stress results or at least be identical.

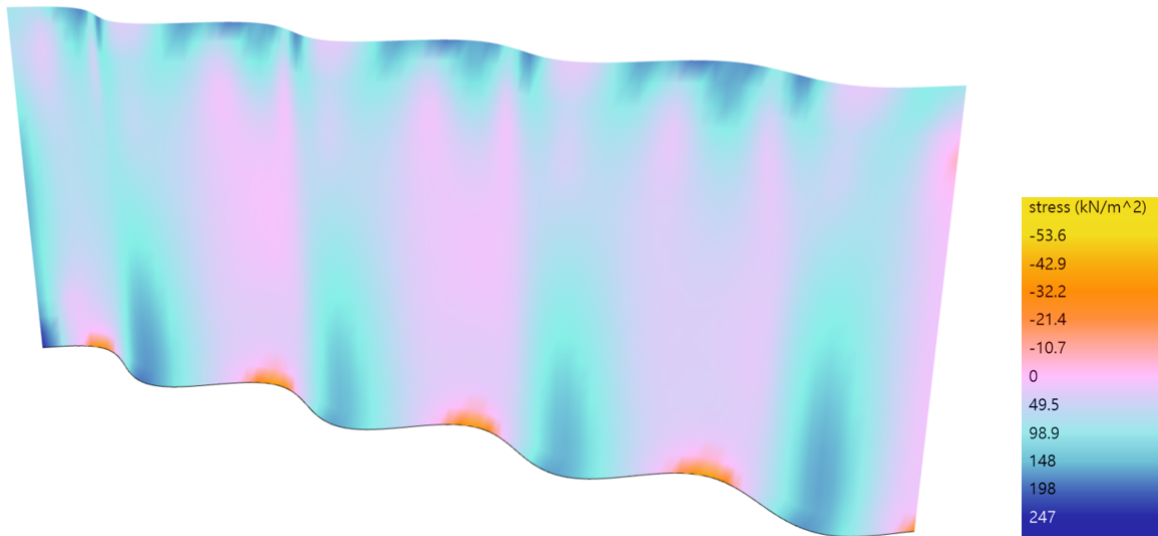


Figure 5.14: First principal stress in the upper boundary layer, UC=0.2

The maximum tensile stress that occurs in the structure is 247 kN/m^2 , which is close to the target of 260 maximum allowable tensile stress. The length of the longitudinal curve is 11.36 meters, and the total weight of the structure is 32592 kg. Therefore, the weight per meter is 2868.3 kg/m. However, since the length of this noise barrier is intended to cover 10 meters, it is more meaningful to divide the total weight by 10m, resulting in 3259.2 kg per meter.

5.4 Discussion

In Chapter 4, it was demonstrated that the optimization model and methodology are capable of producing precise results, which were also confirmed by analytical solutions in Chapter 3. Building upon this success, the optimal cross-section results and optimization framework are being utilized in the three-dimensional optimization.

The primary objective of this chapter is to assess the efficiency of different corrugated shapes and investigate how the longitudinal corrugated profile can influence the size of the cross-sections assigned to it. By combining the three selected corrugations with interpolation weights, we aim to identify which shape dominates and provides the best structural performance under specific stress constraints. Accordingly, it's anticipated that one interpolation weight will be close to one, while the weights for the other two shapes will be nearly zero. This approach also enables us to reduce the number of design variables, thus saving computational power.

Regarding the cross-sections, we utilize the left two results from Fig 4.2, which are the optimal symmetric shapes obtained from 2D optimization with desired utilities of 0 and 0.2. These two shapes are chosen

to represent the extreme cases, with Shape 1 having the largest area and Shape 2 having the smallest area. The design space lies between these two extremes, and the objective of the minimum weight result is to assign a cross-section closer to the smaller extreme at control points, with the assistance of an optimized longitudinal profile. Additionally, the linear interpolation of cross-sections between control points ensures a smooth transition of varying cross-sections along the longitudinal direction, making the geometry more feasible and manufacturable.

One concern of the 3D structural model is establishing the appropriate boundary conditions at the left and right ends to simulate an infinitely long wall. The logical approach would be to fix all three rotational DOFs (Rx, Ry, and Rz). However, the outcomes obtained by fixing each of these rotational DOFs are rather unexpected. Take "straight longitudinal profile + cross-section Shape 1" as an example. Inspecting the principal stress 1 in layer 1, which represents the maximum tensile stress on the upper boundary in tension, it's expected that the front view of the 10-meter-long wall exhibits zero stress in all the mesh. The results of fixing Rx, Ry, or Rz are illustrated in Fig 5.15.

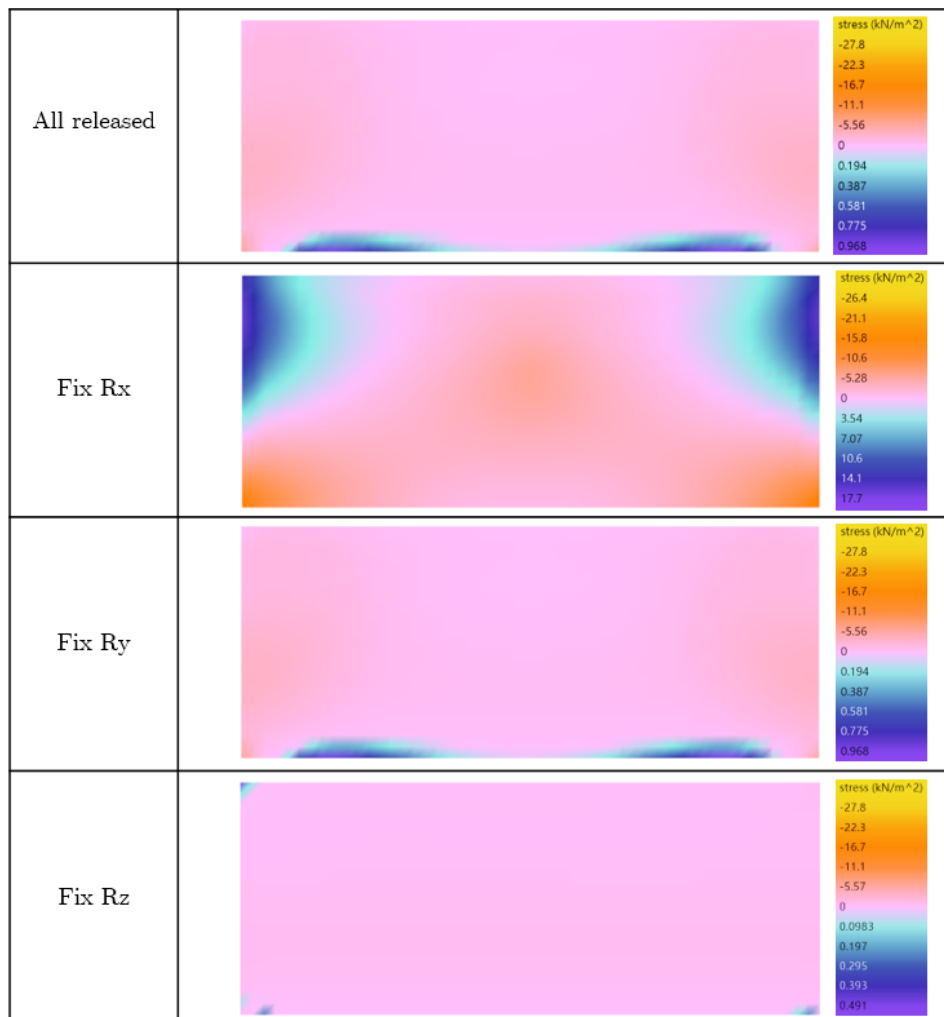


Figure 5.15: Front view of the straight wall with cross-section Shape 1: principal stress one in the upper boundary layer in tension

The findings reveal the following: Although fixing R_z yields the most accurate results, there is minimal difference compared to fixing R_y or releasing all the rotational DOFs. On the other hand, fixing R_x leads to higher stress concentrations at both ends, which is clearly undesirable. Based on these observations, R_z is fixed in both optimization scenarios with desired utilities of 0 and 0.2. However, in the case of target utility 0, where R_x has been fixed, exceedingly high tensile stress still occurs at the bottom corner. To address this issue, the maximum tensile stress in the 0.5-meter-long region from both the left and right ends was not displayed and consequently not taken into account in the optimization process. This is the reason why the stress results at both ends are not shown in Fig 5.12. Apart from this concern, the optimized results in both cases align well with the desired utility and demonstrate satisfactory performance.

Another significant distinction between 2D cross-section optimization and 3D structural optimization lies in their strategies for ensuring bending capacity. In the three-dimensional context, the entire structure collaborates to provide adequate bending resistance by adapting its shape. Consequently, it becomes necessary to release the rotational degree of freedom (DOF) at the bottom support condition, enabling the optimization algorithm to create a corrugated longitudinal profile that inherently possesses bending stiffness. As illustrated in Fig 5.16, the corrugated profile, when countering out-of-plane loading, distributes the bending moment over a greater distance compared to a straight longitudinal profile. This better distribution leads to reduced stress and material requirements. The optimized result of the corrugated longitudinal profile should exhibit adequate bending stiffness, hence even in practical applications where the bottom connection cannot be fully hinged, the impact on stress result is negligible.

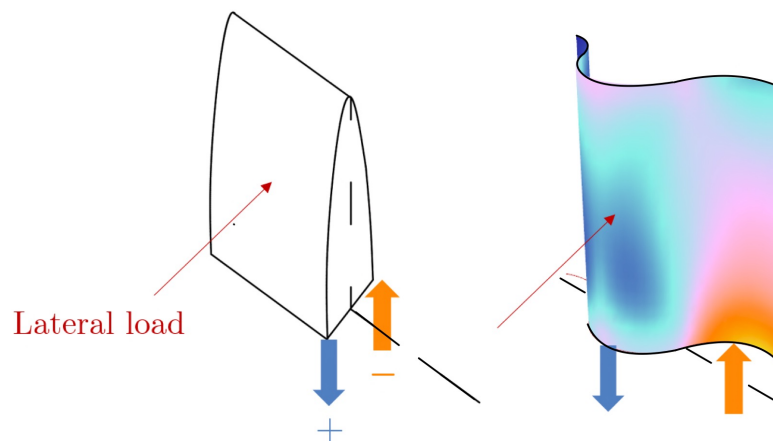


Figure 5.16: Comparison of bending moment between straight and corrugated longitudinal profiles

The optimization methodology is again proven to be really powerful by comparing the material savings with the non-optimized one, which is the "straight longitudinal profile + cross-section Shape 1", shown in the figure below:

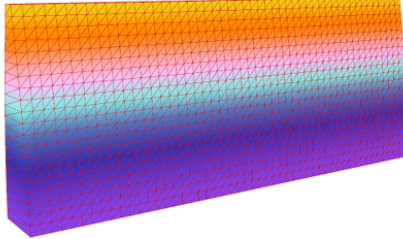
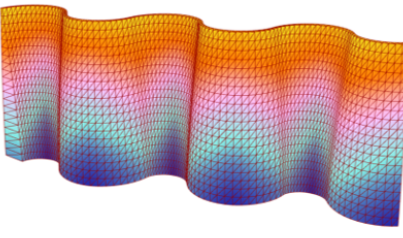
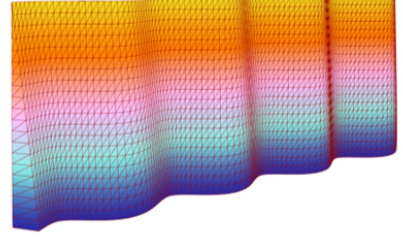
Before Optimization: Straight wall + Cross-section Shape 1		Maximum thickness: 115.90 	8.23 ton/m
UC=0		Maximum thickness: 82.99cm 	6.39 ton/m 22.6 % saving
UC=0.2		Maximum thickness: 54.24cm 	3.23 ton/m 60.5 % saving

Figure 5.17: Material savings of the optimal results with desired utility 0 and 0.2

The optimized design variables in two cases are shown in Fig 5.2, Fig 5.3 (for UC=0), and Fig 5.4, Fig 5.5 (for UC=0.2). Based on these results, we can make a conclusion that the corrugated shape "semi-circle" has the strongest bending stiffness, however, it's not as efficient as a sinusoidal wave when allowing a bit of stress to occur in the structure. As with the same length and height of one cycle, the curve length of the semi-circle is always longer than the sine wave. Additionally, when the desired utility is larger than zero ($UC_i > 0$), the algorithm will always assign interpolation weight 1 to the smallest cross-section and adjust the longitudinal shape to satisfy the stress constraint. On the other hand, when the target is zero tensile stress in the structure ($UC=0$), the assigned cross-section is somewhere in between the two extremes.

The optimized design variables in both cases are illustrated in Fig 5.2, 5.3 for UC=0, and 5.4, 5.5 for UC=0.2. From these results, we can deduce that the corrugated shape "semi-circle" exhibits the highest bending stiffness. However, it is not as efficient as the sinusoidal wave when allowing a slight degree of stress in the structure. This is because, for the same length and height of one cycle, the curve length of the semi-circle is always longer than that of the sine wave, which results in a larger weight.

Moreover, when the desired utility is non-zero ($UC > 0$), the optimization algorithm always assigns an interpolation weight of 1 to the smallest cross-section and adjusts the longitudinal shape to satisfy the stress constraints. Conversely, when the target is zero tensile stress in the structure ($UC = 0$),

the assigned cross-section falls somewhere between the two extremes, allowing for a balance between structural strength and material savings.

In conclusion, 3D structural optimization demonstrates the efficiency and effectiveness of various corrugated shapes. The optimized results prove that the selection of appropriate corrugation and interpolation weights can lead to significant material savings while maintaining structural capacity under specific stress constraints.

Chapter 6

Conclusion

Sec 3.4, 4.4, and 5.4 have provided advanced discussion for analytical uniform strength geometry, and numerical optimization in two dimensions, and in three dimensions. In this chapter, the general conclusions are made to answer the research questions.

The main research question of this research is: What is the optimal geometry, encompassing cross-section and longitudinal profile, of a noise barrier (namely a free-standing wall) made of a low tensile strength material, when considering self-weight and exposure to uniformly distributed lateral load?

Before summarizing our findings and drawing conclusions, there are three important sub-questions we need to address, which are crucial for understanding the outcomes and implications of this research.

1. Can analytical form-finding based on uniform strength theory be effectively utilized to determine optimal structural geometries under specific load conditions?

- The analytical derivations based on uniform strength theory yield constant (maximum) stress geometries, representing the most efficient structure under specific load cases. When the specified constant stress matches the material's maximum allowable stress, the structure's utilization is maximized as all cross-sections experience equal stress levels.
- The reliability of the analytical solutions for the constant stress 2D cross-sections was verified through numerical integration (FEA). The stress results confirm the precision of the mathematical representation of the geometries, as the presence of the specified constant stress in the structure aligns with the criteria outlined in the equations.
- The mathematical expression of the optimal structural geometry offers convenience, with design conditions such as loads and material properties as variables in the equation. Altering these inputs provides immediate access to optimal geometries.

2. Can numerical structural optimization, starting from a basic shape without any foundational understanding, efficiently transform it into the optimal geometry that closely resembles analytical solutions, employing a distinct strategy focused on minimizing weight under specified stress constraints?

- The numerical structural optimization process achieves minimum weight outcomes from a rectangular design space. Through the incorporation of topology optimization and shape optimization techniques, the framework has successfully generated optimal cross-sections that exhibit a close resemblance to the analytical solutions. This outcome underscores the framework's ability to yield optimal results even in situations where the most intuitive shape isn't readily apparent.
- The remarkable similarity between the outcomes of mathematical solutions and numerically optimized geometries provides strong evidence that both analytical form-finding, grounded in uniform strength theory, and numerical structural optimization focused on weight reduction, are capable of attaining optimal geometries. This mutual reinforcement underscores the validity and effectiveness of both approaches.
- The numerical framework's advantage lies in its flexibility to manipulate different desired utilities and design variables, yielding various results based on the user-defined input.

3. When extending to three dimensions, is it feasible to adjust the longitudinal profile of the noise barrier to enhance its bending stiffness against out-of-plane load?

- The release of the rotational degrees of freedom at the bottom support enables the optimization algorithm to generate a geometry that provides sufficient bending stiffness on its own. The optimized result of the corrugated longitudinal profile demonstrated superior resistance to out-of-plane loads compared to a flat wall, as the bending moment is more evenly distributed, resulting in reduced stress and subsequent material usage.
- The application of 3D numerical structural optimization with corrugated shapes as design variables showcases its efficiency and effectiveness in achieving material savings while ensuring bending capacity. This efficiency is evidenced through tremendous material savings compared with a non-optimized reference model.

We can now draw conclusions in relation to the stated objectives. The primary goal of this research is to ascertain the optimal geometries for a noise barrier constructed from a low-tensile strength material, while considering a load combination consisting of self-weight and uniformly distributed lateral load

- The load combination of self-weight and uniformly distributed lateral load gives rise to two distinct symmetric geometries based on the predefined constant maximum tensile stress at the tension boundary. An analytical solution, $h(y) = \frac{3\sqrt{2\gamma qy}}{2\gamma}$, exists when the value is zero; in contrast, when the specified stress is a non-zero value, a numerical approximation reveals a linear geometry. These

outcomes underscore that specifying constant tensile stress instead of mandating zero tensile stress considerably reduces material demands.

- The square root geometry, $h(y) = \frac{3\sqrt{2\gamma qy}}{2\gamma}$, ensures a persistent zero tensile stress along the tension boundary's height. This analytical solution has the advantage of obviating the need for extra structural components like reinforcement or foundation, especially when employing materials with limited tensile strength for building the noise barrier. Additionally, its symmetrical nature is practical in real-world scenarios, ensuring that the tension boundary maintains the specified constant stress even when lateral loads originate from the opposite direction.
- Balancing the bending moment coming from the lateral load can be achieved by utilizing the eccentricity of self-weight, resulting in an asymmetric shape, $h(y) = \frac{2\sqrt{\gamma qy}}{\gamma}$, with zero bending moments in the structure. Nonetheless, this asymmetric form is not feasible in practical applications, as it exacerbates stress conditions when loads are applied from the opposite direction.
- The 3D optimization outcomes indicate that the corrugated "semi-circle" profile showcases superior bending stiffness. However, it is outperformed by a sinusoidal wave profile when considering minimum weight structure. Specifically, when the objective is to maintain zero tensile stress ($UC = 0$), the semi-circle profile achieves a 22.6% reduction in total weight by decreasing the required cross-sectional area. Conversely, for non-zero desired utility, the sinusoidal wave profile attains an impressive 60.5% decrease in total weight, leading to substantial material efficiency gains.

The secondary objective of the research is to develop a practical numerical optimization framework capable of generating an optimal design that aligns with the results obtained through analytical form-finding utilizing uniform strength theory.

The numerical optimization process for two-dimensional cross-sections begins with topology optimization, generating the optimal material distribution within a rectangular design space. The resulting topology-optimized shape is then represented using a second-order polynomial, with its three coefficients serving as design variables to parametrically describe the geometry. Subsequently, Finite Element Analysis (FEA) is performed using Karamba3D, employing "beam elements" fixed at the bottom and subjected to load combination along the center line. The final step involves optimization using Opossum, aiming to minimize weight while adhering to the specified stress constraint, integrated into a single objective function through a penalty function approach. The stress constraint, utilizing the concept of the utility ratio (maximum tensile stress in the structure / tensile strength), corresponds to the specification of constant stress in analytical derivation.

Regarding the three-dimensional geometry model, three corrugated longitudinal profiles are selected as design space. These profiles are then combined using a shape function to create the final profile, with

the corrugation displaying a higher interpolation weight contributing more significantly to the overall geometry. For the cross-section assignment of the 3D structure, the optimal geometries obtained from the 2D optimization act as foundational shapes. These shapes are combined utilizing an interpolation function. The weighted outcomes of the cross-sections are allocated to five control points situated along the length of the barrier. Cross-sections between these control points are further linearly interpolated to ensure a seamless transition of variable cross-sections along the entire barrier. In terms of the structural model, the utilized element is a 3-node shear-deformable flat shell element. The absence of fixed rotational degrees of freedom at the bottom allows the optimization algorithm to create a geometry that inherently offers bending stiffness. The barrier's left and right ends are simulated as infinitely long walls (fix x and R_z). Ultimately, the optimization procedure is the same the method employed in the 2D approach.

Below are some general remarks for the numerical optimization framework:

- Topology optimization employing Karamba3D's "BESO for Shells" component effectively includes self-weight during iterations. The sensitivity to certain inputs necessitates careful manipulation to achieve desired outcomes. Restricting the non-design space by fixing the structure's height prevents impractical results.
- Shape optimization addresses issues like non-monolithic structures, zig-zag boundaries, and lack of symmetry in topology optimization results.
- The penalty function utilized in shape optimization successfully incorporates constraints into a single objective function. A proper setup for determining the penalty function is crucial to achieving desired outcomes.
- Slight discrepancies between numerical and analytical solutions may arise due to the limitations of the second-degree polynomial. Nevertheless, Opossum proves to be a robust optimization tool as its capability to reproduce comparable results to all analytical solutions.

Chapter 7

Recommendation

In this chapter, several recommendations for further research are presented:

1. In the current research, the three coefficients of second-order polynomial serve as the design variables to describe the boundary of cross-sections, however, there is a limitation of it to generate an accurate shape. It would be interesting to explore the use of higher-order polynomials or different methods, such as Non-uniform rational basis spline (NURBS) or Bezier and B-spline blending functions, to describe the geometry more accurately and efficiently.
2. Incorporating topology optimization into the three-dimensional structural optimization framework could be an intriguing aspect. Investigate whether assigning the topology-optimized cross-sections along the longitudinal direction and then conducting shape optimization to adjust the longitudinal profile and outer boundary of the cross-section would yield better results, compared to first optimizing the 3D geometry and then conducting topology optimization to remove inefficient parts. The potential benefit of topology optimization is to fill the non-structural inner part of the geometry with sustainable materials, achieving the highest material savings.
3. While the optimal geometries proposed in this research consider desired utility zero, implying no tensile stress exists in the model and thus linear analysis suffices, allowing for tensile stress in the structure could lead to significant material savings. To ensure structural safety, incorporating a real material model that accounts for nonlinear material behavior would better simulate real-world complexities, leading to more accurate results.

4. The current optimization objective focuses on minimizing the weight of the structure while incorporating stress constraints through the penalty function. However, the deflection of the structure is not considered. To account for achieving maximum stiffness, adding a maximum deflection constraint to the penalty function or conducting multi-objective optimization, including weight minimization and stiffness maximization, could provide a more comprehensive understanding of trade-offs and compromises in structural design.

5. Addressing the challenge of manufacturability for the optimized model is crucial. Given the limitations of additive manufacturing, it might be necessary to fine-tune the optimized model and generate a 3D smoothed model that retains almost the same structural performance but is easier to fabricate.

By pursuing these research recommendations, it leads to more sophisticated and practical design solutions in various engineering applications.

Bibliography

- [1] R. O. DeCastongrene and R. F. Dominguez, “An investigation into the properties and characteristics of homogeneous tapered cables,” 1975.
- [2] P. Aravind, “The physics of the space elevator,” *American Journal of Physics*, vol. 75, no. 2, pp. 125–130, 2007.
- [3] W. J. Lewis, “Constant stress arches and their design space,” *Proceedings of the Royal Society A*, vol. 478, no. 2257, p. 20210428, 2022.
- [4] S. Timoshenko, “Strength of materials, part i, elementary theory and problems (1955).”
- [5] J. Li and W. Gross, “Beams of uniform strength subjected to uniformly distributed load,” in *Proceedings of the Iowa Academy of Science*, vol. 62, no. 1, 1955, pp. 380–383.
- [6] M. P. Bendsøe, O. Sigmund, M. P. Bendsøe, and O. Sigmund, “Topology optimization by distribution of isotropic material,” *Topology Optimization: Theory, Methods, and Applications*, pp. 1–69, 2004.
- [7] V. Braibant, C. Fleury, and P. Beekers, “Shape optimal design-an approach matching cad and optimization concepts,” in *proceedings of the IFIP WG 5.2 Working Conference on Optimization in Computer-Aided Design*,,. Elsevier North Holland, Amsterdam, Netherlands, 1985.
- [8] X. Huang and M. Xie, *Evolutionary topology optimization of continuum structures: methods and applications*. John Wiley & Sons, 2010.
- [9] X. Huang and Y. Xie, “Evolutionary topology optimization of continuum structures including design-dependent self-weight loads,” *Finite Elements in Analysis and Design*, vol. 47, no. 8, pp. 942–948, 2011.
- [10] W. Lewis, “Mathematical model of a moment-less arch,” *Proceedings of the Royal Society A: Mathematical, Physical and Engineering Sciences*, vol. 472, no. 2190, p. 20160019, 2016.
- [11] L. Landweber and M. H. Protter, “The shape and tension of a light flexible cable in a uniform current,” 1947.

-
- [12] C. Tuckey, "Statics: a text-book for the use of the higher divisions in schools and for first-year students at the universities. by as ramsey. pp. xi, 296. 10s. 6d. 1934.(cambridge)," *The Mathematical Gazette*, vol. 18, no. 228, pp. 141–142, 1934.
- [13] J. Heyman, "Hooke's cubico-parabolical conoid," *Notes and Records of the Royal Society of London*, vol. 52, no. 1, pp. 39–50, 1998.
- [14] G. C. Marano, F. Trentadue, and F. Petrone, "Optimal arch shape solution under static vertical loads," *Acta Mechanica*, vol. 225, no. 3, pp. 679–686, 2014.
- [15] R. D. Hill, G. I. Rozvany, W. C. Ming, and L. K. Hwa, "Optimization, spanning capacity, and cost sensitivity of fully stressed arches," *Journal of Structural Mechanics*, vol. 7, no. 4, pp. 375–410, 1979.
- [16] I. Opatowski, "Cantilever beams of uniform strength," *Quarterly of Applied Mathematics*, vol. 3, no. 1, pp. 76–81, 1945.
- [17] R. J. Balling, R. R. Briggs, and K. Gillman, "Multiple optimum size/shape/topology designs for skeletal structures using a genetic algorithm," *Journal of structural engineering*, vol. 132, no. 7, pp. 1158–1165, 2006.
- [18] M. Kociecki and H. Adeli, "Two-phase genetic algorithm for size optimization of free-form steel space-frame roof structures," *Journal of Constructional Steel Research*, vol. 90, pp. 283–296, 2013.
- [19] N. Pollini, "Gradient-based prestress and size optimization for the design of cable domes," *International Journal of Solids and Structures*, vol. 222, p. 111028, 2021.
- [20] A. Mortazavi and V. Toğan, "Simultaneous size, shape, and topology optimization of truss structures using integrated particle swarm optimizer," *Structural and Multidisciplinary Optimization*, vol. 54, pp. 715–736, 2016.
- [21] B. D. Upadhyay, S. S. Sonigra, and S. D. Daxini, "Numerical analysis perspective in structural shape optimization: A review post 2000," *Advances in Engineering Software*, vol. 155, p. 102992, 2021.
- [22] P. W. Christensen and A. Klarbring, *An introduction to structural optimization*. Springer Science & Business Media, 2008, vol. 153.
- [23] Y.-L. Hsu, "A review of structural shape optimization," *Computers in Industry*, vol. 25, no. 1, pp. 3–13, 1994.
- [24] O. C. ZIENKIEWICZ, "Shape optimization and sequential linear programming," *Optimum Structural Design-Theory and Applications-*, 1973.

-
- [25] R. T. Haftka and R. V. Grandhi, "Structural shape optimization—a survey," *Computer methods in applied mechanics and engineering*, vol. 57, no. 1, pp. 91–106, 1986.
- [26] S. BHAIVIKATTI and C. RAMAKRISHNAN, "Optimum design of fillets in flat and round tension bars asme paper," N 77-DET-45, Tech. Rep., 1977.
- [27] P. Pedersen and C. L. Laursen, "Design for minimum stress concentration by finite elements and linear programming," *Journal of structural mechanics*, vol. 10, no. 4, pp. 375–391, 1982.
- [28] M. Luchi, A. Poggialini, and F. Persiani, "An interactive optimization procedure applied to the design of gas turbine discs," *Computers & Structures*, vol. 11, no. 6, pp. 629–637, 1980.
- [29] V. Braibant, C. Fleury, and P. Beckers, "Shape optimal design-an approach matching cad and optimization concepts," in *proceedings of the IFIP WG 5.2 Working Conference on Optimization in Computer-Aided Design,,.* Elsevier North Holland, Amsterdam, Netherlands, 1985.
- [30] M. H. Imam, "Three-dimensional shape optimization," *International Journal for Numerical Methods in Engineering*, vol. 18, no. 5, pp. 661–673, 1982.
- [31] M. Bendsøe and N. Kikuchi, "Generating optimal topologies in structural design using a homogenization method, comp," *Meths. Appl. Mechs. Engng*, vol. 71, pp. 197–224, 1988.
- [32] M. P. Bendsøe, "Optimal shape design as a material distribution problem," *Structural optimization*, vol. 1, pp. 193–202, 1989.
- [33] Y. Xie and G. P. Steven, "Shape and layout optimization via an evolutionary procedure," in *Proceedings of the international conference on computational engineering science*, 1992.
- [34] D. N. Chu, Y. Xie, A. Hira, and G. Steven, "Evolutionary structural optimization for problems with stiffness constraints," *Finite elements in analysis and design*, vol. 21, no. 4, pp. 239–251, 1996.
- [35] X. Yang, Y. Xie, G. Steven, and O. Querin, "Bidirectional evolutionary method for stiffness optimization," *AIAA journal*, vol. 37, no. 11, pp. 1483–1488, 1999.
- [36] M. Zhou and G. Rozvany, "The coc algorithm, part ii: Topological, geometrical and generalized shape optimization," *Computer methods in applied mechanics and engineering*, vol. 89, no. 1-3, pp. 309–336, 1991.
- [37] M. P. Bendsoe and O. Sigmund, *Topology optimization: theory, methods, and applications*. Springer Science & Business Media, 2003.
- [38] X. Huang and Y. Xie, "Convergent and mesh-independent solutions for the bi-directional evolutionary structural optimization method," *Finite elements in analysis and design*, vol. 43, no. 14, pp. 1039–1049, 2007.

-
- [39] M. Zhou and G. Rozvany, “The coc algorithm, part ii: Topological, geometrical and generalized shape optimization,” *Computer methods in applied mechanics and engineering*, vol. 89, no. 1-3, pp. 309–336, 1991.
- [40] K. Svanberg, “The method of moving asymptotes—a new method for structural optimization,” *International journal for numerical methods in engineering*, vol. 24, no. 2, pp. 359–373, 1987.
- [41] O. Sigmund, “A 99 line topology optimization code written in matlab,” *Structural and multidisciplinary optimization*, vol. 21, pp. 120–127, 2001.
- [42] G. Rozvany and M. Zhou, “Optimality criteria methods for large discretized systems,” *Advances in design optimization*, pp. 41–108, 1994.
- [43] M. Bruyneel and P. Duysinx, “Note on topology optimization of continuum structures including self-weight,” *Structural and Multidisciplinary Optimization*, vol. 29, no. 4, 2005.
- [44] M. Stolpe and K. Svanberg, “An alternative interpolation scheme for minimum compliance topology optimization,” *Structural and Multidisciplinary Optimization*, vol. 22, no. 2, pp. 116–124, 2001.
- [45] M. Bruyneel and P. Duysinx, “Note on topology optimization of continuum structures including self-weight,” *Structural and Multidisciplinary Optimization*, vol. 29, no. 4, 2005.
- [46] T. Wortmann and G. Nannicini, “Black-box optimisation methods for architectural design,” in *21st International Conference on Computer-Aided Architectural Design Research in Asia (CAADRIA 2016)*, Melbourne, 2016, pp. 177–186.
- [47] P. Janssen, P. Loh, A. Raonic, and M. Schnabel, “Introducing and evaluating a model-based optimization tool for grasshopper.”
- [48] A. A. A. A. Khan, “Shape optimization of compressed members under buckling,” 2021.
- [49] C. Preisinger, “Linking structure and parametric geometry,” *Architectural Design*, vol. 83, no. 2, pp. 110–113, 2013.
- [50] M. SELMI and Z. Y. İLERİSOY, “A comparative study of different grasshopper plugins for topology optimization in architectural design,” *Gazi University Journal of Science Part B: Art Humanities Design and Planning*, vol. 10, no. 3, pp. 323–334.
- [51] S. Adriaenssens, P. Block, D. Veenendaal, and C. Williams, *Shell structures for architecture: form finding and optimization*. Routledge, 2014.
- [52] Y.-L. Hsu, M.-S. Hsu, and C.-T. Chen, “Interpreting results from topology optimization using density contours,” *Computers & Structures*, vol. 79, no. 10, pp. 1049–1058, 2001.

- [53] Ö. Yeniay, “Penalty function methods for constrained optimization with genetic algorithms,” *Mathematical and computational Applications*, vol. 10, no. 1, pp. 45–56, 2005.
- [54] T. Wortmann, “Genetic evolution vs. function approximation: Benchmarking algorithms for architectural design optimization,” *Journal of Computational Design and Engineering*, vol. 6, no. 3, pp. 414–428, 2019.
- [55] A. Airoidi, G. Sala, L. A. Di Landro, P. Bettini, and A. Gilardelli, “Composite corrugated laminates for morphing applications,” in *Morphing Wing Technologies*. Elsevier, 2018, pp. 247–276.
- [56] E. Izadpanah, S. Shojaee, and S. Hamzehei-Javaran, “Time-discontinuous finite element analysis of two-dimensional elastodynamic problems using complex fourier shape functions,” *Journal of Applied and Computational Mechanics*, vol. 4, no. Special Issue: Applied and Computational Issues in Structural Engineering, pp. 442–456, 2018.
- [57] J. Argyris, L. Tenek, and L. Olofsson, “Tric: a simple but sophisticated 3-node triangular element based on 6 rigid-body and 12 straining modes for fast computational simulations of arbitrary isotropic and laminated composite shells,” *Computer Methods in Applied Mechanics and Engineering*, vol. 145, no. 1-2, pp. 11–85, 1997.